Insights on Seasonal Fluxes in a Desert Shrubland Watershed from a Distributed Sensor Network

by

Ryan Templeton

A Thesis Presented in Partial Fulfillment
of the Requirements for the Degree
Master of Science

Approved November 2011 by the
Graduate Supervisory Committee:

Enrique Vivoni, Chair
Peter Fox
Larry Mays

ARIZONA STATE UNIVERSITY

December 2011

ABSTRACT

The North American Monsoon System (NAMS) contributes ~55% of the annual rainfall in the Chihuahuan Desert during the summer months. Relatively frequent, intense storms during the NAMS increase soil moisture, reduce surface temperature and lead to runoff in ephemeral channels. Quantifying these processes, however, is difficult due to the sparse nature of coordinated observations.

In this study, I present results from a field network of rain gauges (n = 5), soil probes (n = 48), channel flumes (n = 4), and meteorological equipment in a small desert shrubland watershed (~0.05 km^2) in the Jornada Experimental. Using this high-resolution network, I characterize the temporal and spatial variability of rainfall, soil conditions and channel runoff within the watershed from June 2010 to September 2011, covering two NAMS periods. In addition, CO_2, water and energy measurements at an eddy covariance tower quantify seasonal, monthly and event-scale changes in land-atmosphere states and fluxes.

Results from this study indicate a strong seasonality in water and energy fluxes, with a reduction in Bowen ratio (B, the ratio of sensible to latent heat fluxes) from winter (B = 14) to summer (B = 3.3). This reduction is tied to shallow soil moisture availability during the summer (s = 0.040 m^3/m^3) as compared to the winter (s = 0.004 m^3/m^3). During the NAMS, I analyzed four consecutive rainfall-runoff events to quantify the soil moisture and channel flow responses and how water availability impacted the land-atmosphere fluxes. Spatial hydrologic variations during events occur over distances as short as ~15 m.

The field network also allowed comparisons of several approaches to estimate evapotranspiration (ET). I found a more accurate ET estimate (a reduction of mean absolute error by 38%) when using distributed soil moisture data, as compared to a standard water balance approach based on the tower site. In addition, use of spatially-varied soil moisture data yielded a more reasonable relationship between ET and soil moisture, an important parameterization in many hydrologic models. The analyses illustrates the value of high-resolution sampling for quantifying seasonal fluxes in desert shrublands and their improvements in closing the water balance in small watersheds.

This thesis is dedicated to my wife Tiffani for her patience and understanding.

ACKNOWLEDGEMENTS

I would like to thank Enrique Vivoni for the opportunity to pursue the research outlined in this document, Luis Mendez-Barroso for his help in installing and troubleshooting the environmental equipment, the researchers and staff at the Jornada Experimental Range and New Mexico State University for their cooperation with and contributions to this project, Aline Jaimes and Gesuri Ramirez for their collaboration in troubleshooting the flux tower, and finally all members of the Vivoni research group for their support. Special appreciation goes to the Army Research Office (ARO) for funding this project.

TABLE OF CONTENTS

LIST OF TABLES

Table Page

Table Page

LIST OF FIGURES

1. INTRODUCTION

The North American Monsoon (NAM) results in a pronounced seasonal increase in precipitation during the summer months of July, August, and September leading to dramatically elevated vegetation production and surface runoff generation in response to high storm intensity and increased soil moisture. These responses occur in-phase with summer solar radiation maxima and induce rapid vegetation greening following the driest months of the year. While historical research of the NAM has focused on the southwestern US, the core of the regional response transpires in northwestern Mexico where upwards of 70% of annual precipitation can occur during the summer months (Figure 1). Arid and semiarid landscapes dominate most of the region primarily affected by the NAM. It was the disparities in summer rainfall patterns between Arizona and southern California which incited interest in the seasonal shifts in rainfall within the region and an interest in the determination of storm cell origination (Beals, 1922). However, it wasn't until Reed (1933) recognized seasonality of precipitation was a regional feature. Reed was able to link this pattern of regional convection activity to upper-level atmospheric instability (Adams and Comrie, 1997). The system was later described as monsoonal with moisture originating from the Gulf of California and the Pacific ocean (Hales, 1972).

As a monsoonal system, the NAM is highly dependent on land, oceanic, and atmospheric interactions within the region. Prior to monsoon onset, a pressure gradient is established between the eastern Pacific and the Gulf of California. Interruption of this gradient by storm formation in the lower Gulf of California results in humid air overlying the gulf pushing northward and eastward into the Sonoran desert. The interaction of this low-level moist air with heated surface temperatures results in the perpetuation of

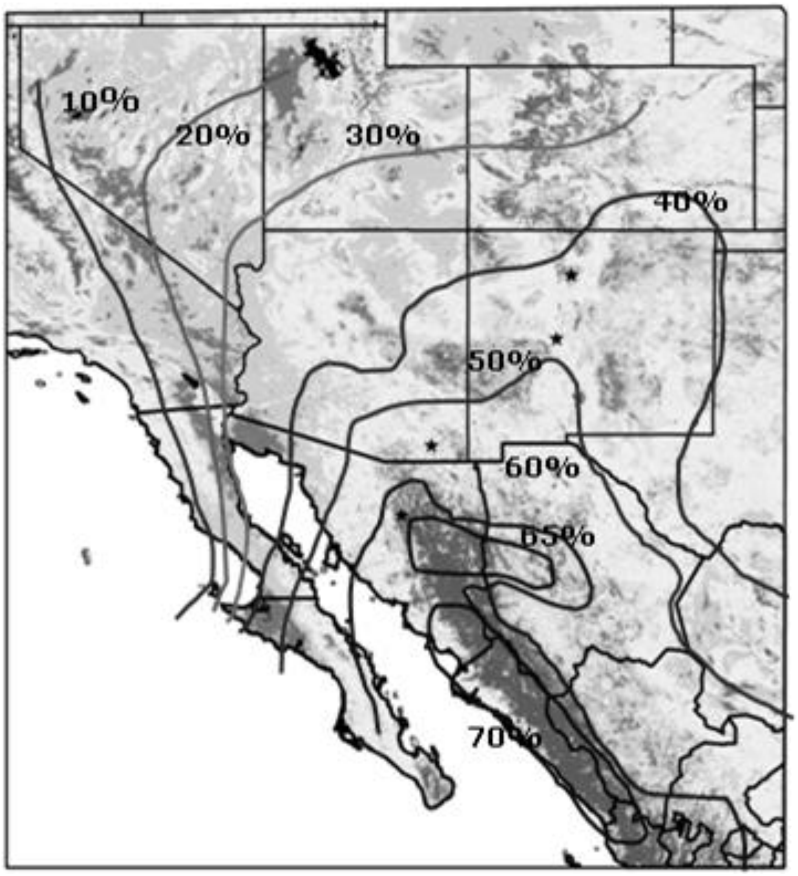

Figure 1: Regional map of NAM region with contours representing the percent of annual precipitation accounted for by the NAM.

convective cell formation resulting in the mixture of the Gulf of California moist air with higher altitude moist air which originates from the Gulf of Mexico (Adams and Comrie, 1997; Schmitz and Mullen, 1996). Gulf of California air can also be recirculated to higher atmospheric levels and transported to desert regions in the upper atmosphere through interaction with the Sierra Madre Occidental (Maddox et al., 1995; Schmidt and Mullen, 1996).

While the NAM system is highly predictable in its annual occurrence, the temporal and spatial onset and intra-seasonal precipitation variability is difficult to forecast (Higgins et al., 1997). Gutzler and Preston (1997) attributed the variability in monsoonal season rainfall to the convective nature of individual storms in the region but instead of attempting to focus on the origination and prediction of individual storm events, they focused on regional scale trends. They found an inverse relationship between Pacific Ocean sea surface temperature (SST) anomalies and summertime precipitation anomalies. More recently, Cerezo-Mota et al. (2011) reported that regional precipitation in the northern portion of the North American monsoon was highly dependent on Gulf of Mexico moisture and the Great Plains low-level jet. While regional scale prediction of NAM onset and magnitude from feedback parameters is important for understanding the system in its entirety, the NAM system exhibits high spatial variation of precipitation due to the convective nature of storm event formation. Gochis et al. (2007) showed in northwestern Mexico that precipitation could triple in < 20 km over the monsoon season. Isolated storm cells formed by the NAM system stress the importance of understanding localized meteorological and hydrological processes in order to fully characterize these systems. To this end, spatial variation of rainfall is important for understanding how a system will react in terms of soil moisture increases and subsequent runoff and vegetation production at a more localized scale and how these reactions may result in feedbacks affecting local meteorology and NAM system perpetuation.

Elevated summer soil moisture in the NAM region plays a critical role in the local responses of energy and water fluxes and runoff production. In semiarid systems located in the NAM region soil moisture varies spatially and temporally influencing hydrologic, energy, and biotic responses of the system to rainfall events (Huenneke and Schlesinger, 2004; Kurc and Small, 2007). As soil moisture increases runoff ratios can be expected to increase; however, these responses are not usually linear relationships (Gochis et al., 2006). The work by Gochis et al. (2006) indicates that drastically different runoff responses over short distances can occur due to small changes in the degree of soil moisture saturation within a region. Not only does horizontally variable soil moisture affect water distribution, but vertical depth profiles of soil moisture determine how water will be partitioned between transpiration and evaporation in these regions. Cavanaugh et al. (2011) found that the onset of the NAM season resulted in shallow soil moisture evaporation dominating evapotranspiration (ET) in the region. It wasn't until three weeks after the NAM season onset that transpiration began to contribute to ET, in response to increases in deeper soil moisture. Only approximately the top 20 cm of soil moisture contributes to an evaporative response (Yamanaka and Yonetani, 1999) while deeper soil moisture is primarily partitioned to vegetation transpiration pools since very little water results in deep aquifer recharge. Evapotranspiration partitioning is important for understanding energy dynamics and determining the rate at soil water reserves are reintroduced into the atmosphere. However, feedbacks between vegetation coverage and soil moisture can affect hydrological and meteorological responses of a system in processes other than evapotranspiration partitioning, and can increase or decrease spatial variability of these responses depending on the vegetation regime.

Following the dry spring months, vegetation in the NAM region quickly responds to the summer precipitation onset with rapid greening and high production (Vivoni et al., 2008, Dominguez et al., 2008). Regional analyses of precipitation patterns with elevation (Gochis et al., 2007; Gebremichael et al., 2007) indicate variable precipitation may control vegetation community structure. Forzieri et al. (2011) classified the NAM region in 6 separate ecoregions characterized by vegetation dynamics found throughout the NAM region. This study provided evidence for the importance of understanding rainfall distribution on vegetation community structure at the regional scale based on local terrain and geographic position; however, feedbacks between atmospheric processes and vegetation dynamics can lead to intensification and perpetuation of the NAM at the local scale as is evidenced by the recycling of precipitation within a local system (Dominguez et al., 2008; Mendez-Barroso and Vivoni, 2010). Retention of precipitation locally within NAM region vegetation communities presents a method for the continued high summer net productivity necessary by these vegetation communities to proliferate. While these systems are primed for the responses to summer rainfall experienced during the NAM, vegetation community shifts are constantly occurring at regional and local scales and the impact of these shifts on NAM system intensity and continuation is unknown.

Local hydrology exhibits hefty controls on the shifts of vegetation communities in semiarid regions. Shifts in the local hydrology can lead to changes in vegetation community structure. ‘Desertification’ is a phenomenon by which historically established grasslands in semiarid regions have been replaced by shrublands leading to a less homogenous land cover with implications for soil moisture and nutrient distribution. When examining the effects of climate change on further desertification, Peters et al. (2010) discovered that the grass, *Bouteloua eriopoda* (black grama), could increase recruitment by 52% in lowland areas of the Jornada basin as a response to a 50% increase in summer rainfall. Under the same conditions, modeling showed that other plant types would only increase recruitment by 24-27%. In contrast, a reduction in rainfall of only 25% would result in the complete decimation of *B. eriopoda* recruitment in these regions. Peters et al. concluded that a shift in the precipitation regime from current patterns to higher intensity, lower duration storms with comparable rainfall totals as today (as predicted by the IPCC, 2007) could result in the reversion of desertification effects in these lowland areas due to increased upland runoff contributions leading to higher water redistribution to these regions. This idea gained further credence when Thomey et al. (2011) found that less frequent but more intense storms would result in increased *B. eriopoda* in a Chihuahuan desert landscape. Reestablishment of grasses in semiarid regions such as the Jornada basin, due to increased runoff production, could result in an interesting feedback scenario within the system whereby increased grass recruitment over shrub recruitment could lead to the reduction of surface runoff due to relative decrease in bare soil plots. Surface runoff production is of major interest and is one of the reasons high resolution characterization of semiarid regions is important in understanding the response of these systems to changes in precipitation regimes.

Surface runoff and channel flows increase in semiarid regions during the NAM season due to heightened antecedent soil moisture and high intensity storms. Gochis et al. (2006) examined 15 basins in northwestern Mexico and found that 85% of annual streamflow occurred during the NAM season and runoff ratios increased during the summer months. This has important implications for the conservation and usage of water supplies by local human communities throughout the year. Since much of this region is used for arable land, water distribution and storage for dry seasons can be of high importance. Furthermore flood events are more likely to occur during the wet summer months which could have devastating effects on local communities. However, the key to understanding flood formation occurs at the local scale. Understanding how spatial distributions of plant communities and thus soil moisture and infiltration rates affect surface flow formation is highly important. While precipitation is the primary driver in runoff formation, more localized topographic and surface features and properties result in spatially varied responses. Plant community structure plays an important role in soil moisture and runoff formation heterogeneities in semiarid shrublands. Infiltration rates beneath shrub canopies has been shown to increase when compared to intercanopy regions (Pierson et al., 1994), which has been attributed to increased detritus, and thus organic matter. Furthermore, detritus beneath shrubs has also been shown to decrease overland water flow rates, decreasing runoff formation (Abrahams et al., 2003). It has also been suggested that the reduction in rainfall impact energy beneath shrub canopies decreases soil compaction, and thus crust formation (Duniway et al., 2010). Finally, reduction of soil evaporative effects under shrub canopies due to shading can affect soil moisture content in the upper soil column (Breshears et al., 1998). The spatial variability associated with shifts from grass dominated regions to shrub dominated regions in the NAM region have also been shown to result in increased rill formation in intershrub areas due to increased surface water flows (Wainwright et al., 2000). These results outline the spatially variable nature of runoff formation in semiarid watersheds due to vegetation interactions and its feedbacks on the system. Like rainfall, solar radiance (due to the watershed hillslope aspect), and soil textures; runoff formation is highly variable even at the small watershed scale. This variability of runoff formation, while extremely important in understanding watershed responses, is still poorly documented and requires high resolution characterization in order to fully understand local controls.

Increased spatiotemporal characterization of this region not only aids in understanding the systems response to energy flux and hydrologic processes and their feedbacks with the local environment, but it also provides the opportunity for higher resolution and more accurate distributed hydrological modeling and forecasting. Hydrological modeling within this region focuses heavily on the prediction of streamflow for water resource usage, runoff production for flood forecasting, or environmental shifts in vegetation structure. Most of these efforts use low resolution datasets in order to calibrate forecasting models while ignoring how spatial distributions of intra-watershed rainfall, soil moisture dynamics, local topography, and heterogeneous vegetation coverage can create feedback systems which alter model responses of interest. In order to compensate for inadequate datasets, many modeling efforts have used downscaling techniques to create adequately resolute input datasets (Beuchat et al., 2011; Najafi et al., 2011; Mehrotra and Sharma, 2011). While Beuchat et al. (2011) was able to dramatically increase the accuracy of rainfall downscaling from daily data to subdaily data, error in calculating correct rainfall rates at 12 hours still approached 20%, for 6 hours it approached 30%, and for 2 hour intervals it approached 50% in some instances. The problems associated with downscaling are numerous and have been well defined. Robust datasets and watershed characterizations provide the necessary tools for not only accurate model calibration, but also for identifying the resolution at which watershed sampling should occur for accurate modeling of a region.

Hydrologic and energy dynamics control climate and the vegetation coverage in a region. The southwestern US exhibits high degrees of seasonality in rainfall leading to strong seasonal shifts in energy and hydrologic fluxes in the region. While efforts have increased in the characterization of these flux changes at high temporal scales (Scott, 2010; Cavanaugh et al., 2011; Mendez-Barroso and Vivoni, 2010), little work has focused on how small spatial scale changes in these environments may affect hydrologic and energetic processes. Scott (2010) presented a point-scale method to estimate evapotranspiration (ET) for a watershed utilizing the water balance. This approach is an excellent method for the determination of the rate of water reintroduction to the atmosphere from the watershed surface if direct field measurements cannot be obtained. However, high spatial variability occurs within semiarid shrublands, which may necessitate higher spatial sampling for more accurate characterization. In the past 100-200 years, a shift in the dominant vegetation type in the southwestern US has occurred. What were primarily grass dominated regions have become shrublands due to a process referred to as desertification. The process of desertification has increased the heterogeneity in these systems, resulting in increases in bare soil regions. Increases in bare soil coverage have lead to decreasing infiltration rates, increasing runoff production, and increasing surface albedo in these areas. In contrast, the shrub covered areas have high infiltration rates, decreased runoff production, and decreased surface albedo. This increase in hydrologic and energetic process heterogeneity has lead to a need for increased spatial sampling within a watershed in order to accurately characterize the system as a whole.

In this study, we conduct a high resolution characterization of a watershed in the NAM region of the southwestern U.S. The basin is located in southern New Mexico in a Chihuahuan desert shrubland and was outfitted with a dense environmental sensor network. Based on this effort, this thesis has the following main objectives:

1. To understand watershed-scale temporal dynamics at the event, seasonal, and yearly scale through the installation of a distributed soil moisture network, a meteorological flux tower, a network of rain gauges, and ephemeral stream flumes all sampling at high temporal resolution.
2. To investigating the importance of spatial variability of hydrologic processes within a small watershed during the NAM season using the sensor network previously mentioned.
3. To determine the optimal spatiotemporal sampling resolution of environmental sampling necessary to adequately characterize the watershed and provide a relationship between surface and atmospheric processes.
4. To provide an accurate point-scale calibration and testing of the TIN-based Real-Time Integrated Basin Simulator (tRIBS) for the hydrological and meteorological forecasting of the system.

Few studies have been conducted in the NAM region analyzing watersheds at high resolution for both hydrological and meteorological characterization. This work provides unique knowledge and analysis on the spatial and temporal resolution at which surface and atmospheric evolve at a variety of temporal scales. Furthermore, this thesis will provide the necessary tools for adequately forecasting responses to storm pulse events and monsoon seasonal shifts for small semiarid watersheds.

2. METHODS

2.1 Watershed Characterization

The Jornada basin Long-term Ecological Research (LTER) project was established in 1982 as one of the largest desert rangeland study sites in the United States covering approximately 100,000 ha of semiarid shrub and grassland. Scientific investigation of desertification and shrub encroachment on grasslands began in 1912. The thorough investigation of local desertification (Okin et al., 2006; Fredrickson et al., 2006), plant processes (Yao et al., 2006; Bestelmeyer et al., 2006), and geological characterization (Monger and Bestelmeyer, 2006) provided a uniquely characterized backdrop for our research. The research outlined in this document occurred in a shrub dominated portion of the San Andres mountains piedmont, along the southeastern boundary of the basin (Figure 2). We analyzed a small watershed of ~0.047 km^2 area

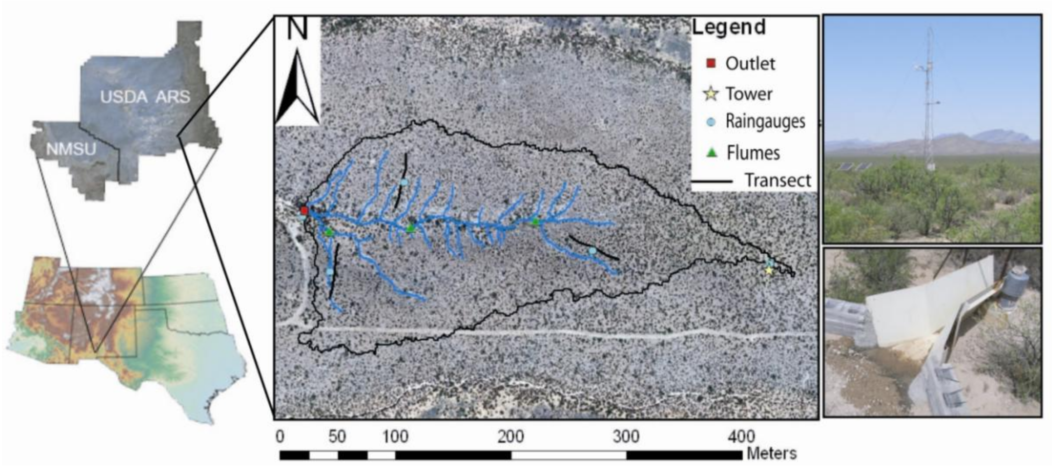

Figure 2: Location of the Tromble watershed within the Jornada Experimental Range. Stream network delineation was performed by manual GPS sampling. Equipment locations are given in the center panel with an underlying aerial image of the site as produced from BAT3 images.

(DTM) was created from an aerial orthomosaic collected in October 2010. This DTM was then utilized to delineate the watershed boundary upstream of the outlet flume (Figure 2). We further characterized intrawatershed parameters such as pixel slope and aspect, and delineated the watershed into subbasins using ArcGIS (ESRI). Soil sampling within the watershed boundary at multiple locations up to a depth of 50 cm indicated the dominant soil type is loam and a distinct calcium carbonate horizon exists between 0 cm (in parts of the main channel) and 60 cm depth (in the upper watershed elevations). The development of this caliche layer at an average depth of ~40cm throughout the watershed indicates minimal vertical soil water redistribution occurs below this depth and thus, this layer was treated as the lower boundary of the soil profile throughout our work.

Historical rainfall data was obtained from a rain gauge (TB3, Hydrological Services Pty Ltd) installed in 2005, located at the outlet flume. Annual rainfall from 2005 to present was approximately 308 mm (Figure 3). The highest monthly rainfall rates occur during the NAM season months of July, August, and September. During this three month period ~59.5% of the annual rainfall occurred. The short duration and high intensity NAM season storms in the southwestern U.S. strongly affect the surface hydrologic and topographic conditions of these desert landscapes, ultimately directing surface water redistribution and channel formation throughout the watershed. Using a Leica Geosystems GPS1200, the watershed’s ephemeral stream and rill network was manually mapped (Figure 2).

2.2 Environmental Sensor Network

Rainfall, runoff, and soil moisture and temperature were measured spatially

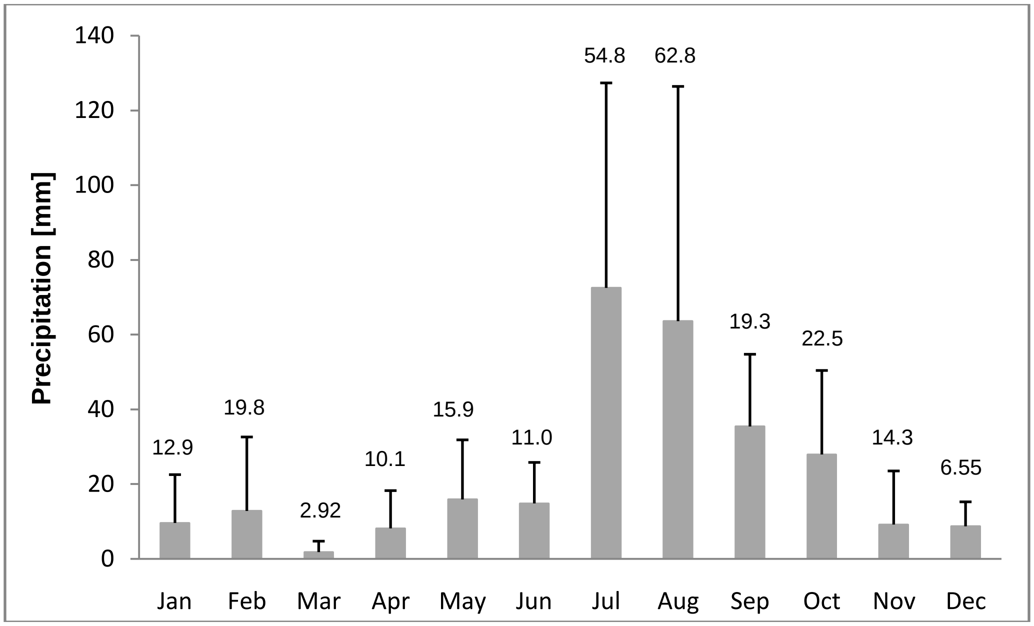

Figure 3: Annual and monthly average rainfall for the period of 2005-2010. Measurements were taken at the Tromble watershed outlet. Values of 1 standard deviation are shown.

through environmental sampling by a dense sensor network initially installed in late May 2010. All equipment referred to in this section is shown in an aerial map in supplemental material Figure A.1. Sensor IDs, locations, and elevations are described in Table 1. Installation of three soil moisture transects on the north-facing (transect 1 – T1), south-facing (transect 2 – T2), and west-facing slopes (transect 3 – T3) of the watershed allowed for semi-hourly sampling of soil moisture and temperature and instantaneous sampling of rainfall (Figure 2). Each transect consisted of 15 soil dielectric sensors (Stevens Water Monitoring, Hydra Probe) with 5 sensor locations on each transect spanning from near the main channel to approximately 160 feet upslope. The Hydra Probe measures soil conductance of an electric signal in order to determine the impedance the soil creates on the sampling probe and thus determine the water content of the soil and is based on the work of Campbell (1990). Soil sampling for volumetric soil

Table 1: Sensor locations within the Tromble watershed for all installed instrumentation. Relative locations of sensors (UTM - WGS 1984, 13N), as identified by Sensor ID, are presented in Appendix A.

Sensor Type	ID	Northing [m]	Easting [m]	Elevation [m]
Soil Probe	SM1	3606431.753	349156.521	1453.61
	SM2	3606418.716	349154.273	1454.85
	SM3	3606406.579	349153.374	1455.85
	SM4	3606396.690	349152.025	1456.82
	SM5	3606384.103	349148.879	1457.34
	SM6	3606461.421	349205.968	1456.04
	SM7	3606471.311	349208.665	1456.88
	SM8	3606482.998	349211.363	1457.64
	SM9	3606494.686	349214.959	1458.62
	SM10	3606507.273	349214.959	1459.04
	SM11	3606437.596	349356.559	1462.21
	SM12	3606432.202	349365.999	1462.89
	SM13	3606428.156	349377.686	1463.66
	SM14	3606421.414	349388.924	1464.36
	SM15	3606417.817	349400.163	1465.02
Rain gauge	R1	3606454.229	349126.402	1452.51
	R2	3606407.928	349150.227	1455.80
	R3	3606483.448	349214.509	1457.77
	R4	3606425.459	349377.237	1463.61
	R5	3606414.671	349530.974	1469.47
Flumes	F1	3606455.577	349126.852	1452.52
	F2	3606441.642	349149.328	1453.00
	F3	3606444.339	349219.004	1455.00
	F4	3606451.082	349328.239	1459.61
Tower	To	3606407.793	349528.844	1469.40

water and soil temperature occurred at three depths (5 cm, 15 cm, and 30 cm). The only transect to deviate from this design was the south-facing transect which had caliche at a depth of 25 cm at the sensor location closest to the watershed main channel (SM6) and thus no sensor was installed at a depth of 30 cm for this location.

Tipping bucket rain gauges (Texas Electronics, TE525MM) measured rainfall at each of the soil moisture transects and at the eddy covariance tower; rainfall was also measured at the watershed outlet (Hydrological Services, TB3 tipping bucket rain gauge). This allowed for spatially varied sampling of precipitation (n=5) spanning the watershed domain. Each gauge was mounted at a height of 1 m above the ground as to not underestimate rainfall due to interception from surrounding vegetation. Three flumes (F2, F3, and F4) were installed within the watershed to measure intra-watershed channel flow. These flumes were further utilized as outlets when partitioning the watershed for subbasin characterization. Miniflumes used to measure subbasin flow were procured from within the Jornada Experimental range and were previously utilized in surface flow research projects within the basin (Wainwright et al., 2002). Miniflume dimensions are shown in Figure A.2 of the supplemental material. Watershed outlet runoff was measured using a large flume (F1) which was previously installed. Measurements were taken by a pressure transducer (Campbell Scientific, CS450) located within the stilling well of each flume.

Spatially varied environmental sampling of soil moisture and temperature, rainfall, and runoff was supplemented by the installation of a 10 m tall eddy covariance tower (To). The tower was used to characterize surface and atmospheric energy, heat, carbon dioxide, and water fluxes as well as other meteorological and surface environmental parameters within an area representative of the watershed’s vegetative and geomorphic characterization. The tower was located on the eastern edge of the watershed

(Figure A.1). Tower measurements included precipitation at ~3 ft height (Texas Electronics, TE525); net long and short wave radiation at a ~5 m height (Kipp & Zonen, CNR2-L); incoming solar radiation at a height of ~5 m (Campbell Scientific, CMP3-L); sensible heat, latent heat, and carbon fluxes at a ~7 m height (Campbell Scientific, CSAT3 and LICOR, LI7500); air temperature and humidity at a ~1.5m height (Campbell Scientific, HMP45C); barometric pressure (Setra, CS100); soil surface temperature (Apogee Instruments Inc, SI-111 Infrared Radiometer); 2 and 4 cm depth soil temperature (Campbell Scientific, TCAV-L thermocouple); bare soil and vegetation shaded soil heat flux with measurements taken 0.05 m below the surface (Hukseflux, HPF01-SC); and 5 cm, 15 cm, 30 cm, and 50 cm depth volumetric soil moisture (Campbell Scientific, CS616). Precipitation measurements were sampled at tip resolution. Measurements required for latent, sensible, and carbon dioxide flux processing were sampled at 20Hz intervals while all other data was averaged or sampled at 30 min intervals. 20 Hz sampling of the three dimensional sonic anemometer and open-path gas analyzer insured maximum data resolution. The datalogger program used for sampling at the tower is provided in supplemental material, Appendix B. All equipment was cleaned every 3 weeks to reduce buildup of foreign materials on sensor lenses which might affect measurements.

A telemetry network was installed in March of 2011 for the remote monitoring of real-time datasets. A Campbell Scientific RF450 spread spectrum radio was installed at each of the 5 datalogger locations (F1, T1, T2, T3, and To). Data from each transect datalogger and the outlet flume datalogger were transmitted via a 900 MHz radio band to the tower. Transmitted data and tower data was then routed through a network link (Campbell Scientific, NL100). Network consolidated data was then transmitted from the tower to the Jornada headquarters through a TCP/IP link (Ubiquiti Networks Inc., Bullet

M2HP) for higher throughput. Once received at the Jornada headquarters, the data was routed through the New Mexico State University network and was easily accessible through a virtual private network using Loggernet software (Campbell Scientific).

2.3 Digital Terrain Map Production and Vegetation Classification

Digital terrain mapping and vegetation classification were accomplished by a team of New Mexico State University (NMSU) scientists lead by Andrea Laliberte and Albert Rango. An autonomous unmanned aerial system (UAS) was deployed over the

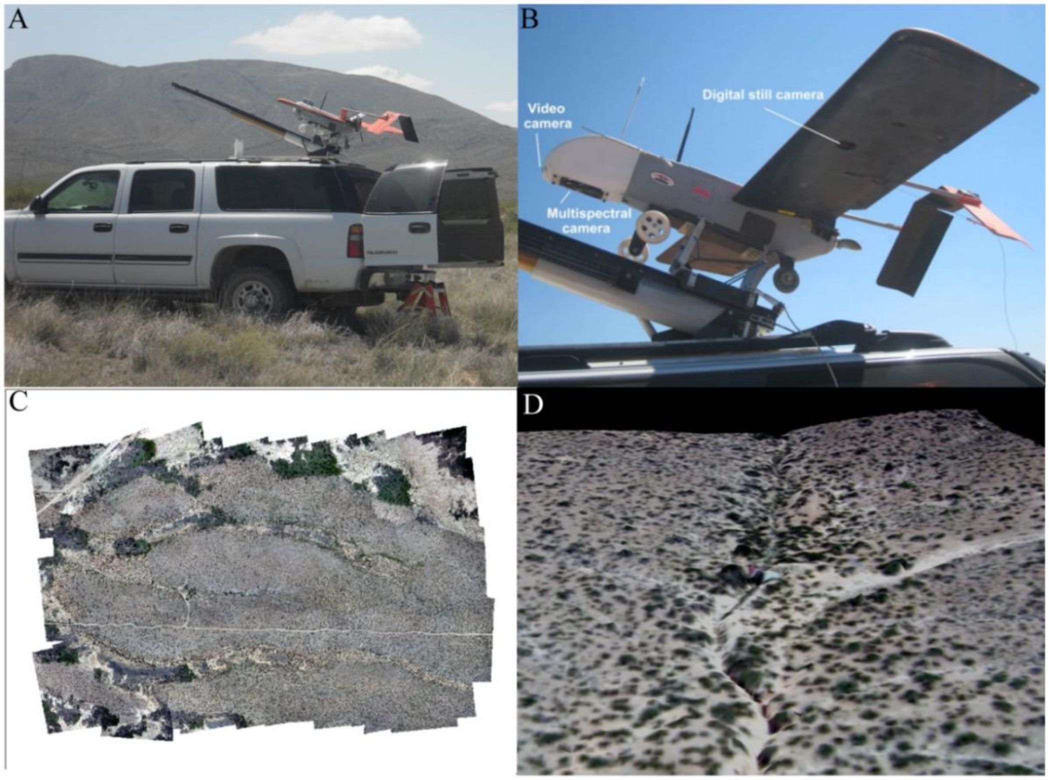

Figure 4: DTM creation from aerial photographs taken by the MLB BAT3: (a) launching platform for the BAT3; (b) the BAT3 has a mounted video camera for real-time monitoring of terrain, a multispectral camera for easily distinguishing vegetated areas, and a digital still camera for aerial photographs for later use in creating an area mosaic; (c) a completed mosaic of the watershed and surrounding areas; and (d) initial DTM creation (point of view is from watershed outlet looking eastward up the main channel).

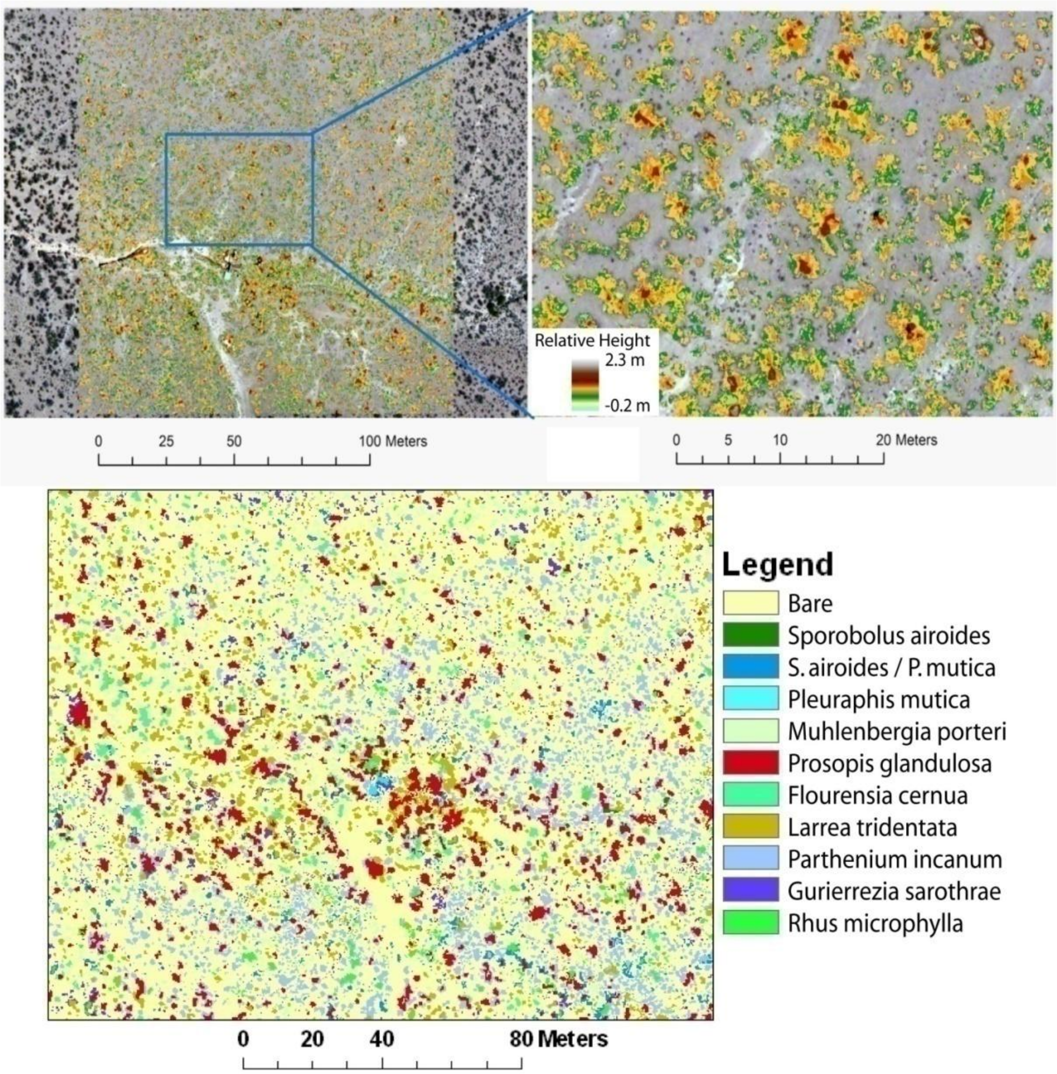

Figure 5: A subsample of the vegetation classification map for the watershed. The area shown in these images is just north of the outlet flume. Vegetation classification utilizing the eCognition 8 software depends on vegetation structure and color signature.

watershed to collect aerial photographs of the site at a height of approximately 200 m. The UAS utilized was the BAT 3 (MLB Co., Mountain View CA) with a mounted Canon SD 900 ten megapixel digital camera (Figure 4). An orthomosaic was created from overlapping aerial photos (75% forward lap and 40% side lap). Orthorectification was accomplished using a unique method called Presync developed by the NMSU research group (Laliberte et al., 2008), followed by mosaicing of the imagery using Leica

Photogrammetry Suite (LPS®) (Erdas 2010). Vegetation classification to the species scale was accomplished through the analysis of the orthomosiac by the program eCognition® 8 (Definiens, 2009) (Figure 5). Classification is based on plant or plant group structure and the Red, Green, and Blue spectrum signature (RGB) associated with these structures and is calibrated from field sampling. A more detailed description of the DTM creation and vegetation classification is described by Laliberte and Rango (2011). Previous vegetation classification utilizing this method in the Jornada basin has produced results with an average accuracy of 78% at the species level, and 81% at the structure group level.

2.4 Data Processing

All raw data was processed to assure high quality. Half-hourly averaged soil moisture datasets obtained from soil moisture measurements (Stevens Water Monitoring Systems, Hydra Probe) were transformed to volumetric soil moisture (m^3/m^3) values via the 'loam soil' type factory calibration equation to coincide with the dominant soil type found in the Tromble watershed (Seyfried et al., 2005). The equation utilized for calculation using the measured dielectric values of the soil is:

$$\theta = A + BE_r + CE_r^2 + DE_r^3 \qquad \text{Equation 1}$$

where θ is soil moisture [m^3/m^3]; E_r is the real dielectric permittivity of the soil; and A, B, and C are coefficients dependent on soil properties.

For all analyses, periods of interrupted measurements for individual probes resulted in either removal of periods of compromised data from the entire dataset, or removal of the individual probe data entirely for the period of analysis. In order to calculate spatially averaged soil moisture, the watershed was separated via the main channel network into 3 sections: the north-facing slope, the south-facing slope, and the west-facing slope. Each slope was separated into 5 bins based on elevation. Elevation weighted soil moisture was then calculated for each slope at the three sampled depths with each of the 5 transect soil moisture locations corresponding to one of the 5 elevation bins. Watershed averaged soil moisture was then calculated by the area-weighted average of slope soil moisture. Finally, profile averaged soil moisture was calculated by treating the measured 5cm soil moisture as average soil moisture over the top 10 cm of soil, measured 15 cm soil moisture was treated as the average soil moisture over the depth of 10-20 cm, and measured 30 cm soil moisture was treated as the average soil moisture over the depth of 20-40 cm. This weighted averaging method was also used when performing soil temperature analyzing the basin averaged responses of soil temperature at the 3 depths sampled.

Upon installation, each Texas Electronic tipping bucket rain gauge was calibrated statically to insure accuracy of individual tip volumes. Watershed-scale spatially averaged precipitation was calculated using the R2, R3, and R4 rain gauges (Appendix A). The watershed outlet and tower rain gauges (R1 and R5 respectively) were omitted from spatially averaged calculations due to a few periods of equipment malfunction over the sampling timeframe. A watershed bound Theissen polygon map was created based on rain gauge location to calculate contributing area-weighted, spatially averaged rainfall.

Pressure transducers sampled gauge pressure within the stilling wells of each flume at 1 min intervals. Flume pressure transducers provided pressure differential measurements for the stilling well relative to local atmospheric pressure as psig. Following installation, calibration of each pressure transducer was performed by relating pressure differential measurements to water height within the main stem of the flume. A linear calibration curve was created in the general form of:

$$h = m * p + b \qquad \text{Equation 2}$$

where h is the height of the water in the flume [cm], m is the rate of change of height with pressure change [cm/psig], p is measured pressure [psig], and b is the height offset [cm]. Diurnal changes in measurements due to heat fluctuations forced us to normalized runoff events prior to onset. In order to calculate individual storm event hydrographs, data was clipped to 30 minutes prior to the precipitation initialization and one hour following completion. Initial pressure measurements were normalized to a value of zero two minutes prior to precipitation onset to account for temperature fluctuation effects on pressure readings. The calibration curve formula supplied above was applied to normalized values. Flow for each miniflume was then calculated using the International Organization for Standards (ISO) protocol 4359 which determines flow rates based on flume dimensions and water height. Outlet flume flow was calculated using the previously determined height vs. flow equation listed below:

$$\mathrm{Q} = 0.08068 * \mathrm{h} + 4.307 * \mathrm{h}^2 \qquad \text{Equation 3}$$

Data from the three-dimensional sonic anemometer and open-path gas analyzer on the eddy covariance tower were first filtered to remove rainfall periods and periods of equipment malfunction. Data was then despiked for any samples which were 3+ standard deviations of the mean calculated on a monthly basis. Next, signal lag was removed and subsequent 30 min block averaging was performed. Coordinate plane rotation (Wilczak et al., 2001), stability, and density fluctuation (Webb et al., 1980) corrections were also performed prior to calculation of finalized fluxes. Sensible heat flux was calculated using the sonic temperature (Schotanus et al., 1983). Fluxes were then examined visually for erroneous data periods. For those 30-min flux periods which were manually removed due to extreme values, linear interpolation of data was performed to gap-fill. Negative latent heat flux values were set equal to zero. Despiking, corrections, and 30 min flux calculations were performed using the EdiRe data software tool (The University of Edinburgh). EdiRe software is a tool for processing raw microclimatological eddy covariance datasets which is fully customizable with a user friendly graphical interface.

Soil heat flux at the surface was calculated using the HFP01SC sensors with overlying TCAV soil thermocouples and a shallow soil moisture probe. The heat flux plate measures heat flux at depth (8 cm) while the soil thermocouple monitors the overlying soil temperature change. Shallow soil water content (5 cm) is used with shallow soil temperature dynamics to compute soil storage above the heat flux plate. Soil heat flux at the surface is then calculated by adding the measured flux at depth to the energy stored in the soil above the plate.

2.5 Water Balance Closure and Evapotranspiration Estimation

Watershed scale water balance calculations were performed using precipitation (P), runoff (Q), soil water storage change (ΔS), and evapotranspiration (ET). The following steady-state water balance equation was utilized for all calculations of water balance residuals or closures:

$$P = Q + \Delta S + ET \qquad \text{Equation 4}$$

Table 2: Missing Observation periods for all datasets between 6/1/2010 – 10/1/2011.

Start Date	**Start Time**	**Finish Date**	**Finish Time**
Raw Fluxes			
6/6/2010	17:00	6/25/2010	11:30
8/5/2010	16:30	8/23/2010	18:00
8/24/2010	17:00	8/26/2010	12:00
8/27/2010	6:30	9/8/2010	17:30
12/9/2010	12:30	1/3/2011	10:30
2/2/2011	0:00	3/11/2011	12:30
4/8/2011	10:30	4/13/2011	14:00
5/11/2011	14:30	5/12/2011	11:30
20 Hz Fluxes			
6/1/2010		8/2/2010	17:27
8/5/2010	17:29	8/23/2010	18:17
8/24/2010	18:19	8/26/2010	12:47
8/27/2010	8:19	9/4/2010	10:17
10/22/2010	12:16	10/22/2010	18:44
12/9/2010	11:46	1/3/2011	10:52
2/2/2011	0:29	3/11/2011	12:51
5/11/2011	13:45	5/12/2011	11:48
Weir Rain Gauge			
7/8/2010		8/24/2010	
Transect 1			
9/4/2010	11:00	9/7/2010	12:30
4/8/2011	11:00	4/12/2011	11:30
Transect 2			
9/4/2010	11:00	9/7/2010	12:30
4/8/2011	11:00	4/12/2011	11:30
Transect 3			
9/4/2010	10:30	9/7/2010	12:30
4/8/2011	11:00	4/12/2011	11:30
Meteorological Dataset			
8/5/2010	14:00	8/23/2010	18:00
8/24/2010	18:30	8/26/2010	12:00
8/27/2010	6:30	9/8/2010	17:30
12/9/2010	12:30	1/3/2011	10:30
2/1/2011	23:00	3/11/2011	12:30
4/8/2011	10:30	4/13/2011	14:00
5/11/2011	14:30	5/12/2011	11:30
Tower Rain Gauge			
6/1/2010		8/24/2010	
8/29/2010		8/31/2010	
10/7/2010		10/22/2010	

Plant water storage is not measured in this study and is unlikely to influence monthly or annual water balance calculations due to the lengthy time periods and the low vegetation coverage in the watershed (~34%). Spatially averaged precipitation and soil storage were calculated as previously discussed, while runoff was determined from outlet measurements of channel flow.

Evapotranspiration was calculated at 30 min intervals for the entire sampling period from latent heat flux (λE). For those periods when equipment failure occurred at the tower (Table 2), the Hargreaves method for calculating daily ET was utilized:

$$ET_0 = 0.0135(KT)(R_a)(TD)^{0.5}(TC + 17.8) \qquad \text{Equation 5}$$

where ET_0 is the Hargreaves evapotranspiration estimate [mm/day], KT is an empirical coefficient which varies based on environment vegetation and precipitation regimes, R_a is extraterrestrial solar radiation, TD is the difference between daily maximum and minimum temperature, and TC is the average daily temperature (Hargreaves and Samani, 1982; Hargreaves and Samani, 1985). KT values were determined for the watershed by comparing ET values calculated from tower data to ET_0 values for periods of field observed λE. λE data was separated into 'wet' and 'dry' periods where watershed averaged soil moisture was > 0.1 m^3/m^3 and < 0.1 m^3/m^3 respectively. The best correlations when comparing ET to ET_0 for wet and dry periods occurred when KT = 0.195 and KT = 0.0184 respectively. Daily ET_0 estimates are given in Appendix I. Monthly error values (ε) for the water balance were calculated using the formula:

$$\epsilon = P - Q - \Delta S - ET \qquad \text{Equation 6}$$

We also perform the Scott (2010) approach of comparing monthly water balance derived ET to those measured using the eddy covariance method. In order to perform this analysis, Scott (2010) calculated ET from field measured values of P, Q, and ΔS by using the equation:

$$ET = P - Q - \Delta S \qquad \text{Equation 7}$$

In this study we expand this comparison by analyzing spatial mismatches between the point-scale water balance derived ET (ET_{Tower}) as Scott calculated it, using a distributed dataset for a basin-averaged water balance derived ET (ET_{Basin}), and using the in-situ sampled eddy covariance derived ET (ET_{EC}). In order to calculate ET_{Tower} using the equation listed above, precipitation and ΔS were measured at the point-scale where the single sampling location for both was at the tower. ET_{Basin} was calculated using spatially averaged P and ΔS, where each constituent was calculated using the methods described in section 2.4. In both cases Q was measured at the watershed outlet. ET_{EC} was treated as a standard by which the accuracy of ET_{Tower} and ET_{Basin} could be compared.

I also analyzed the importance of utilizing a distributed dataset in the calculation of ET at the daily scale using a different method of ET calculation. For this method field measured data is used to create an ET vs. soil moisture (θ) relationship. Again, 2 scenarios were tested, 1) where tower based point-scale θ dataset and ET_{EC} were used to create one relationship and 2) the spatially averaged, distributed θ dataset and ET_{EC} were used to create a second relationship. The creation of each ET vs. θ relationship followed the multivariate approach to calculate the soil moisture hygroscopic point (θ_H), the soil moisture wilting point (θ_W), the soil moisture at maximum ET (θ^*), evapotranspiration at the wilting point (ET_W), and maximum evapotranspiration (ET_{MAX}) simultaneously as established by Vivoni et al. (2008). Following the creation of each of these piecewise linear relationships, ET was calculated from θ using each relationship for the point-scale dataset and the distributed dataset. Accuracy of daily ET calculations were then compared against ET_{EC}.

2.6 Energy Balance Closure

Energy fluxes were summed at the monthly and annual scale to determine the individual contributions of incoming solar radiation (I_S), net longwave and shortwave radiation (R_n), latent heat (λE), sensible heat (H), and ground heat (G) fluxes. Furthermore, seasonal energy flux components were averaged at 30 minute intervals to determine the diurnal dynamics of each component throughout the year. Ground heat flux was sampled in a bare soil region and under vegetation canopy (n =2). In order to represent intra-watershed ground flux dynamics, bare soil and under canopy measurements were averaged weighted by the fraction of vegetation coverage within the watershed using the following equation:

$$G_{avg} = 0.34 * G_{UC} + 0.66 * G_{BS} \qquad \text{Equation 8}$$

where G_{avg} is the weighted average ground heat flux used for energy balance calculations, G_{UC} is ground heat flux measured beneath vegetation canopy, and G_{BS} is ground heat flux measured in bare soil. In order to address the issue of unaccounted for energy when calculating the energy balance, an error term (ε) was calculated on the monthly scale using the equation:

$$\varepsilon = R_n - \lambda E - H - G \qquad \text{Equation 9}$$

Furthermore, seasonal albedo (α) was calculated from net shortwave radiation (SW) and incoming solar radiation (I_S) using the formula:

$$\alpha = 1 - \frac{SW}{I_S} \qquad \text{Equation 10}$$

2.7 Point-Scale Model Application

Calibration and numerical simulation of hydrologic processes were tested for 2011(3/11 – 10/1) and 2010 (5/25 – 8/5) periods respectively utilizing the physically based hydrologic model the TIN-based Real-time Integrated Basins Simulator (tRIBS) (Ivanov et al., 2004; Vivoni et al., 2007a). The model is fully distributed and captures topographic, land-use, and soil features of the basin of interest by partitioning the basin using a TIN. Each TIN node is associated with Voronoi polygons for finite volume domain calculations of local hydrologic responses such as vegetation interception, partitioned ET, soil water infiltration and redistribution, and surface water flow (Vivoni et al., 2010). A more detailed description of the model can be found in Ivanov et al. (2004).

For the purposes of this thesis, a single Voronoi polygon centered at the eddy covariance tower was used for the point-scale modeling (3606407.8 m N, 349528.8 m E, 1469.4 m). The soil depth at the tower was set to 0.9 m with a soil texture of loam utilized for modeling. Soil texture and bulk density were determined through laboratory analysis of field samples from the tower location. Other soil hydrologic parameters utilized for model calibration and simulation were determined using the soil classification software suites SoilPar (Acutis and Donatelli, 2001; Acutis and Donatelli, 2003) and

Rosetta (USDA ARS). All utilized model soil parameters for the 2010 and 2011 simulated runs are given in Appendix H.

Land surface characteristics were also used to parameterize the model. Surface albedo was determined at the tower using the method described by equation 10 for tower measured IS and SW. Vegetation coverage was determined by using the UAV derived vegetation characterization dataset, whereby the percent coverage over the entire watershed was calculated from aerial maps and was assumed to represent the tower modeled location. Further land cover parameterization was based off of similarly determined values from Vivoni et al. (2010) and calibrated to match the 2011 summer dataset.

The summer 2011 calibrated model was utilized for a trial run of 2010 to determine the point-scale model accuracy. Residual soil moisture, albedo (Al), and optical transmission coefficient (Kt) values were altered between the two years to reflect watershed changes between the 2 summer periods. Simulated results for each summer period were compared against field observations in order to calculate 4 error metrics: 1) correlation coefficient (CC), efficiency error (E), bias (B), and mean absolute error (MAE) (Vivoni et al., 2006). The following equations were utilized for calculation of each error metric:

$$CC = \frac{\sum_{i=1}^{N}(O_i - \bar{O})(F_i - \bar{F})}{\left[\sum_{i=1}^{N}(O_i - \bar{O})^2\right]^{0.5}\left[\sum_{i=1}^{N}(F_i - \bar{F})^2\right]^{0.5}} \qquad \text{Equation 11}$$

$$E = 1 - \frac{\sum_{i=1}^{N}(O_i - F_i)^2}{\sum_{i=1}^{N}(O_i - \bar{O})^2} \qquad \text{Equation 12}$$

$$B = \frac{\bar{F}}{\bar{O}} \qquad \text{Equation 13}$$

$$MAE = \frac{1}{N}\sum_{i=1}^{N}|O_i - F_i| \qquad \text{Equation 14}$$

where the number of observations = N for field observed (O) values and forecasted (F) values.

3. RESULTS AND DISCUSSION

3.1 Watershed Characterization

Despite research occurring within the Jornada basin for > 100 years, the watershed in which we research had limited previous physical characterization. In order to perform high resolution characterization of land-atmospheric exchanges, it was imperative that we gain insight into the topographic and vegetative identity of the region.

Remote UAS terrain analysis using the MLB BAT3 allowed for the creation of a 1-m DTM as well as watershed vegetation characterization. A watershed elevation map is shown with relative sensor locations in Figure 6. Minimal relief change occurs throughout the watershed (Table 3). Shrub encroachment on historically grass dominated lands has been an important focus of research in the Jornada basin due to a strong shift from a grassland dominated environment to shrub domination in the last 100 years (Fredickson et al., 2006; Okin et al., 2006). Remote vegetation characterization followed by ground verification showed that larger shrubs were the dominant vegetation

Table 3: Watershed elevation as determined by ArcGIS. Cell sizes are 1-m x 1-m.

	Elevation	
Elevation [m]	# of Cells	Coverage [%]
1452-1454	1855	3.97
1454-1456	3819	8.17
1456-1458	6543	14.0
1458-1460	10238	21.9
1460-1462	8740	18.7
1462-1464	6337	13.6
1464-1466	4994	10.7
1466-1468	3149	6.74
>1468	1059	2.27
All	46734	100

types in the Tromble watershed (Table 4). The most dominant plant species within the watershed were mariola, mesquite, and creosote while grasses only covered approximately 5% of the watershed. Remote vegetation characterization closely mimicked the results seen by 3 hillslope vegetation characterization transects performed on 5/25/2010. For this characterization a 70 m long transect was analyzed on each of the three primary hillslopes where vegetation coverage was sampled every 1 m. This characterization resulted in an average bare soil coverage across the three transects of ~61% of the total sampled area and large shrubs such as mariola, creosote, tarbush, and mesquite accounting for ~77% of the total vegetation. The heterogeneity of a shrub dominated environments has proven to also lead to heterogeneities in soil moisture. While Hennessey et al. (1985) found no significant differences in soil moisture in the Jornada between mesquite vegetated plots and bare soil plots at 15 cm depth, at 30 cm depth vegetated plots were found to have significantly less soil moisture. Soil moisture disparities due to shrub encroachment can not only perpetuate further heterogeneities through juvenile vegetation recruitment control, but it can also alter local hydrology in the form of altering soil water storage reserves and infiltration rates.

Historical attempts at watershed boundary delineation provided a crude representation of the watershed boundary based on visual delineation. The watershed boundary delineation provided in Figure 6 was created using the ArcGIS tool, ArcHydro (ESRI). Since this process is highly dependent on DTM resolution (Alcaraz et al., 2009), the procurement of the regional MLB BAT3 1-m resolution DTM was integral in accurate boundary delineation. Watershed area was found to be 46,734 m^2, with only 18 m of relief change occurring throughout the watershed. The hillslope north of the main channel of the watershed showed a fairly uniform aspect facing south-southwest while

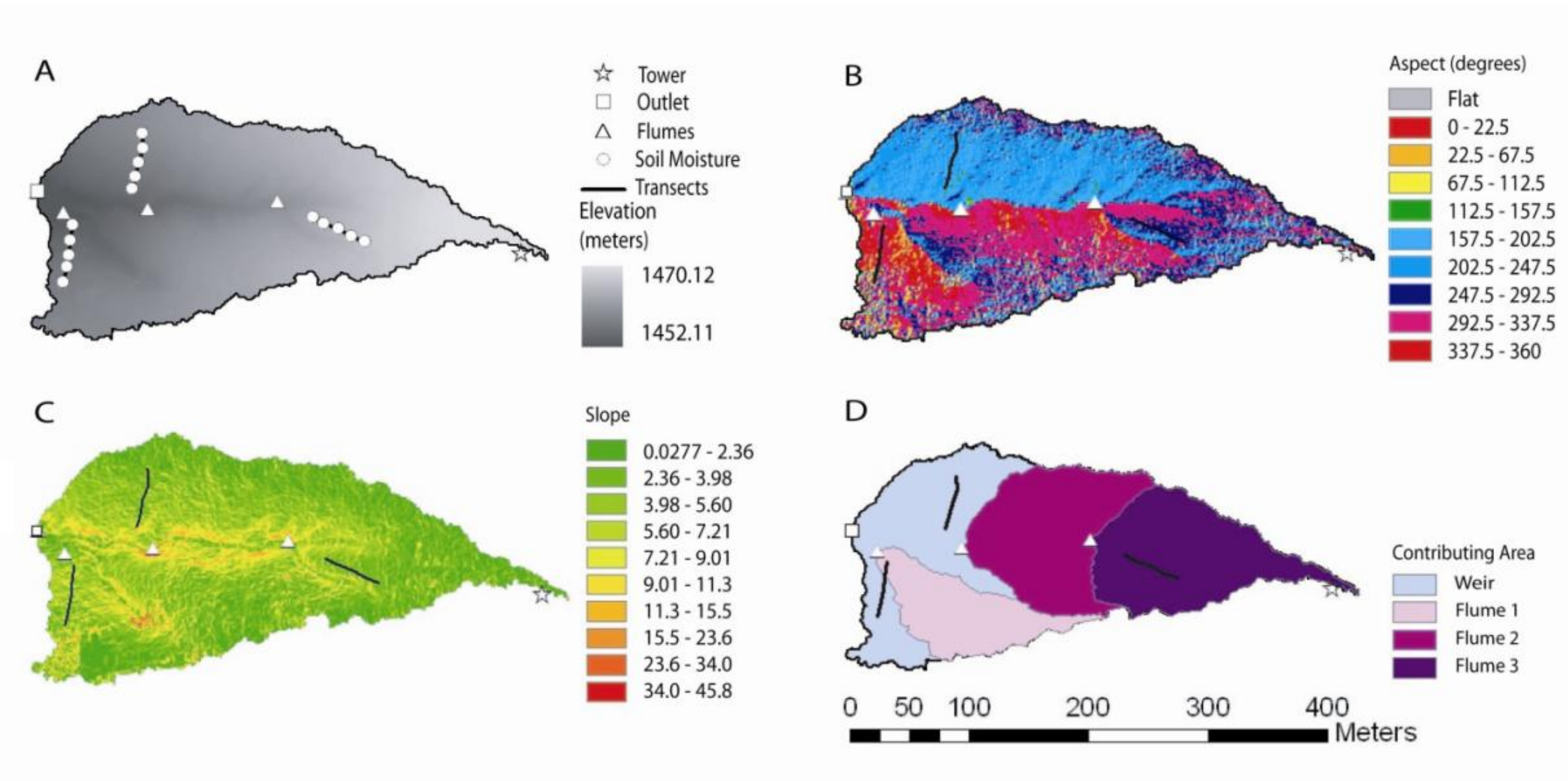

Figure 6: A topographic characterization of the watershed. Watershed delineation boundary is shown, as well as: A) sensor location and elevation, B) aspect in cardinal degrees from north, C) slope in degrees, and D) delineated subbasin extent with flumes serving as subbasin outlets.

Table 4: Watershed vegetation coverage as determined remotely using imagery from the UAS MLB BAT3 and through image processing by eCognition 8 software.

Watershed Vegetation Characterization	
Vegetation Species	Coverage [%]
Bare Soil	65.95
Parthenium incanum (Mariola)	11.94
Prosopis glandulosa (Mesquite)	6.47
Larrea tridentata (Creosote)	5.82
Muhlenbergia porteri (Bush Muhley)	2.89
Flourensia cernua (Tarbush)	2.48
Gurierrezia sarothrae (Snakeweed)	1.82
Pleuraphis mutica (Tobosa Grass)/*Sporobolus sp.* (Dropseed)	1.40
Rhus sp. (Sumac)	1.15
Sphaeralcea angustifolia (Globe Mallow)	0.04
No Data	0.02

Table 5: Watershed aspect, as determined for each cardinal direction using ArcGIS. Cell sizes are 1-m x 1-m.

Aspect		
Cardinal Direction	# of Cells	Coverage [%]
North	6869	14.7
Northeast	1777	3.80
East	643	1.38
Southeast	852	1.82
South	5401	11.6
Southwest	12005	25.7
West	9493	20.3
Northwest	9694	20.7
All	46734	100

Table 6: Characterization of each soil probe sensor location. All values were determined from 1 m x 1 m sensor cell characteristics within ArcGIS. Cardinal direction is based on the aspect of the cell.

Sensor Location Characterization					
Sensor	Subbasin Location	Aspect [^{o}]	Cardinal Direction	Slope [^{o}]	Elevation [m]
SM1	Flume 1	329.75	NW	5.40	1453.68
SM2	Outlet	322.07	NW	3.05	1454.90
SM3	Outlet	305.93	NW	6.34	1455.80
SM4	Outlet	352.44	N	3.41	1456.82
SM5	Outlet	216.06	SW	2.77	1457.34
SM6	Outlet	197.79	S	7.62	1456.04
SM7	Outlet	207.96	SW	4.24	1456.90
SM8	Outlet	203.46	SW	3.97	1457.69
SM9	Outlet	221.29	SW	6.33	1458.62
SM10	Outlet	260.96	W	2.66	1459.04
SM11	Flume 3	296.33	NW	5.51	1462.28
SM12	Flume 3	265.49	W	3.61	1462.89
SM13	Flume 3	253.34	W	4.28	1463.72
SM14	Flume 3	259.98	W	5.65	1464.36
SM15	Flume 3	288.49	W	2.14	1465.02

Table 7: Watershed slope as determined by ArcGIS. Cell sizes are 1-m x 1-m.

Slope		
Slope (Degree)	# of Cells	Coverage [%]
0-2.36	9186	19.7
2.36-3.98	12847	27.5
3.98-5.60	11631	24.9
5.60-7.21	6985	15.0
7.21-9.01	3461	7.41
9.01-11.3	1764	3.77
11.3-15.5	719	1.54
15.5-23.6	106	0.23
23.6-34.0	30	0.06
>34.0	5	0.01
All	46734	100

the hillslope south of the main channel had a more variable aspect due to the intrusion of two main channel tributaries (Table 5). The varied aspects of the north-facing hillslope led to soil moisture transect 1 having aspects of individual sampling locations which varied between 216-352^{O} while soil moisture transect 2, located on the more uniform south facing hillslope, had individual sampling locations which only varied in aspect from 198-260^{O}. Transect 3 was located on a small ridge on the west-facing hillslope which varied in sampling location aspects between 253-296^{O}. The uniformity of aspects on the south- and west-facing slopes indicate that during storm events, surface and groundwater flow would be more likely to originate from the same upslope regions for all sampling locations. However, due to variability of aspects within the transect 1 footprint, it is more likely that the sampling locations located on this transect would have storm water contributions which originate from multiple locations. Excluding channel banks, slope analysis showed consistently low values throughout the watershed and the surrounding terrain (Table 7). Due to relatively flat terrain surrounding the tower, net vertical wind speed should approach zero as is required by one of the major assumptions of eddy flux calculation (Burba and Anderson, 2010). Subbasin delineation using miniflumes and the outlet flume as pour points resulted in comparably sized basins (Table 8).

Table 8: Surface area of each delineated subbasin.

Subbasin Area	
Basin/Subbasin	Area [m^2]
Watershed Outlet	13,128
Flume 1	7,747
Flume 2	12,754
Flume 3	13,105
Watershed Area	46,734

3.2 Basin-Averaged Temporal Dynamics

Seasonal variability of hydrological processes and energy fluxes play an important role in semiarid regions in the southwestern US due to increased precipitation, incoming solar radiation, and vegetation greening during the NAM season. While in most ecosystems summer plant productivity is highly dependent on winter rainfall (Snyder et al., 2004), the plant species productivity within the NAM is mostly dependent on summer rainfall (Schwinning et al., 2004) and the intra-seasonal temporal distribution of summer rainfall (Austin et al., 2004; Sher et al., 2004). The increase in summer solar radiation strongly controls seasonality in sensible and ground heat fluxes, while the in-phase nature of seasonal radiation, maximum yearly rainfall, and vegetation greening provide conjunctive efforts for an increased seasonal response of latent heat flux during the NAM period.

The presence of the NAM at the Tromble watershed was highly evident during 2010 and 2011. During the 2010 fall, 2011 winter, and 2011 spring (i.e., 10/1/2010 – 6/30/2011) only 20 mm of rainfall fell, while the 2010 and 2011 summer periods (i.e., 7/1/2010 – 9/30/2010 and 7/1/2011 – 9/30/2011) experienced 113 mm of rainfall and 202 mm of rainfall respectively. This resulted in elevated 5 cm, 15 cm, and 30 cm soil moisture for the entire watershed for the NAM summer periods when compared to non-NAM seasons (Figure 7). 5 cm soil moisture was highly dependent on total storm precipitation and the interstorm period length. During the fall (Figure 8), winter (Figure 9), and spring (Figure 10) seasons all depths of basin-averaged soil moisture were consistently lower than during the NAM season (Figure 11). However, summer interstorm periods which exceeded one week resulted in 5 cm soil moisture approaching values similar to those sampled during the dry season. Even though 15 cm soil moisture

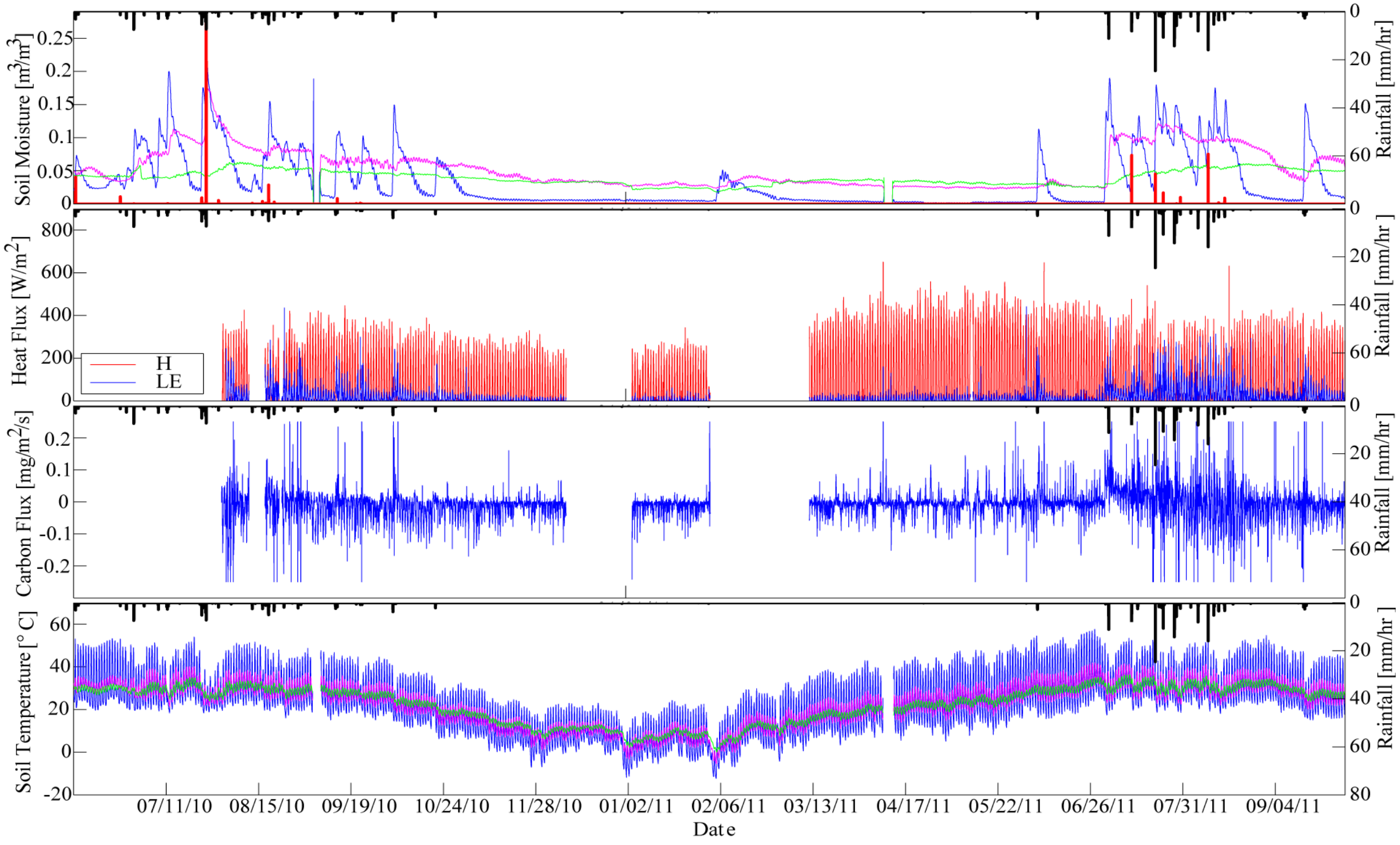

Figure 7: 2010-2011 time-series of water, energy, and CO_2 dynamics, beginning in the 2010 summer (6/6/2010) and ending in the 2011 summer (9/31/2011). The top image shows the spatially averaged 5, 15, and 30 cm soil moisture for the watershed; the 2nd image down shows the latent and sensible heat fluxes; the third image from the top shows the carbon flux; and finally, the temporal dynamics of watershed averaged soil temperature for 5, 15, and 30 cm depths are shown in the final plot. Gaps indicate periods of equipment failure.

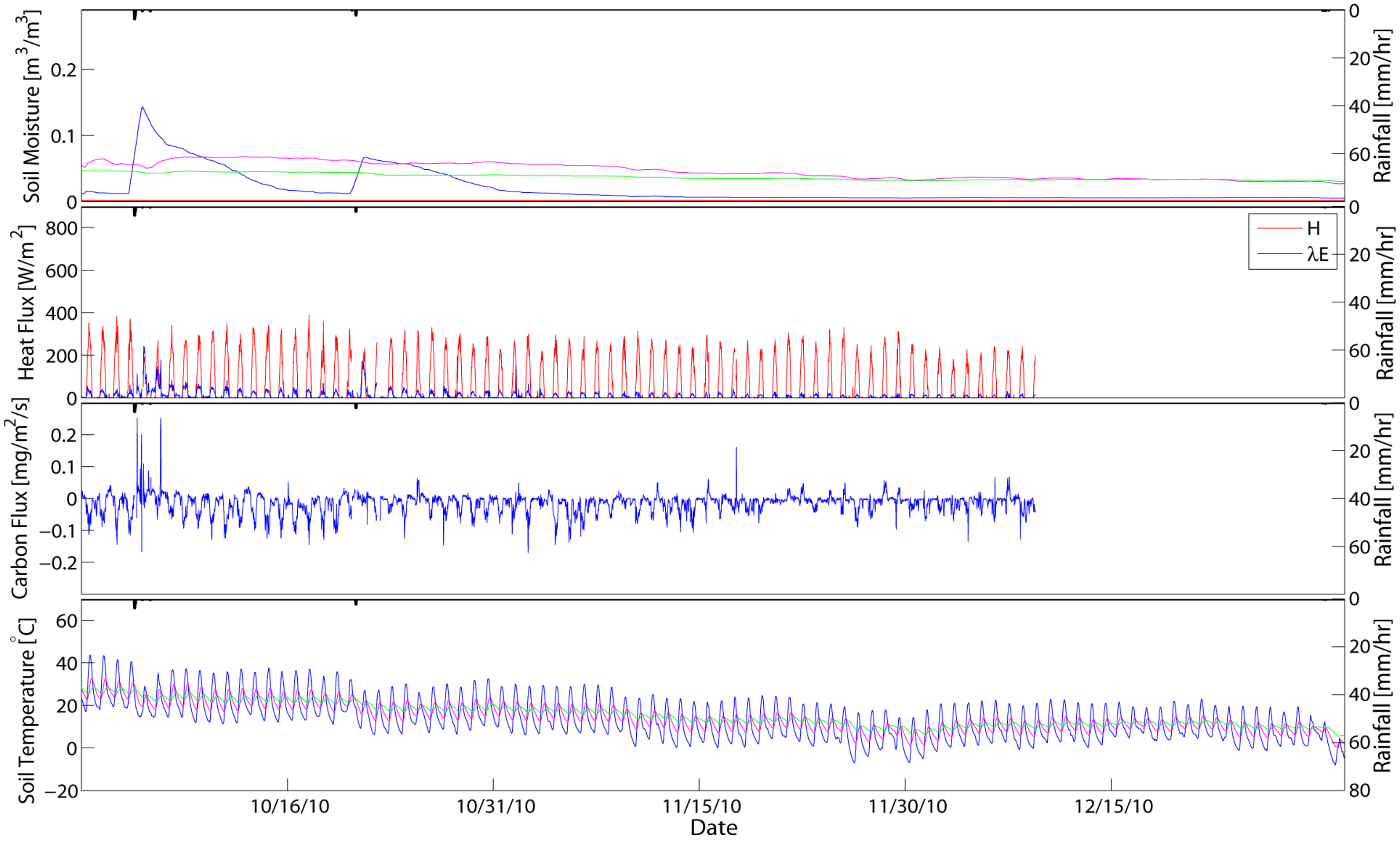

Figure 8: 2010 fall time-series (10/1/2010 – 12/31/2010) of water, energy, and CO_2 dynamics. The top image shows the spatially averaged 5, 15, and 30 cm soil moisture for the watershed; the 2nd image down shows the latent and sensible heat fluxes; the third image from the top shows the carbon flux; and finally, the temporal dynamics of watershed averaged soil temperature for 5, 15, and 30 cm depths are shown in the final plot. Gaps indicate periods of equipment failure.

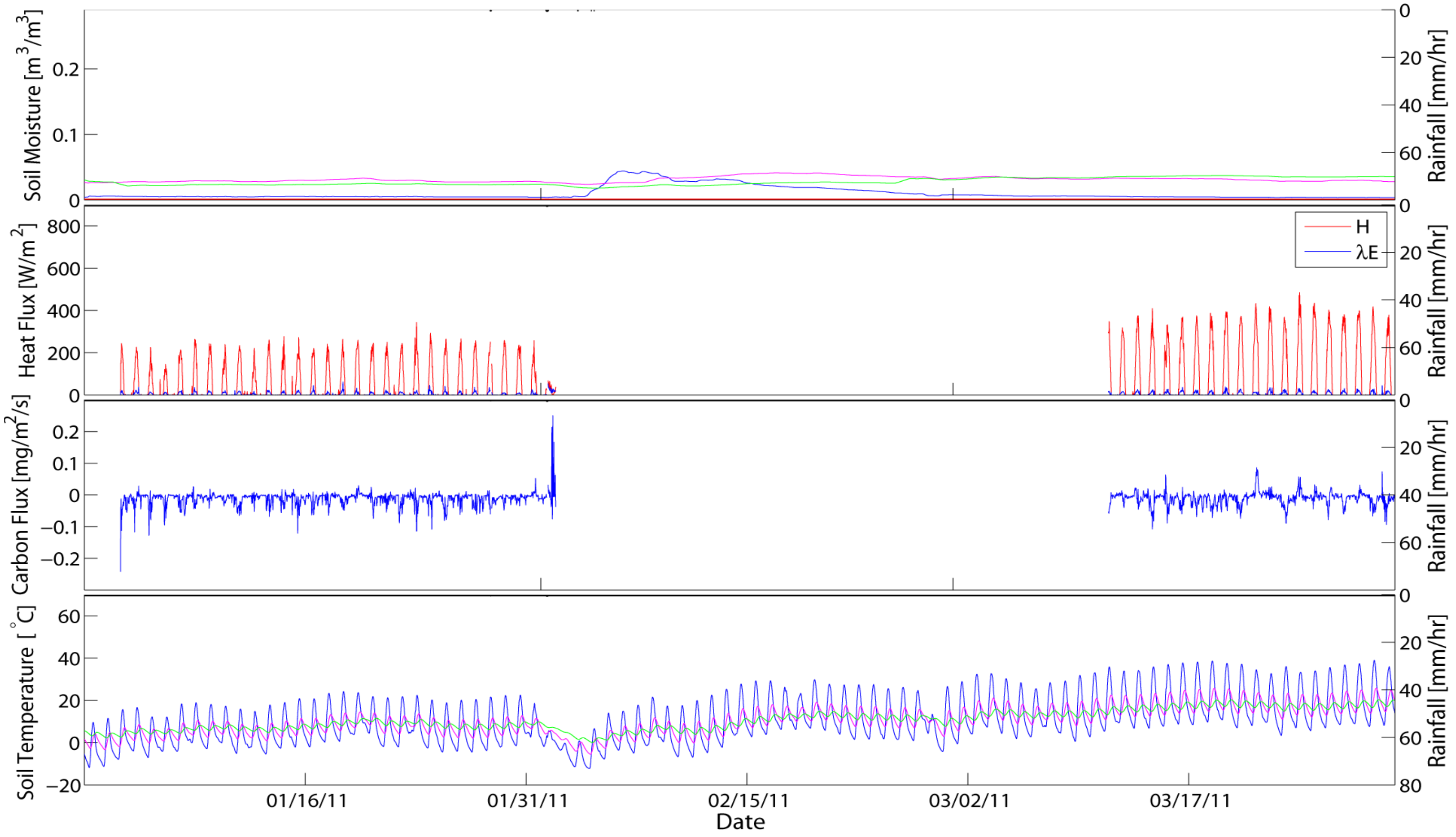

Figure 9: 2011 winter time-series (1/1/2011 – 3/31/2011) of water, energy, and CO$_2$ dynamics. The top image shows the spatially averaged 5, 15, and 30 cm soil moisture for the watershed; the 2nd image down shows the latent and sensible heat fluxes; the third image from the top shows the carbon flux; and finally, the temporal dynamics of watershed averaged soil temperature for 5, 15, and 30 cm depths are shown in the final plot. Gaps indicate periods of equipment failure

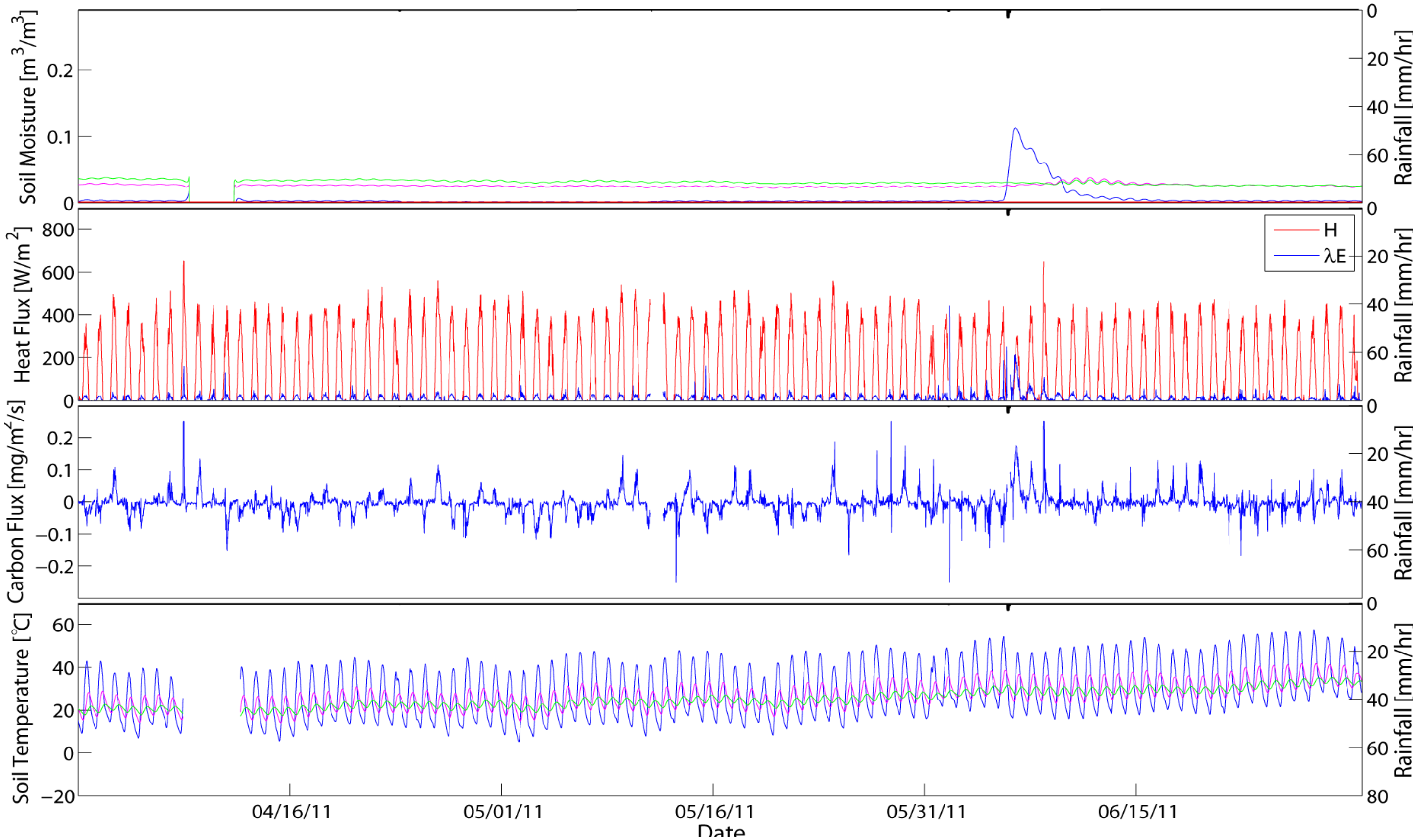

Figure 10: 2011 spring time-series (4/1/2011 – 6/30/2011) of water, energy, and CO_2 dynamics. The top image shows the spatially averaged 5, 15, and 30 cm soil moisture for the watershed; the 2nd image down shows the latent and sensible heat fluxes; the third image from the top shows the carbon flux; and finally, the temporal dynamics of watershed averaged soil temperature for 5, 15, and 30 cm depths are shown in the final plot. Gaps indicate periods of equipment failure.

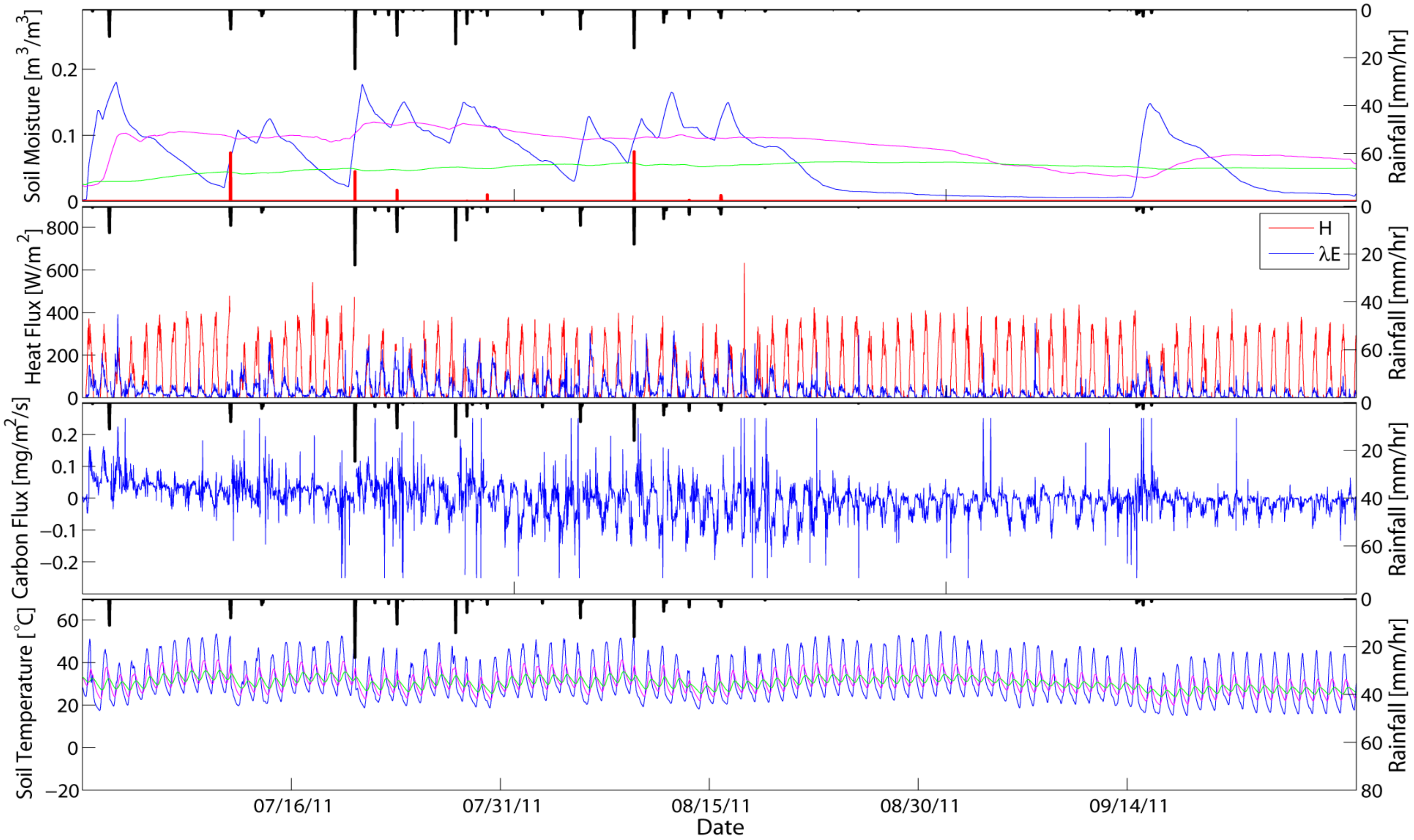

Figure 11: 2011 summer time-series (7/1/2011 – 9/30/2011) of water, energy, and CO_2 dynamics. The top image shows the spatially averaged 5, 15, and 30 cm soil moisture for the watershed; the 2nd image down shows the latent and sensible heat fluxes; the third image from the top shows the carbon flux; and finally, the temporal dynamics of watershed averaged soil temperature for 5, 15, and 30 cm depths are shown in the final plot. Gaps indicate periods of equipment failure.

was much more responsive to precipitation pulses than 30 cm soil moisture, both depths reached a similar dry seasonal minimum of soil moisture. Comparison of fall, winter, and spring 15- and 30-cm soil moisture shows that towards the end of the winter and the beginning of the spring seasons 15 cm soil moisture begins to fall below that of 30 cm soil moisture. The inactivity of soil moisture dynamics at the 30 cm depth for most of the year indicates little recharge occurs below 30 cm depth. Since most of the watershed has a well defined caliche layer just below this 30 cm mark, it is possible that water storage in the caliche layer occurs during the NAM season and could be slowly released during the dry seasons. This method of deep soil moisture replenishment from caliche nodules was suggested by Hennessy et al. (1983), who found that caliche nodules extracted from Jornada soils have a saturated water content of 27% by volume. However, it is unknown if the caliche layer would retain enough water storage to last an entire dry season.

Watershed runoff, presented in Figures 7-11, was measured at the watershed outlet and was highly dependent on seasonal increases in storm recurrence intervals and antecedent soil moisture. During the entire sampling period there were only 2 runoff occurrences when basin averaged 5 cm soil moisture did not exceed 0.1 m^3/m^3 (n = 18). These two runoff events were also the only 2 events when runoff did not occur during the NAM period. The lack of runoff events (Figure 7) shows that even though the watershed had a well defined channel system, the watershed only provides surface flow to downstream regions during extreme storm events or during periods of prolonged wetness. This indicates that changes in precipitation patterns with increasing storm intensity but decreasing occurrence, as predicted by the IPCC (2007), may result minimal change or possibly slightly increased runoff activity in the watershed. Since few runoff events currently occur on a yearly basis, decreases in rainfall occurrence could result in minimal effect on the annual runoff totals, while increased storm intensity could greatly increase total runoff from each storm event.

Energy fluxes are highly dependent on solar radiation and precipitation. Sensible heat shows a strong seasonal shift with yearly maximums occurring during the dry early spring and yearly minimums occurring during the wet periods and the late fall and winter. Precipitation notwithstanding, sensible heat nearly doubles during the shift from winter (~200W/m^2 daily maximums) to the spring and summer seasons (~400W/m^2 daily maximums) (Figure 7). Latent heat flux is limited by the lack of soil moisture throughout the year with daily maximums usually reaching ~60 W/m^2 during dry periods. Storm periods result in latent heat maximization and can lead to the latent heat fluxes exceeding sensible heat fluxes for short periods immediately following rainfall events. Immediately following rainfall events, latent heat can meet and exceed 250 W/m^2. Latent heat flux is maximized during the summer season when precipitation and solar radiation also reach yearly highs.

Huxman et al. (2004) described the complex relationship between rainfall pulses and carbon flux pulses in semiarid ecosystems by noting that for small rainfall pulses soil microbial activity increases significantly, resulting in pulse carbon releases in the environment. Huxman et al. (2004) expands on this by stating that if the rainfall pulses are large enough, vegetation will respond and the resulting effect will be that the environment will act as a carbon sink due to increased photosynthetic activity. Seasonal analysis of carbon flux for the fall 2010 (Figure 8) and spring 2011 (Figure 10) periods in the Tromble watershed indicate that small rainfall pulses during dry periods tend to result in increased microbial respiration. Analysis of summer 2011 carbon fluxes exhibit a trend whereby larger rainfall events result in immediate increases in soil respiration followed by delayed, increased photosynthetic activity. This carbon flux shift could play an interesting role in the degree to which photosynthetic activity increases following large rainfall events. The immediate increase in atmospheric CO_2 following a large storm event could fuel increased rates of photosynthetic activity for the local vegetation. Once the infiltrated rainfall is available for plant usage, atmospheric CO_2 pools have increased to allow for increased photosynthetic rates. Regional shifts in precipitation patterns could result in plant community structure changes in the future, regardless of changes in precipitation amount (Knapp et al., 2002). In the study period from 2010 – 2011 the region was found to respond as a carbon sink, uptaking an average of 164 grams of C for every m^2 of land annually. Vegetation community changes could alter the region's carbon uptake rates.

The water balance for the watershed was calculated on the monthly scale to determine the distribution of precipitation into runoff, evapotranspiration, and soil water storage. Evapotranspiration dominated the water balance accounting for 138% of rainfall over an 11 month period. Evapotranspiration occurred at greater rates than soil water storage change in dry months (Figure 12). This discrepancy was likely due to rainfall underestimation because of undercatch (Larson and Peck, 1974) or release of soil water storage from caliche deposits and utilization by vegetation (Hennessy et al., 1983). The only month to show increases in soil water storage was July 2011, which marked the beginning of the monsoon season. The time it took for vegetation to green and start maximizing soil water usage allowed for the increased storage seen in this month; however, lower precipitation in the following 2 months resulted in the largest negative net storage changes of soil water storage seen throughout the year. Runoff represents a very small portion of incoming rainfall and primarily occurs during the NAM season. Over the 11 month period analyzed, runoff represented 0.39% of the total incoming

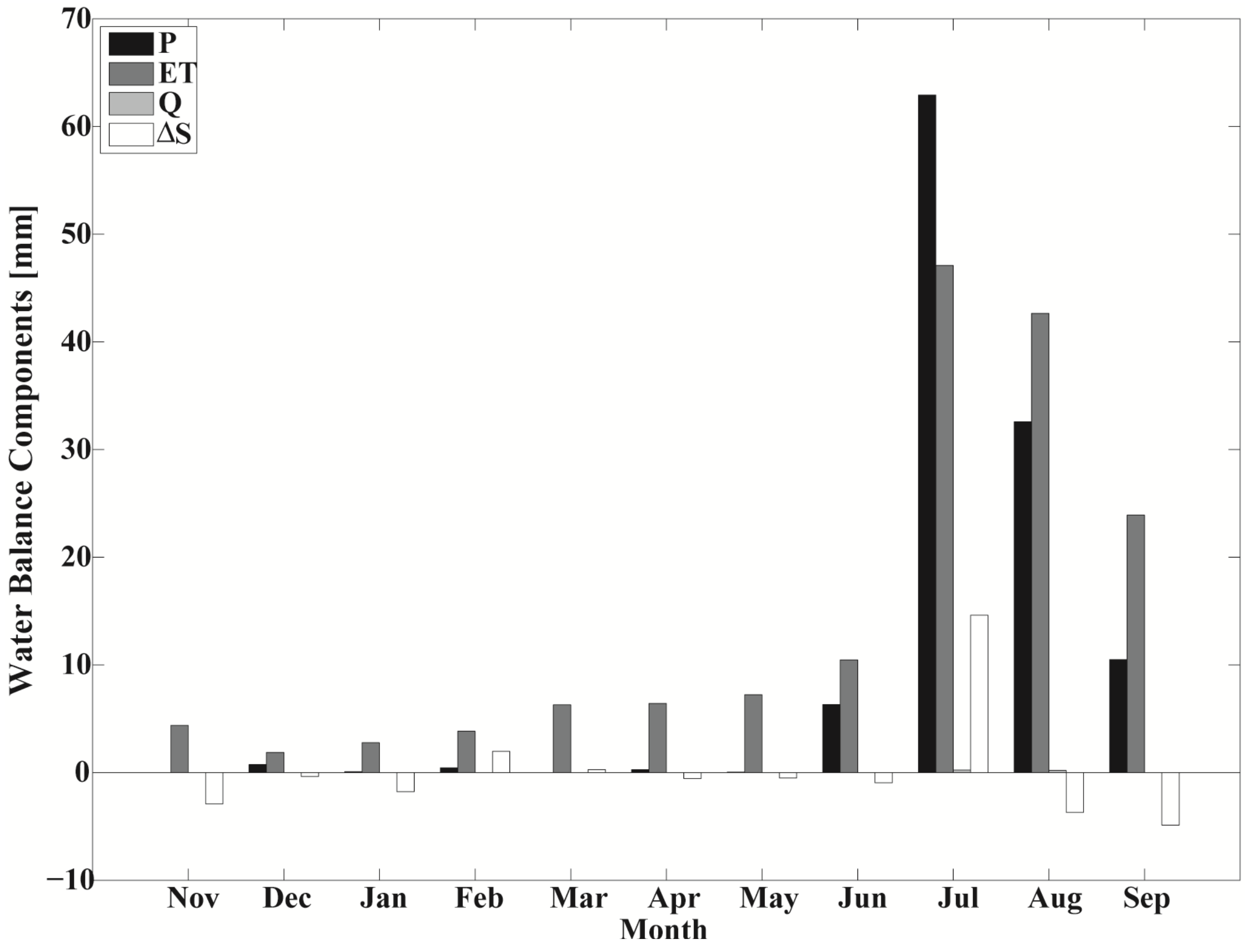

Figure 12: Total monthly water balance components as summed over the entire sampling period. Spatially averaged precipitation (P), runoff (Q) as measured at the outlet flume, evapotranspiration (ET), and soil water storage change (ΔS) were measured directly or calculated.

Table 9: Total summed monthly water balance components [mm]. Spatially averaged precipitation (P), runoff (Q) as measured at the outlet flume, evapotranspiration (ET), and soil water storage change (ΔS) were measured or calculated as previously described. Error terms represent the discrepancy between precipitation and the sum of all other components.

Year	Month	P	Q	ET	ΔS	Error
2010	Nov	0.00	0.00	4.38	-2.90	-1.48
2010	Dec	0.74	0.00	1.87	-0.36	-0.77
2011	Jan	0.09	0.00	2.77	-1.77	-0.91
2011	Feb	0.43	0.00	3.84	1.98	-5.39
2011	Mar	0.00	0.00	6.29	0.27	-6.56
2011	Apr	0.27	0.00	6.41	-0.55	-5.60
2011	May	0.04	0.00	7.23	-0.50	-6.69
2011	Jun	6.32	0.00	10.46	-0.95	-3.19
2011	Jul	62.93	0.24	47.09	14.63	0.97
2011	Aug	32.57	0.20	42.64	-3.70	-6.57
2011	Sep	10.49	0.00	23.91	-4.89	-8.53

precipitation (Table 9). Evapotranspiration is the major component to soil moisture depletion and mimics seasonal trends in soil moisture (Figures 8-11) with minimal values in the pre-NAM winter and spring months and maximums in the summer when radiation and precipitation are maximized. Monthly errors in the water balance (Table 9) were comparable to yearly values calculated by Scott (2010). Like Scott, our errors were negative indicating an underestimation of precipitation relative to evapotranspiration.

Scott (2010) compared ET calculations from the eddy covariance method to those derived from calculating ET from the water balance and found comparable results indicating the effectiveness of the eddy covariance method in calculating evapotranspiration. He attributed the error seen between the two methods to 3 factors: 1) underestimation of precipitation, 2) slope changes in the environments sampled, and 3) the spatial scale mismatch between the water balance estimated ET and the eddy

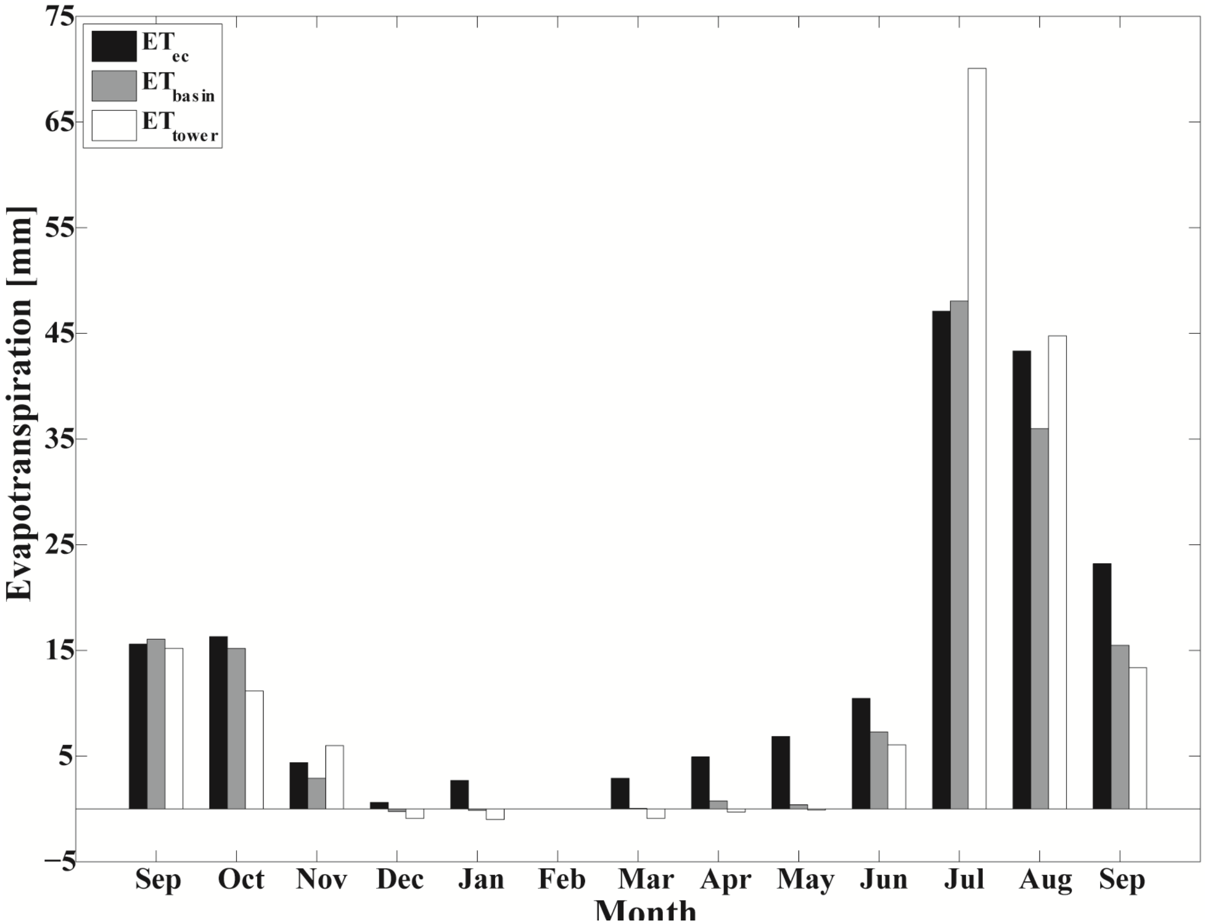

Figure 13: Monthly comparison (9/2010 – 9/2011) of evapotranspiration calculated using the eddy covariance method (ET_{ec}), the water balance using basin-averaged soil moisture and precipitation measurements (ET_{basin}), and point-scale measurements of soil moisture and precipitation as measured at the tower (ET_{tower}).

Table 10: Seasonally averaged soil temperature [^{o}C] for summer (7/1/2010 – 9/30/2010 and 7/1/2011 – 9/30/2011), fall (10/1/2010 – 12/31/2010), winter (1/1/2011 – 3/31/2011), and spring (4/1/2011 – 6/30/2011). Depth averaged values were calculated from daily maximums of soil temperature for the 3 depths sampled across all locations. Profile averaged values were averaged over all sampled locations and weighted for each depth.

Season	5cm Avg.	5cm St. Dev.	15cm Avg.	5cm St. Dev.	30cm Avg.	30cm St. Dev	Profile Avg.	Profile St. Dev.
Summer	45.5	2.37	35.9	1.33	31.8	0.55	36.2	6.13
Fall	25.7	2.60	18.5	1.75	16.8	1.02	19.5	4.41
Winter	24.7	3.14	15.3	3.30	12.3	2.21	16.2	6.07
Spring	46.5	3.04	32.9	1.84	28.0	0.77	33.8	8.18

covariance calculated ET. We attempted to partially address the spatial scale mismatch by calculating ET from the water balance using basin averaged precipitation and soil moisture values (ET_{basin}) and using precipitation and soil moisture samples from the tower (ET_{tower}) and comparing both values against ET from tower eddy covariance measurements (ET_{EC}). The assumption is that the distributed ET_{basin} is more representative of ET_{EC} than the point-scale ET_{tower} due to the increased sampling area spatial scale agreement of ET_{basin} with ET_{EC} when compared to the point-scale measurements used for the ET_{tower} calculations. Over the 11 month period analyzed only August 2011 showed better agreement between ET_{tower} and ET_{EC} when compared to ET_{basin} vs. ET_{EC} (Figure 13). Absolute error (AE) between estimated ET values (e.g., ET_{tower} and ET_{basin}) and ET_{EC} where calculated at the monthly scale using the following equation:

$$AE = |ET_{EC} - ET_{EST}| \qquad \text{Equation 15}$$

where ET_{EST} represents either ET_{tower} or ET_{basin}. AE was then averaged over the period of analysis (9/2010 – 9/2011) to get an absolute average monthly error. The absolute average monthly error between ET_{EC} and ET_{basin} is 3.79 mm while the absolute average monthly error between ET_{EC} and ET_{tower} was 6.15 mm. We therefore see almost a doubling of ET estimation accuracy when moving from point-scale based calculations of ET to calculations made utilizing a distributed dataset of soil moisture and precipitation. This confirms Scott's assertion that spatial scale mismatch can cause error when calculating ET from the water balance. However, one assumption made in our comparison is that the entire basin is always representative of the tower footprint. Further work should address how to acquire representative soil moisture and rainfall sampling with the varying tower footprint size and direction.

Soil temperature was highly variable seasonally (Table 10). Shallow soil temperature (5 cm) was found to have the highest daily maximums averaged over the sampling period during the spring due to increased solar activity and decreased vegetation coverage. However, when samples were depth averaged, summer exhibited the highest soil temperature values annually. This is due deeper soil temperatures requiring more time to warm following a cold winter, when the 30 cm depth averaged only 12.3 ^{o}C daily maximums.

3.3 Event-scale analysis

High temporal and spatial resolution sampling within the watershed allow for unparalleled characterization of event-scale analyses. These analyses are imperative for defining the spatiotemporal resolution of environmental monitoring necessary for a complete representation of a small semiarid watershed during the NAM season when performing environmental monitoring. In this section we examine runoff production and

Table 11: Characteristics of four 2011 NAM season storm events. Period of analysis occurred from 30 minutes prior to the first rainfall to 24 hours following the final rainfall. Storm intensity = I, outlet runoff = Q, basin averaged precipitation = P, evapotranspiration = ET, soil water storage change = ΔS, peak runoff = Q_{pk}, runoff time to peak from initiation of storm = T_P, total runoff period = T_B, and lag time between the storm onset and runoff onset = T_L calculations are shown.

	7/11/2011	7/20/2011	7/23/2011	8/9/2011
Start Time	14:51	13:30	13:50	13:53
End Time	16:12	14:48	15:07	15:35
I [mm/hr]	5.01	14.21	5.58	5.47
Q/P outlet	0.0225	0.0012	0.0012	0.0076
Q/P flume 1	0.0025	0.0090	0.0037	0.0022
Q/P flume 2	0.0001	0.0170	0.0107	0.0244
Q/P flume 3	0.0001	0.0143	0.0047	0.0170
ET/P	0.2812	0.1404	0.3638	0.2920
ΔS/P	0.5695	0.4899	0.0674	0.3288
Q_{PK} [m^3/s]	0.0122	0.0075	0.0028	0.0125
T_P [min]	14	15	12	49
T_B [min]	24	15	13	59
T_L [min]	1	3	8	0
P [m^3]	318	868	337	437
Q [m^3]	9.12	1.37	0.48	4.26
ET [m^3]	89.4	121.8	122.5	127.6
ΔS [m^3]	181.1	425.2	22.7	143.7

soil moisture progression through the early 2011 NAM season. In particular we focus on 4 storm events: 7/11/2011, 7/20/2011, 7/23/2011, and 8/9/2011. These storm events span from the first major storm event of the NAM season well into the peak of the 2011 NAM season. All four storms produced runoff at the watershed outlet and were comparable in length and the time of day of their occurrences. Characteristics of these storm events are found in Table 11.

Partitioning of water balance components for the first major storm of the season (7/11/2011) resulted in the highest proportion of precipitation going to storage change

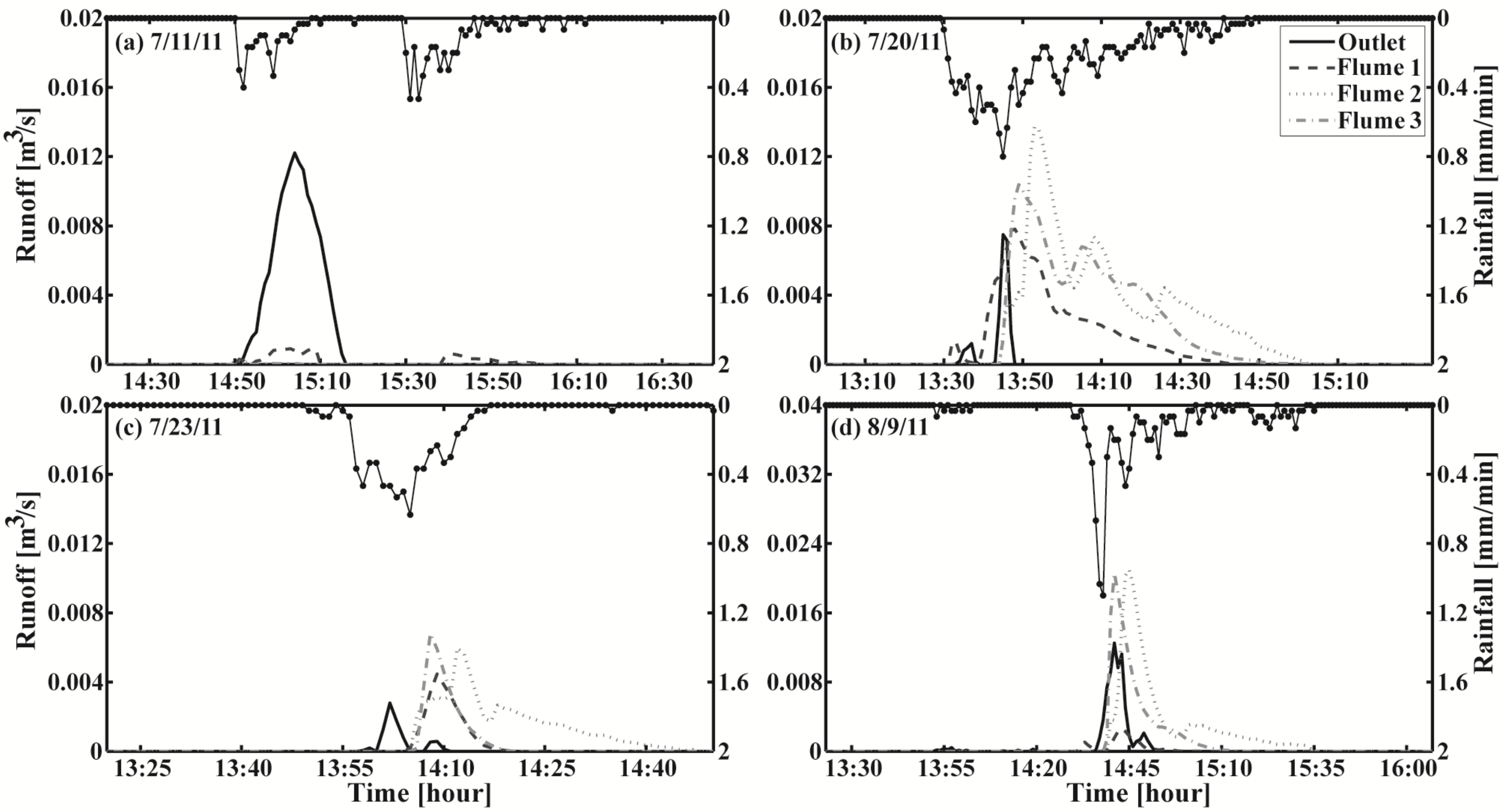

Figure 14: Spatial variation of runoff within the watershed through 4 storm events. The graphs above show the spatial variation within the watershed for the 4 flumes for the: a) July 11, 2011; b) July 20, 2011; c) July 23, 2011; and d) August 9, 2011 events.

($\Delta S/P$) and watershed runoff (Q/P) of any of the 4 storms analyzed. Since this is the first major storm of the season, soil moisture is low due to a pre-NAM drought period of about 9 months. High storage changes are seen for the first and second storm due to this low soil moisture. A much smaller storage change is seen for the 7/23/2011 storm due to a small interstorm period between the 7/20/2011 and 7/23/2011 storms leading to elevated soil moisture values at the storms onset. The long interstorm period between the third and fourth storms (i.e., 7/23/2011 and 8/9/2011) leads to an increased proportion of precipitation partitioning to soil water storage due to adequate time for soil dry down. Interestingly, watershed runoff in terms of 1) proportion of storm precipitation (Q/P), 2) peak runoff (Q_{PK}), and 3) total runoff show evidence of an inverse correlation when compared to storm intensity for the 4 storms. The 7/11/2011 and 8/9/2011 storms have the lowest rainfall intensity of any of the 4 storm periods analyzed, but have the highest Q/P, Q_{pk}, and ΣQ of the four storms shown. In contrast, these two storms had the highest interstorm period prior to precipitation onset of the four storms shown, which could indicate the watershed experiences refractory runoff production during periods of successive rainfall where for short periods immediately following one rainfall event, a successive rainfall event has reduced runoff production. One potential reason for this unexpected relationship could be due to soil seal formation. It has been discussed that in semiarid environments, soil seal formation can occur from raindrop impaction alone (Ben-Hur and Marcos, 2008). Seal formation is primarily due to the coalescence of clay particles at the soil surface (Lado and Ben-Hur, 2004). In the Jornada basin surface soil formation is primarily due to wind controlled soil redistribution. With a lengthy interstorm period, fine soil particles can be easily redistributed over the watershed by wind activities. At the beginning of a storm event the coalescence of the soil surface fines could form a surface seal leading to an increased chance of runoff. However, runoff production results in erosional processes. If the following interstorm period is not lengthy enough for wind controlled redispersion of fine soil particles, the next rainfall event could result in increased infiltration due to the lack of soil sealing. This phenomenon was further analyzed by reviewing all available runoff events during the sampling period. Analysis of the larger sample size of runoff events determined no distinguishable relationship between Q_{pk} and storm intensity, Q_{pk} and preceeding interstorm period, or Q_{pk} and initial profile-averaged soil moisture indicating some other environmental parameter is responsible for runoff formation or a combination of soil seal formation, storm intensity, and initial soil moisture may play a more complex role in runoff formation.

When soil water storage change does not dominate precipitation partitioning, ET is the major contributing component, as is the case for the 7/23/2011 storm. It is important to note that ET is only reported in Table 11 for a 24 hour period following rainfall completion. However, even for this short period, ET plays a major role in watershed scale redistribution of rainfall for each of the 4 storm periods shown. As this period increases in length soil evaporation and vegetation transpiration increases depleting soil storage and increasing the relative importance of ET in the water balance. Furthermore, ET increases for each successive storm indicating a hysteretic effect between initial NAM season soil moisture and vegetation production and transpiration as previously described by Vivoni et al. (2010).

Intra-watershed runoff shows high variability in total and peak runoff between the 4 flumes for the four storms presented in Table 11 (Figure 14). The outlet runoff experienced the highest runoff peak and total runoff for only the 7/11/2011 event. For 2 of the three remaining events the outlet experienced the lowest peak and total runoff, indicating channel losses are extremely important in this watershed. Channel runoff was

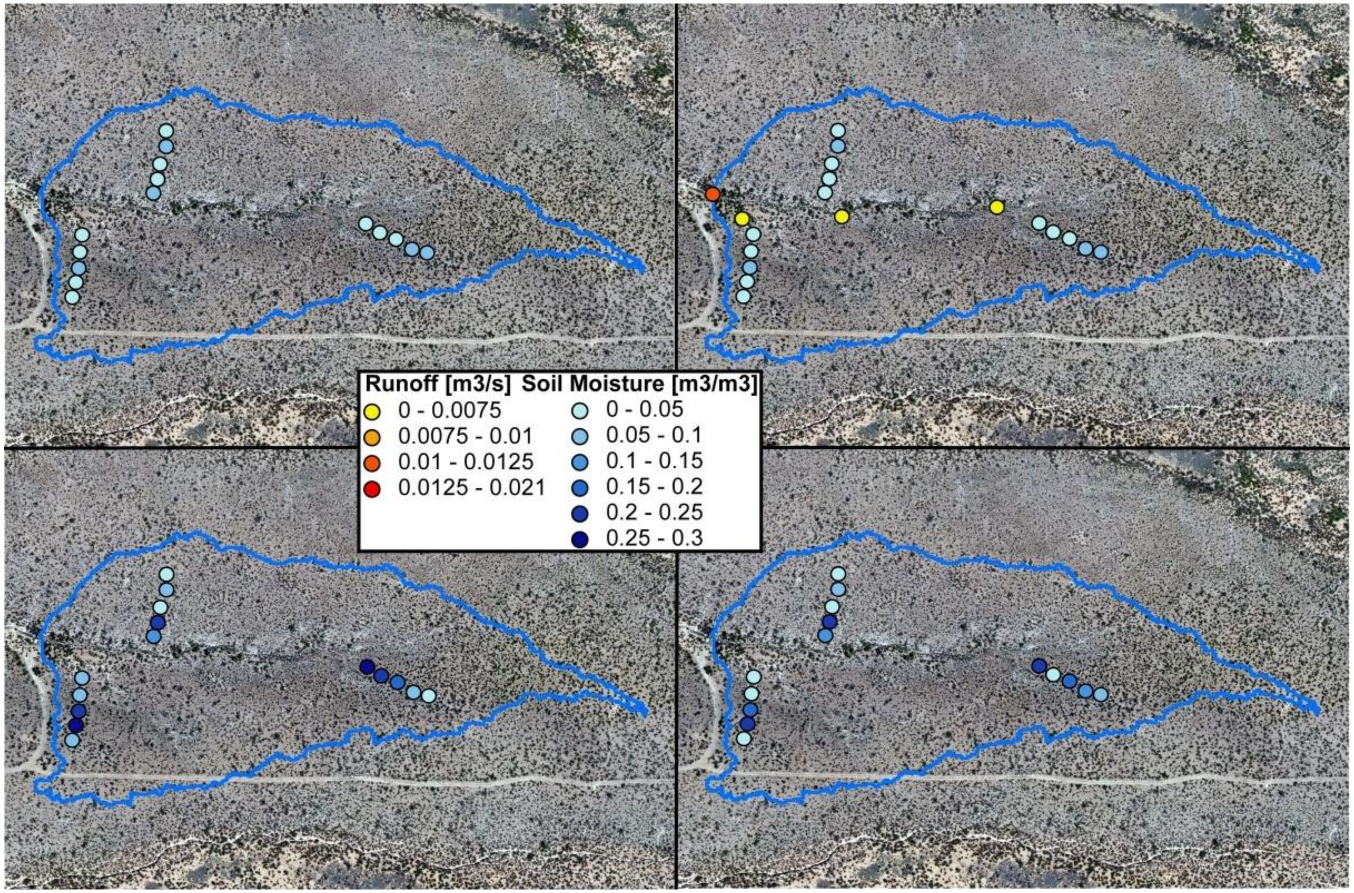

Figure 15: A map showing a 9-hour time-series of 5cm depth soil moisture for the 7-11-2011 event. The top left figure shows shallow soil moisture 1 hour prior to the event, the top right figure shows soil moisture during peak rainfall and the storm period’s peak runoff at each flume, the bottom left figure shows the shallow soil moisture 1 hour following the completion of the event, and the bottom right figure shows shallow soil moisture 8 hours after the completion of the event.

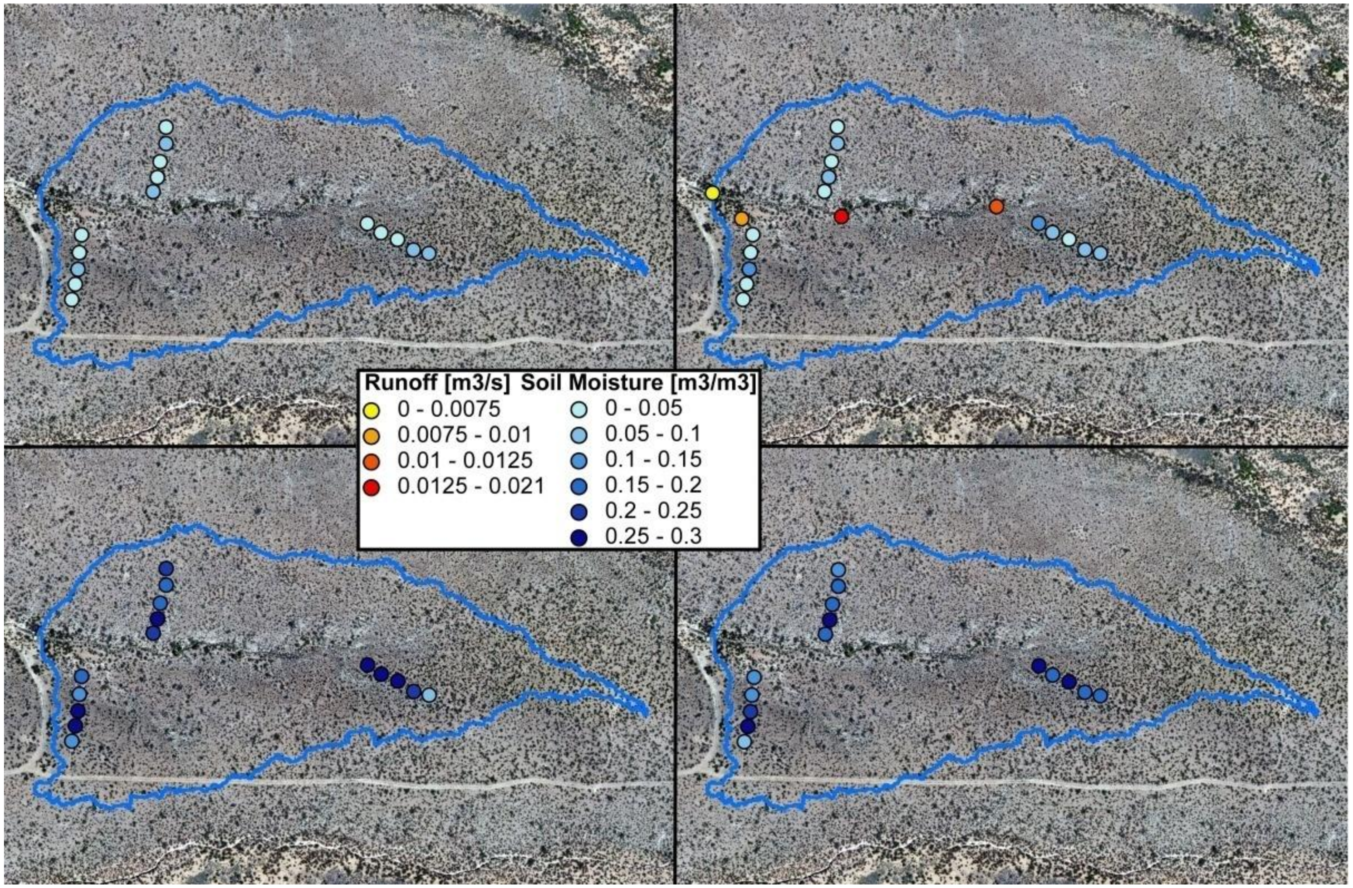

Figure 16: A map showing a 9-hour time-series of 5cm depth soil moisture for the 7-20-2011 event. The top left figure shows shallow soil moisture 1 hour prior to the event, the top right figure shows soil moisture during peak rainfall and the storm period’s peak runoff at each flume, the bottom left figure shows the shallow soil moisture 1 hour following the completion of the event, and the bottom right figure shows shallow soil moisture 8 hours after the completion of the event.

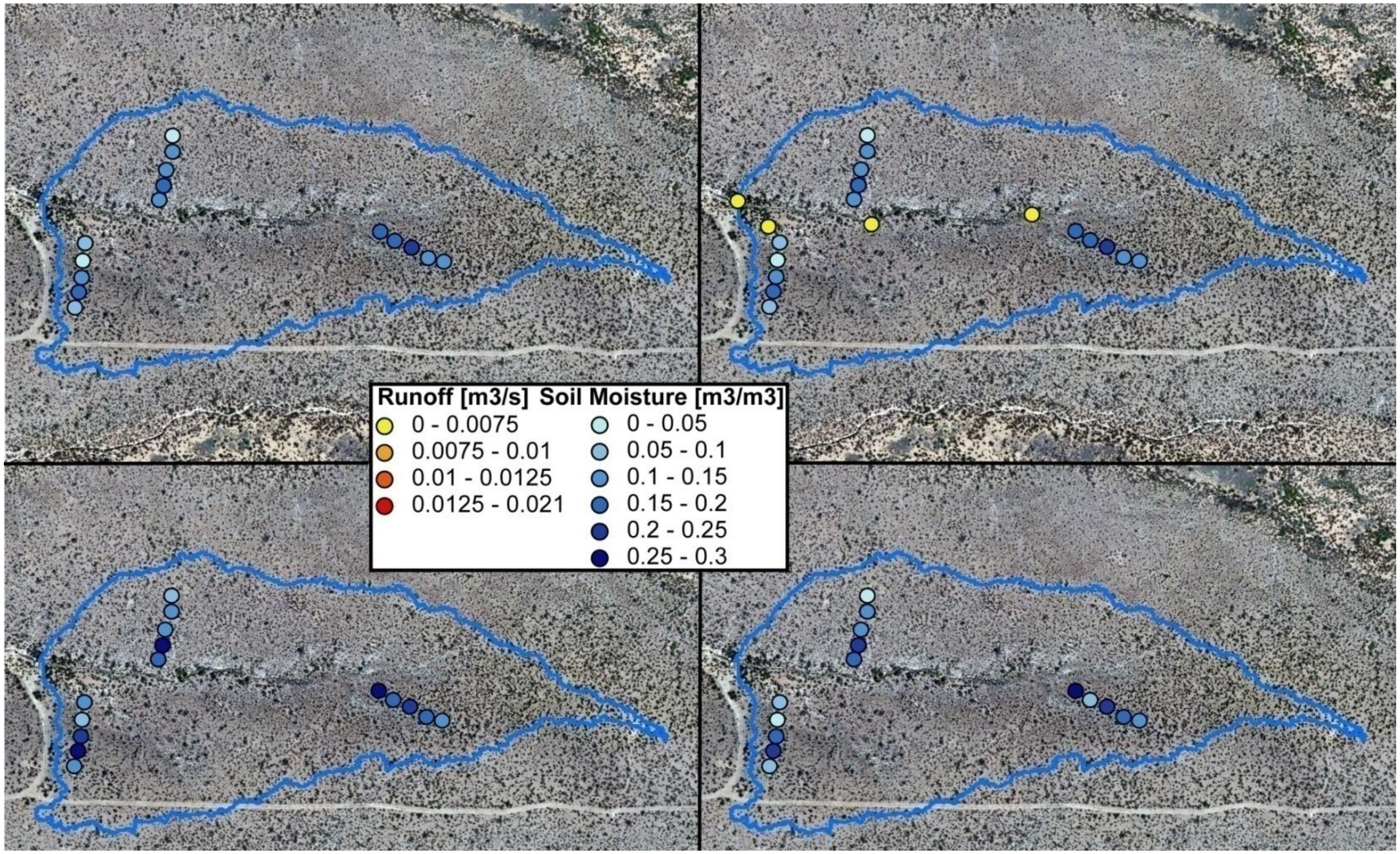

Figure 17: A map showing a 9-hour time-series of 5cm depth soil moisture for the 7-23-2011 event. The top left figure shows shallow soil moisture 1 hour prior to the event, the top right figure shows soil moisture during peak rainfall and the storm period's peak runoff at each flume, the bottom left figure shows the shallow soil moisture 1 hour following the completion of the event, and the bottom right figure shows shallow soil moisture 8 hours after the completion of the event.

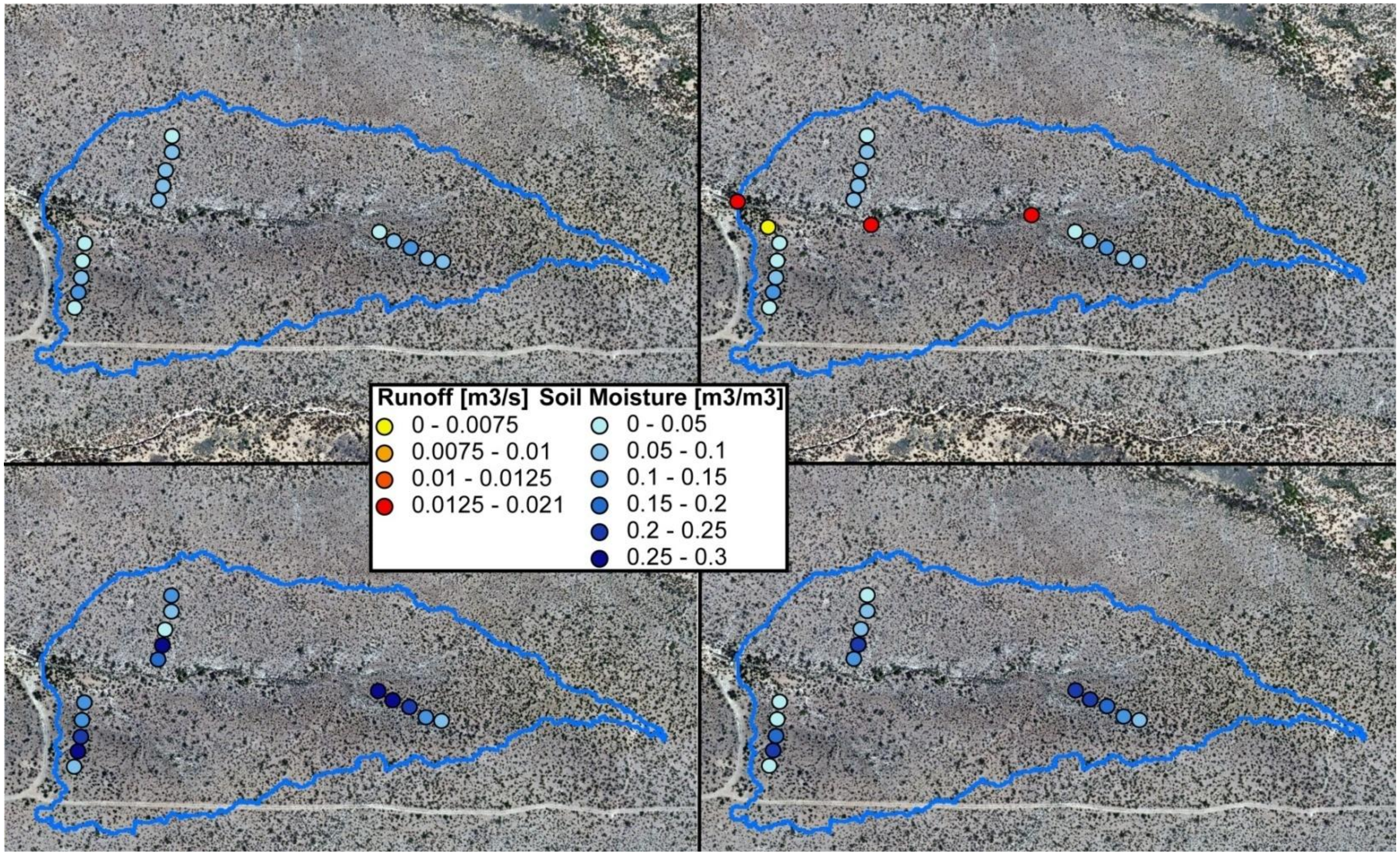

Figure 18: A map showing a 9-hour time-series of 5cm depth soil moisture for the 8-9-2011 event. The top left figure shows shallow soil moisture 1 hour prior to the event, the top right figure shows soil moisture during peak rainfall and the storm period's peak runoff at each flume, the bottom left figure shows the shallow soil moisture 1 hour following the completion of the event, and the bottom right figure shows shallow soil moisture 8 hours after the completion of the event.

previously presented as the greatest contributor to groundwater recharge in the climatically similar Walnut Gulch Experimental Watershed in Arizona (Renard, 1970). The channel bed directly upstream of the outlet is much looser and coarser soils than are any other soils found throughout the watershed which could lead to the high channel losses seen here. In contrast, the furthest upstream reaches of the main channel are caliche lined. Consequently, we can see that total runoff for each storm event increases from the 3rd flume to the 2nd flume indicating little to no channel loses in this portion of the watershed. When comparing the second and third flumes (located the furthest up the main channel) to the outlet flume, peak flow of the outlet flume is usually prior to peak flow of the second and third flume. The outlet flume experiences runoff patterns much more similar to the first flume (located in a large tributary which feeds into the main channel very close to the outlet). This indicates that little of the runoff which occurs upstream in the main channel translates to outlet runoff and that runoff at the outlet originates locally and in some cases (Figure 14a.) independently of runoff formation in other subbasins of the watershed. Watershed subbasin runoff results from these 4 storms indicate spatial variability is high when examining intrawatershed surface flow.

Spatially varied soil moisture dynamics were also examined for the four events analyzed above (Figures 15-18). Generally, the rain events which produced the highest peak watershed soil moisture were those which also resulted in the highest runoff rates (i.e., 7/20/2011 and 8/9/2011). Soil moisture spatial patterns throughout the watershed were highly variable, accentuating the need to sample soil moisture in various locations when examining hydrologic properties even at a small watershed scale. Transect 3 (located the furthest east) showed a general trend of increasing soil moisture during a wetting event with decreasing elevation. This trend indicates the importance of lateral groundwater flow when examining soil moisture dynamics on a watershed slope. The higher elevation points (SM14 and SM15) showed the lowest soil moisture dynamics of the 5 locations sampled on this transect. Conversely, SM12 (the second lowest elevation point on this transect) had the quickest soil moisture increase and the quickest dry down of any of the locations sampled on this transect.

While transect 3 exhibited an elevation dependent trend for soil moisture dynamics, transect 2 (located the furthest north) and transect 1 (located the furthest south) did not exhibit elevation dependence in their soil moisture profiles. SM7, located on transect 2, showed the fastest increase and decrease in soil moisture on this transect during and following a storm event. In contrast, SM8, ~11m away, only showed high soil moisture temporal variability during the 7/20/2011 storm event. SM10, exhibited the lowest soil moisture changes of any of the locations sampled on transect 2. Interestingly, this location also had the lowest local slope of any sampling location on the transect. On transect 1, SM2 and SM5 showed consistently low soil moisture values when compared to the other 3 sampling locations on the transect and also had the lowest local slope of any sampling locations found on the transect. SM3 and SM4 on transect 1 consistently had the highest soil moisture during storm events of any of the sampling locations. Although elevation and distance from a stream network are generally inversely and directly correlated, respectively, to soil moisture on a given slope (Nash et al., 1991; Anderson and Burt, 1977; Ridolfi et al., 2003), only transect 3 in this study exhibited those trends. Generally, in this environment, distance from the main channel should play less of a role in determining soil moisture since the channel network is ephemeral, unless caliche depth affects soil moisture. Through observations, caliche depth was generally found to increase with distance from the main channel. While relative elevation on the transect slope may play a small role in soil moisture dynamics, it is evident in the case of

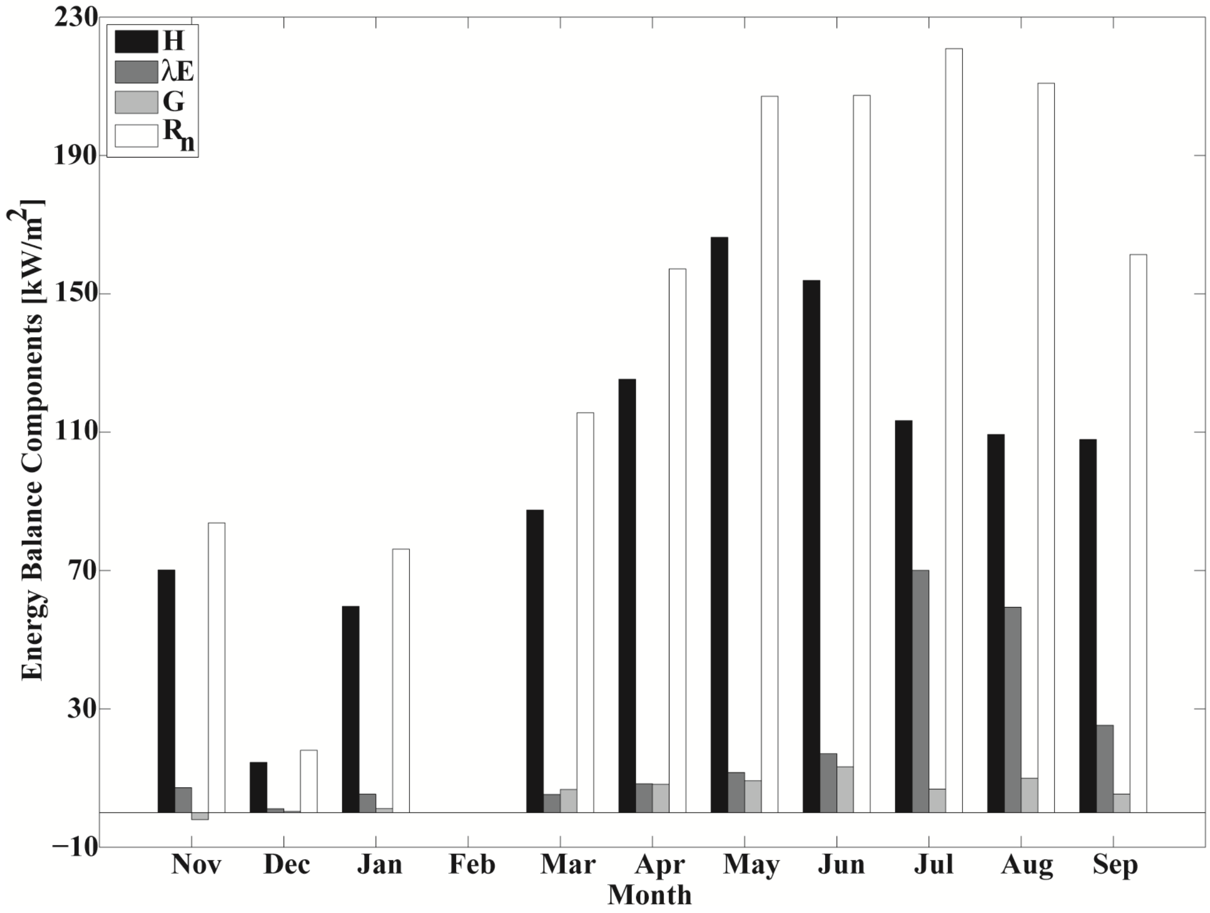

Figure 19: Individual energy balance component contribution as summed at the monthly scale. Sensible heat flux (H), latent heat flux (λE), ground heat flux (G), and net radiation are presented as the percentage of total incoming solar radiation. February data is not shown due to equipment failure.

Table 12: Energy balance component contribution summed at the monthly scale. Sensible heat flux (H), latent heat flux (λE), ground heat flux (G), and net radiation are presented as their monthly summed values [kW/m^2] and as percentages [%] of net radiation. The months of December, January, March, and April have some data missing and February data is not shown due to equipment failure.

Date		Energy Flux [kW/m^2]								% Contribution						
Year	Month	H	λE	G	SW	LW	R_n	IS	ε	H	λE	G	SW	LW	R_n	ε
2010	Nov	70	7	-2	207	-123	84	279	10	84	9	-2	247	-147	100	10
2010	Dec	15	1	0	48	-30	18	65	2	81	6	2	265	-165	100	11
2011	Jan	60	5	1	183	-107	76	246	12	78	7	2	241	-141	100	13
2011	Feb															
2011	Mar	87	5	7	223	-107	116	303	17	76	5	6	193	-93	100	14
2011	Apr	125	8	8	292	-134	157	400	17	80	5	5	186	-86	100	10
2011	May	166	12	9	380	-173	207	527	22	80	6	4	184	-84	100	10
2011	Jun	154	17	13	393	-185	207	535	25	74	8	6	189	-89	100	11
2011	Jul	113	70	7	354	-133	221	477	31	51	32	3	160	-60	100	14
2011	Aug	109	59	10	340	-129	211	447	32	52	28	5	161	-61	100	15
2011	Sept	108	25	5	293	-131	161	392	23	67	16	3	181	-81	100	14
Total		1008	211	59	2712	-1253	1458	3671	191	69	14	4	186	-86	100	12

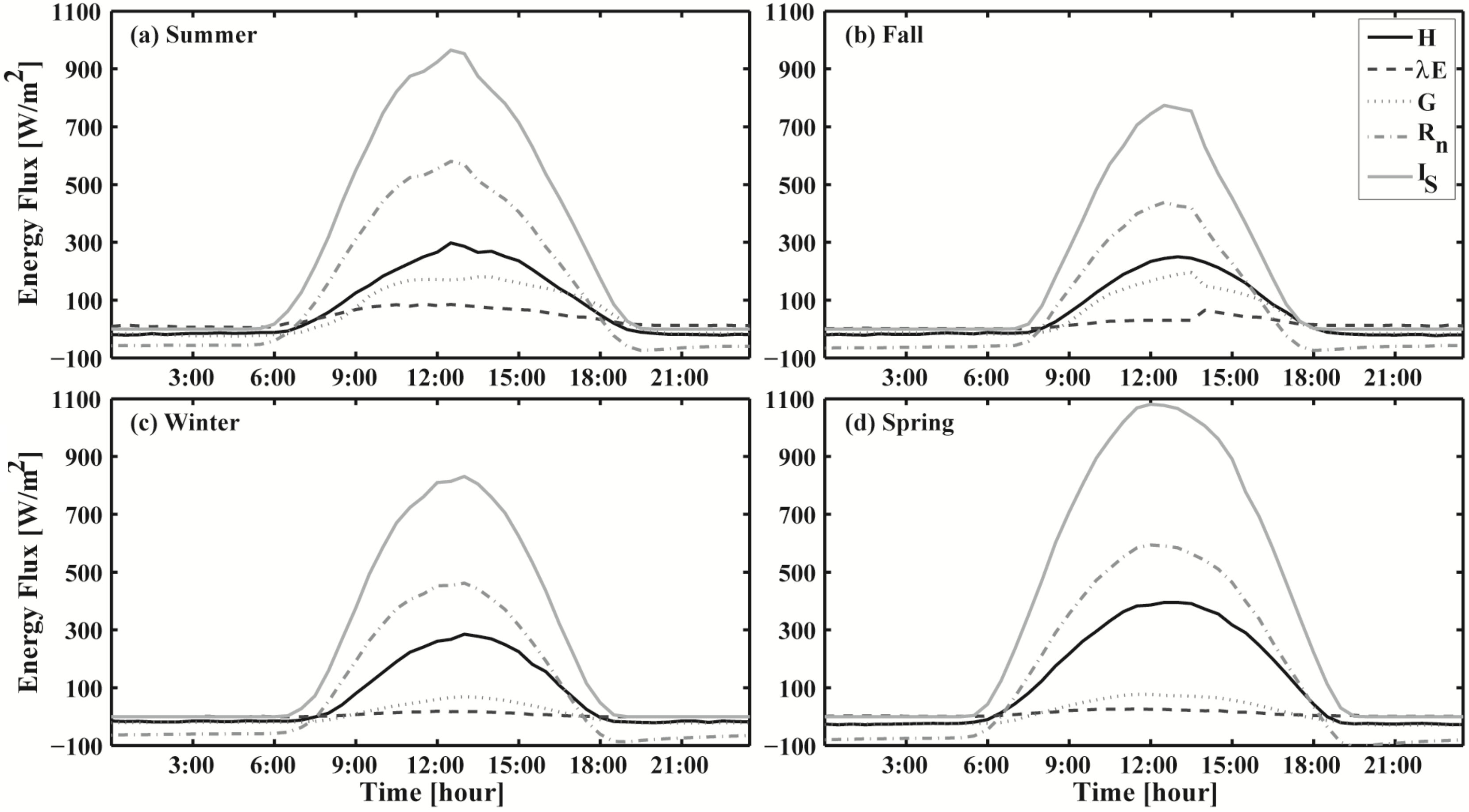

Figure 20: Seasonally averaged diurnal energy fluxes. Summer is calculated from 7/1-9/30, fall is calculated from 10/1-12/31, winter is calculated from 1/1-3/31, and spring is calculated from 4/1-6/30.

transect 1 and transect 2 that local factors such as slope, porosity, caliche depth are likely just as important to greatly affect soil moisture.

3.4 Annual, Seasonal, and Event-scale Energy Dynamics

Semiarid environments by definition are highly limited by water inputs and thus incoming solar radiation exhibits a much higher likelihood of partitioning to sensible heat rather than latent heat. Monthly analysis of the energy balance component contributions confirm the domination of sensible heat flux (H) in this environment with latent heat being seasonally dependent and only playing a strong role in the energy balance in the wet months of July, August, and September (Figure 19). Only the monthly scale, sensible heat flux ranges from 51% to 84% of the net radiation with an annual average of 69%, while latent heat ranges from 5% to 32% of net radiation at the monthly scale and averages 14% annually (Table 12). Ground heat flux consistently has a low contribution to the energy balance at the monthly scale, only exceeding the latent heat contribution during the extremely dry month of March. The seasonal analysis of energy components in Figure 20 shows how these components, on a diurnal scale, can shift in magnitude. Incoming solar radiation (I_S), net radiation (R_n), and sensible heat flux (H) have similar seasonal shifts with maximum seasonal values occurring in the spring, followed by summer, winter, and finally fall. Lower summer values compared to spring and fall having lower values than winter is attributed to increased cloud cover during the NAM season. In contrast, latent heat (λE) is maximized in summer, followed by fall, spring, and finally winter. Latent heat is highly dependent on rainfall pulses since no other major water source is available in this environment, and thus is a major component of the energy balance during the NAM months. Once the ground has dried from the NAM season storms and seasonal storms have ceased in mid to late fall, λE is controlled by

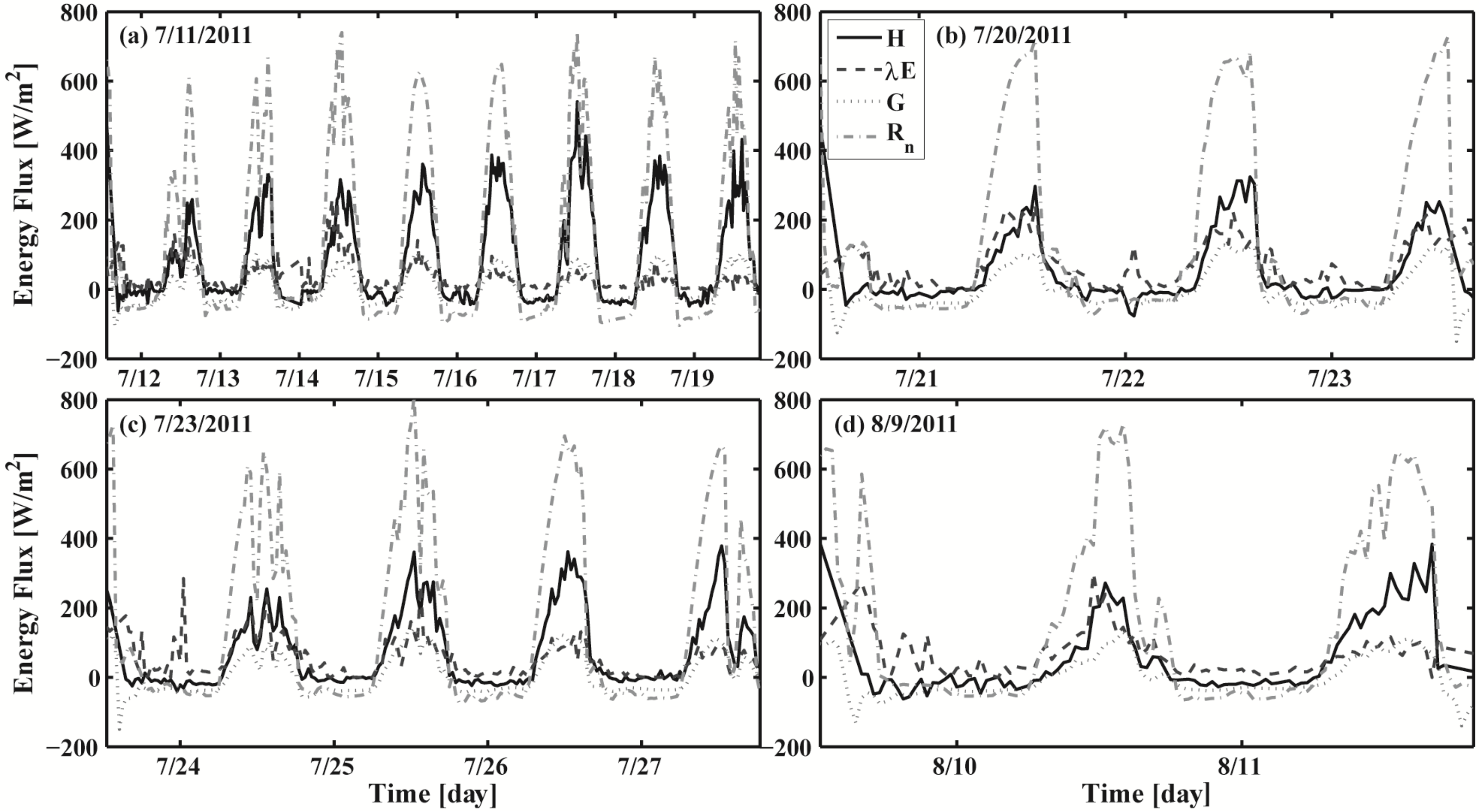

Figure 21: Interstorm fluxes for individual energy balance components. Energy fluxes are shown from 1 hour prior to the onset of the event of interest to 1 hour following the next rainfall event greater than 1 mm of depth.

energy availability which would explain the higher spring latent heat values than those seen during the winter, when energy inputs are at a yearly minimum. Ground heat flux is primarily driven by net radiation; however, vegetation cover and soil moisture are also important factors. Summer greening of vegetation in this region affects the flux of radiation into the ground. When normalizing energy component contributions relative to net radiation (Table 12), this effect is increased due to net radiation being sampled above the vegetation canopy in this study. For this reason, we see that soil heat flux is maximized in the fall, when radiation is still high, soil moisture is elevated, and vegetation cover begins to decrease. This yearly maximum in soil heat flux is followed by the summer season, spring season, and finally the winter season.

Next, energy balance component dynamics were studied following the 4 storm periods outlined earlier. The progression of energy flux dynamics following a rainfall event helps to define the length of impact precipitation pulses can have on energy dynamics within a semiarid region. Figure 21 presents the energy balance progression from each storm period until the next major rainfall event (i.e., >1 mm rainfall). Since net radiation is primarily only going to be affected by cloud coverage on this short of a timescale, we do not see a discernable progression pattern during any of the interstorm periods. In contrast, sensible heat flux is depressed following a rainfall event and can take several days to a week to reach pre-storm levels (Figure 21a.). Excess energy during this dry down period is partitioned into latent heat flux. Daily latent heat fluxes are maximized for the first day following the storm event and slowly decrease over the length of the inter-storm period. Yearly and seasonal soil moisture patterns (Figures 7-11) following a large storm event indicate that it can take upwards of 2 weeks before residual soil moisture levels are reached. These soil moisture storages act to elevate latent heat fluxes for the relatively short inter-storm periods analyzed in Figure 21. Since inter-

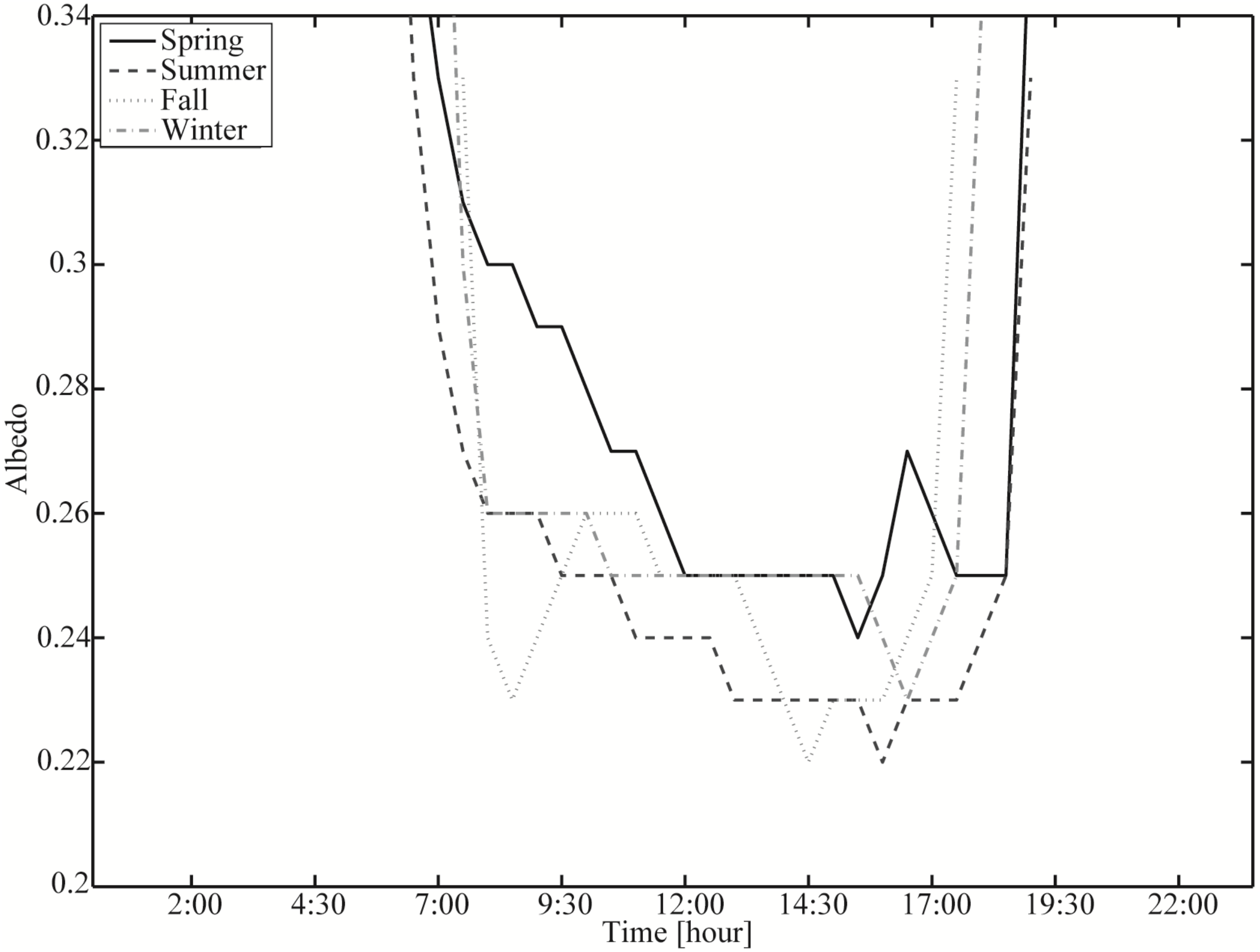

Figure 22: Seasonally averaged surface albedo measured at the tower. Albedo values were calculated from net shortwave radiation and incoming solar radiation.

storm periods generally last less than 2 weeks during the NAM season, soil moisture should be elevated over residual soil moisture for the entire NAM season allowing vegetation to sustain productivity throughout the entire period with minimal stress, leading to elevated transpiration rates during the summer season. If NAM season storm frequency changes in the future, it may be difficult for many desert species to adequately produce during the summer season. While sensible and latent heat fluxes experience a prolonged response to precipitation events, ground heat flux in this region only seems to show a 24 hour response to the precipitation. Following the rainfall event, ground heat flux drops; however, within a 24 hour period, ground heat flux reaches values comparable to those seen prior to the rainfall event. Variable rates at which different energy components return to normalcy following a storm event illustrate the importance of adequate temporal scale environmental sampling in order to understand the system.

Seasonality in surface albedo was found to coincide with seasonality in vegetation greening (Figure 22). Summer represents the lowest albedo season due to increased precipitation leading to higher soil moisture and the onset and progression of vegetation greening. Following the highly productive summer months, albedo increased slightly in the fall. Transitioning for the fall to winter resulted in further increases in albedo due to increased vegetation activity and leaf coverage. This trend continued during a drought period as the system transitioned from winter to spring, with albedo reaching its highest annual values.

3.5 Spatial Variability

Vegetative production in the southwestern semiarid US is driven by the NAM period (Huenneke et al., 2001; Huenneke et al., 2002; Mendez-Barroso et al., 2009; Mendez-Barroso and Vivoni, 2010; Watts et al., 2007). Without sharp increases in

Table 13: Storm event (n=44) precipitation characteristics from June 2010 to July 2011. Rainfall = P and intensity = I are given.

Location	Total P [mm]	Avg Storm P [mm]	Max I [mm/hr]	Mean I [mm/hr]	I Std Dev [mm/hr]
R2	243.7	5.5	19.50	4.91	3.97
R3	228.2	5.2	25.76	5.15	5.13
R4	247.0	5.6	24.38	4.85	4.40

summer precipitation (Figure 3), little vegetative productivity would occur. However, precipitation pulses during the NAM season are well known for their spatial variability (Vivoni et al., 2007b; Gochis et al., 2004) which can lead to small scale heterogeneities in intra-watershed hydrologic responses. Spatial variation of precipitation is presented for the 3 transect location rain gauges. Measurements from the outlet and the tower were excluded due to equipment failure during portions of the year resulting in missing datasets. Average depth of rainfall per storm event and total rainfall measured over the sampling period only varies approximately 8% between the 3 locations. Similarly, average storm intensity only varies ~6%. Although NAM summer storms are known for their high degree of localization, the spatial scale examined in this study was small enough to not experience large variability in rainfall. The greatest distance between 2 transect tipping bucket rain gauges was 188 m between R2 and R4.

Large event (i.e., > 1 mm total precipitation) averaged soil moisture for the entire sampling period (n=18) was performed for each sampling location for 5 cm depth (Figure 23) and averaged over the vertical depth profile sampled (Figure 24). The soil moisture for each location was averaged for all events from 30 min prior to storm onset to 24 hours after storm completion. These maps indicate a high degree of soil moisture variability not only within the watershed, but also within each transect. Results from this analysis are similar to those seen for the 4 storm events analyzed previously (Figures 15-18).

Table 14: Seasonal and yearly depth averaged soil temperature for each transect. Calculations were based on daily maximum soil temperatures.

Season	T1 Average	T1 St Dev	T2 Average	T2 St Dev	T3 Average	T3 St Dev
Summer	35.79	1.28	36.87	1.54	36.42	0.87
Fall	18.40	1.18	21.10	1.20	19.52	1.18
Winter	14.74	3.00	17.89	1.31	18.56	3.04
Spring	33.63	1.85	34.55	1.95	34.44	1.33
Yearly	25.64	9.81	27.60	8.68	27.24	8.69

Transects 2 and 3 show a mild elevation dependence for 5 cm soil moisture and a strong elevation dependence for soil moisture averaged over the depth profile. It should be noted that SM6 (located on transect 2) is the only location in the watershed where the depth averaged soil moisture where 30 cm depth was not sampled due to a shallow calcium carbonate horizon in this location. Transect 1 presents a unique case in which intermediate elevation locations have the highest soil moisture values for 5cm and depth averaged soil moisture plots. SM1 and SM5 locations have the lowest averaged soil moisture values within the watershed indicating local conditions are more important for soil moisture dynamics in these two locations when compared to other locations. Due to watershed hillslope aspect, soil temperature was found to vary between transects (Table 14). For all seasons except winter, transect 2 had the highest soil temperature of the 3 transects sampled. Conversely, transect 1 had the lowest transect averaged soil temperature of the three transects sampled. These trends are attributable to the aspect of each slope on which each transect is located. Transect 1 is located on the north facing slope which represents the slope facing away from the sun year round, while transect 2 is located on the south facing slope which always faces the sun year round, maximizing

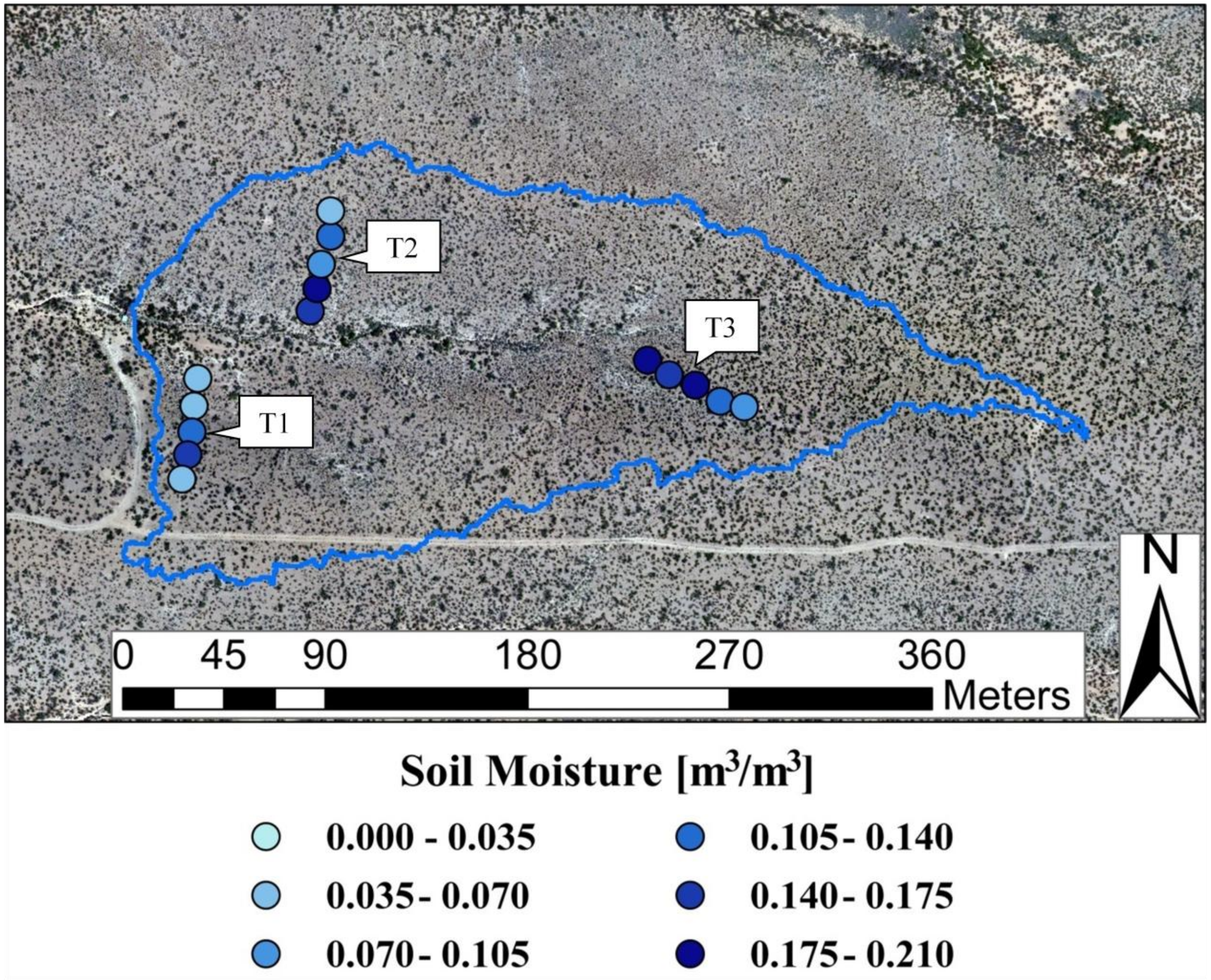

Figure 23: A spatial distribution map of shallow soil moisture (5 cm) averaged over all storm periods > 1 mm of total rainfall from 6/1/2010 to 9/30/2011. Relative locations of transect 1 (T1), transect 2 (T2), and transect 3 (T3) are shown.

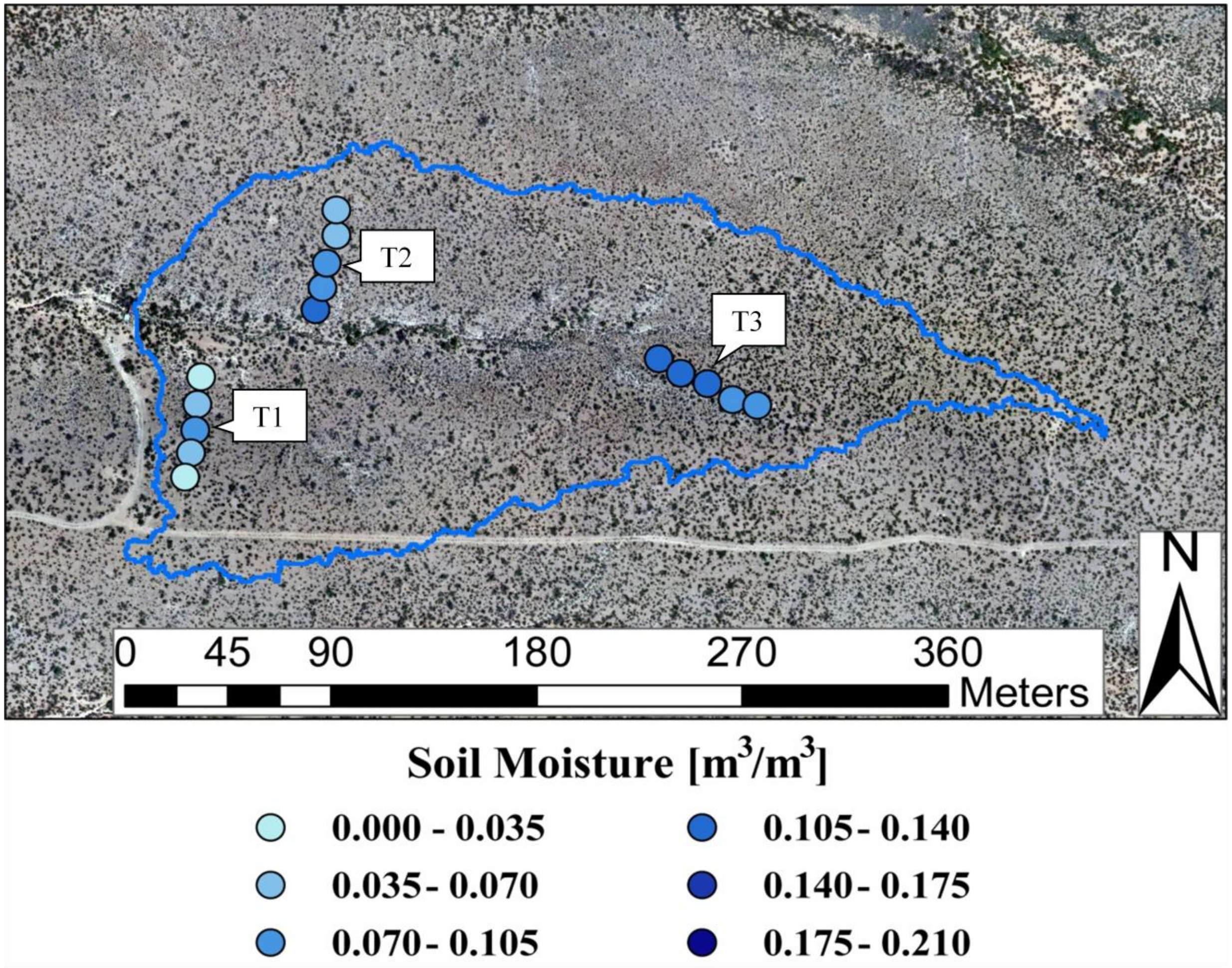

Figure 24: A spatial distribution map of 30 cm soil moisture averaged over all storm periods > 1 mm of total rainfall from 6/1/2010 to 9/30/2011. Relative locations of transect 1 (T1), transect 2 (T2), and transect 3 (T3) are shown.

incoming radiation. Soil temperature is important for soil moisture dynamics, as increasing soil temperature leads to increased soil evaporation.

Soil moisture dry down analysis was performed for the 7/11/2011, 7/20/2011, 7/23/2011, and 8/9/2011 post-storm periods (Figure 25). Following each storm period, trends were determined for transect averaged soil moisture at 5 cm depth and averaged over the 30 cm vertical profile. Following all four storms, 5 cm transect averaged soil moisture was lowest for transect 1 and highest for transect 3. Solar radiation may be a good predictor of dry down rates as T2 and T3 (highest solar radiation due to slope aspect) consistently dry down at a faster rate than T1 (lowest solar radiation due to north facing slope aspect). T2 and T3 dry down at generally the same rate except for the 7/11/2011 storm, for which T2 dries down faster. Another explanation for the slow 5 cm soil moisture dry down for T1 relative to T2 and T3 may be due to T1 soil moisture consistently being lower than T2 or T3. Soils dry at a slower rate as soil moisture reserves are depleted due to plant physiological characteristics and soil properties (Laio et al., 2001). When analyzing the profile averaged soil moisture across the 3 transects following each storm we see results that are similar to the 5cm averaged data, T3 is the wettest transect and T1 is the driest. Soil moisture does not decrease noticeably following any of the storm events for the profile averaged values indicating transect averaged net lateral flow is minimal. Variability in 5 cm soil moisture and stability in profile averaged soil moisture shows that while shallow soil moisture decreases deeper soil moisture increases which would indicate that the shallow soil moisture is redistributed to deeper vertical depths. However, post-storm spikes in latent heat (Figure 7), and thus evapotranspiration, prove that vegetative activity and soil evapotranspiration can cause large depletions in soil moisture in a relatively quick post-storm period, reaching pre-storm soil moisture levels in as quickly as a week. Therefore, it is likely that in conjunction with 5cm soil moisture replenishing deeper soil moisture, a good proportion of the 5cm soil moisture is lost to ET, and thus profile averaged soil moisture is likely kept steady by a net

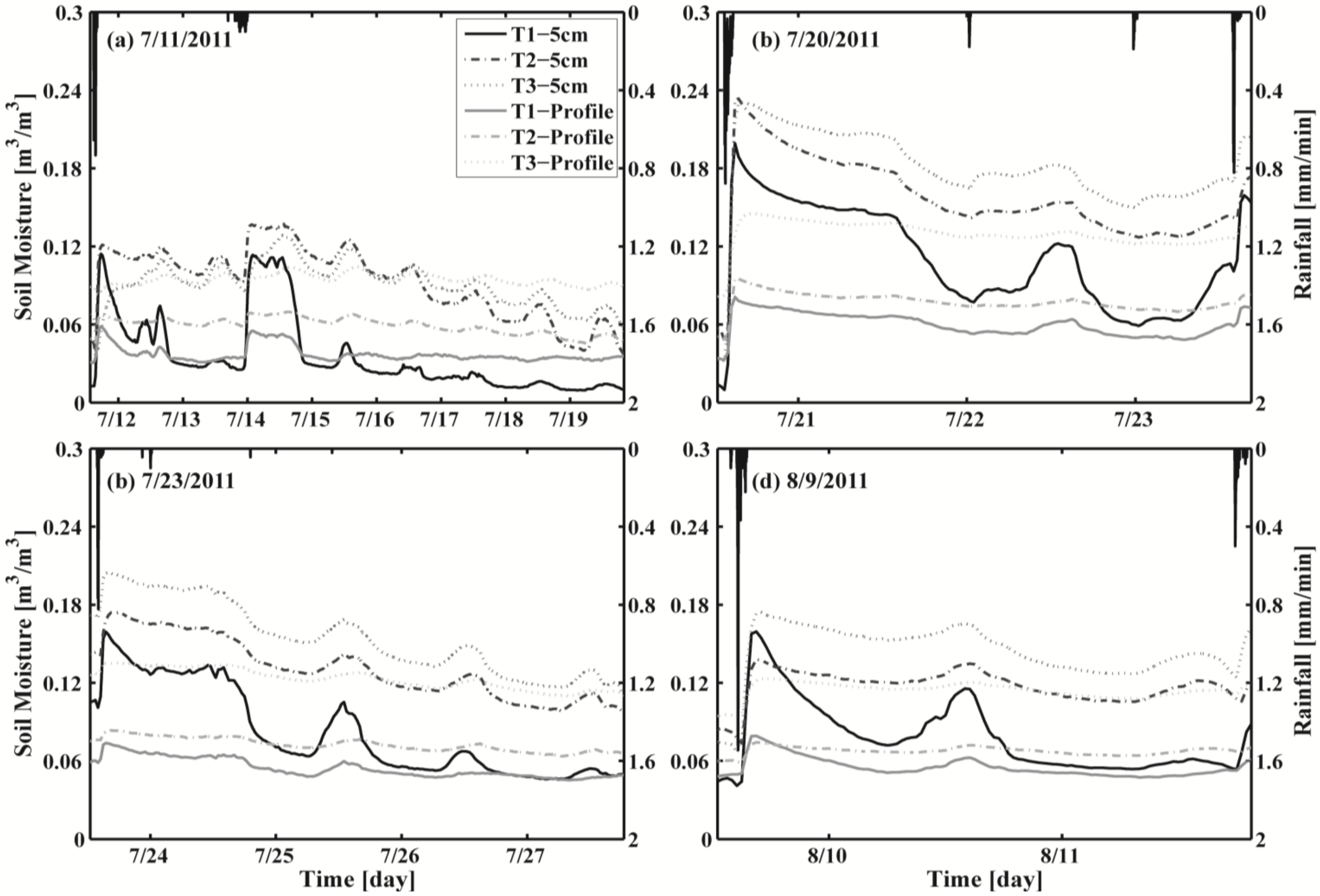

Figure 25: Spatial variation of transect averaged 5 cm soil moisture and profile averaged soil moisture within the watershed following 4 storm events.

influx of soil water from the higher elevation portion of each slope and/or a lower depth soil moisture stability from caliche release of stored water.

3.6 Evapotranspiration vs. Soil Moisture Relationship

Laio et al. (2001) described a stochastic model for the determination of soil leakage and evapotranspiration which was based on soil characteristics and plant physiology. The model (Figure 26) was based on 5 soil and vegetation characteristics: 1) maximum evapotranspiration (ET_{MAX}), 2) evapotranspiration at the wilting point (ET_W), 3) soil moisture at the soil's hygroscopic point (θ_h), 4) soil moisture at the wilting point (θ_w), and 5) soil moisture at which evapotranspiration is maximized (θ^*). The relationship outlined by Laio is also currently the basis of calculating actual evapotranspiration for many currently employed hydrometeorological and climate models currently in use today (e.g., TIN-based Realtime Integrated Basin Simulator - tRIBS, Variable Infiltration Capacity Macroscopic Hydrologic Model - VIC, the Automated Geospatial Watershed Assessment Tool - AGWA, etc).

Through the use of a numerical method developed by Vivoni et al. (2008) these 5

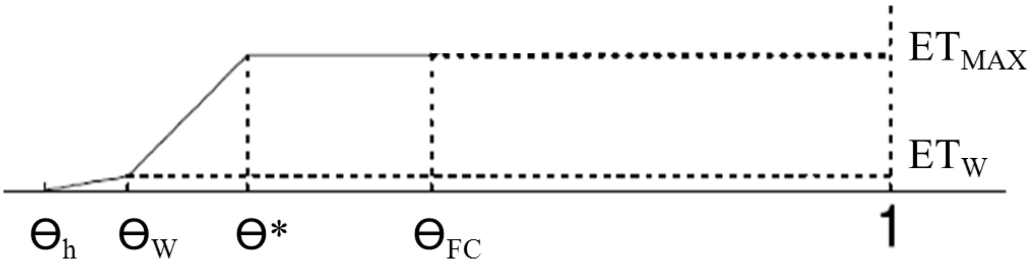

Figure 26: Conceptual model of a piecewise evapotranspiration vs. soil moisture relationship where ET estimates are calculated based on the values of θ_h, θ_W, θ^*, ET_{MAX}, and ET_W.

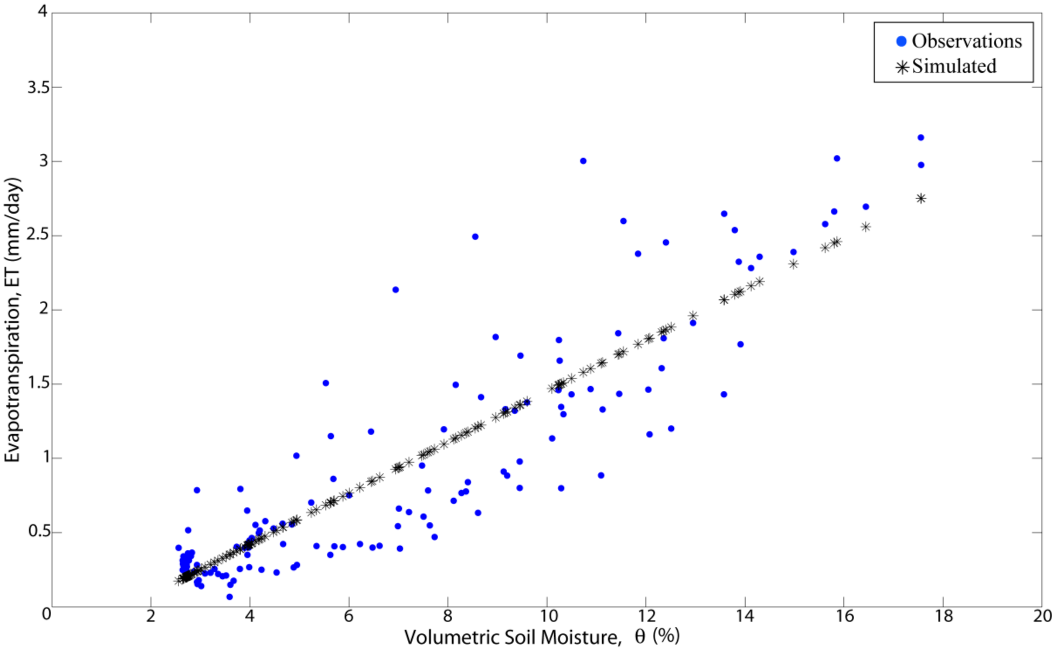

Figure 27: Piecewise linear relationship based on the point-scale θ dataset (ET_{Tower}) and ET_{EC} sampled values, created using the multivariate approach established by Vivoni et al. (2008). Field observed values (blue) and simulated relationship values (black) are given.

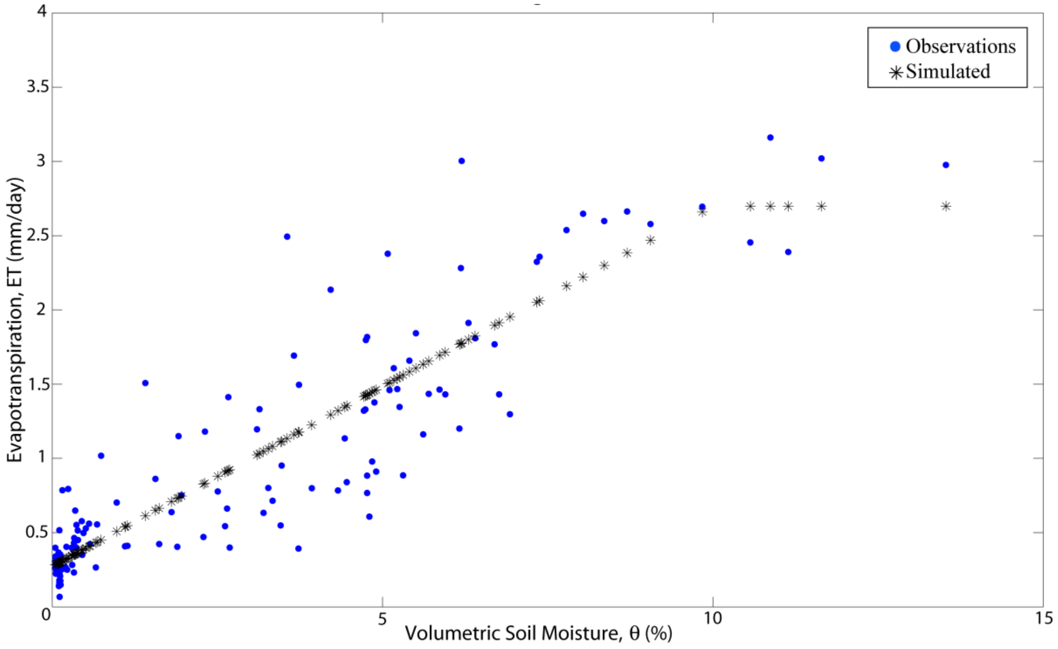

Figure 28: Piecewise linear relationship based on the distributed θ dataset (ET_{Basin}) and ET_{EC} sampled values, created using the multivariate approach established by Vivoni et al. (2008). Field observed values (blue) and simulated relationship values (black) are given.

characteristics were calculated using a multivariate approach by establishing a best-fit piecewise relationship between eddy covariance tower measured evapotranspiration and 1) basin averaged soil moisture and 2) point-scale soil moisture at the tower. Developing these 2 relationships allowed for the evaluation of the importance of spatial sampling of soil moisture when performing this analysis. When analyzing the results, it was found that a piecewise relationship between basin averaged soil moisture and evapotranspiration (Figure 28) occurred while the point-scale tower soil moisture versus evapotranspiration relationship (Figure 27) more closely mimicked at single linear relationship. The establishment of an evapotranspiration maximum plateau (ET_{MAX}) at 10% soil moisture (θ^*) for the basin-averaged soil moisture relationship is important in creating a hydrometeorological model which can accurately predict ET at high θ values. When analyzing the tower's point-scale results (Table 15) for this analysis, we see that $\theta^* = \theta_{MAX}$ (i.e., a maximum evapotranspiration rate is never found for the relationship using the soil moisture value range from the point-scale dataset. The inability of the point-scale soil moisture dataset to produce an ET_{MAX} when utilizing the same eddy covariance ET

Table 15: Soil and Vegetation Characteristics calculated from the eddy covariance method calculated ET using basin-averaged or tower-sampled soil moisture.

	ET_{Basin}	ET_{Tower}
ET_{MAX} [mm/day]	2.70	2.75
ET_{W} [mm/day]	0.283	0.174
θ_h [%]	0.005	0.012
θ_W [%]	0.045	2.551
θ^* [%]	10.0	17.6
θ_{MAX} [%]	13.5	17.6

measurements as the basin-averaged soil moisture dataset could prove problematic when calibrating a hydrologic model. The point-scale based relationship would result in indefinite increases to ET with increasing soil moisture, or the need to estimate θ* based on non-empirical means.

The accuracy of the created relationships was tested against the field measured ET_{EC} values in order to determine the importance of using a distributed dataset for ET estimation. Mean absolute error (MAE) between eddy covariance measured ET and ET estimates using the two established ET vs. θ relationships were calculated daily over the sampling period. When these values were averaged over the sampling period, the point-scale based ET vs. θ relationship exhibited a MAE value of 0.252, whereas the basin-averaged based ET vs. θ relationship exhibited a MAE value of 0.235. We can see that similar to the results of the ET estimation utilizing the water balance method presented earlier, when we create an ET vs. θ relationship using distributed data instead of point-scale data we increase the accuracy at which we can estimate evapotranspiration.

3.7 Point-scale Modeling Results

Point-scale simulations of hydrological and meteorological processes at the eddy covariance tower were performed for the 2011 period from 3/11 to 10/1 in order to calibrate the model. This period included a dry spring season and a wet summer season in order to test the model accuracy through the extreme seasonal transitions which occur at this site. 2011 modeled results showed good agreement with field observed data during the simulated period for most of the processes modeled (Figure 29). Simulated net radiation values show excellent agreement with field observations during the dry spring season. While summer rains reduce the accuracy of net radiation simulations, through most of the wet NAM season the simulations show good agreement with field

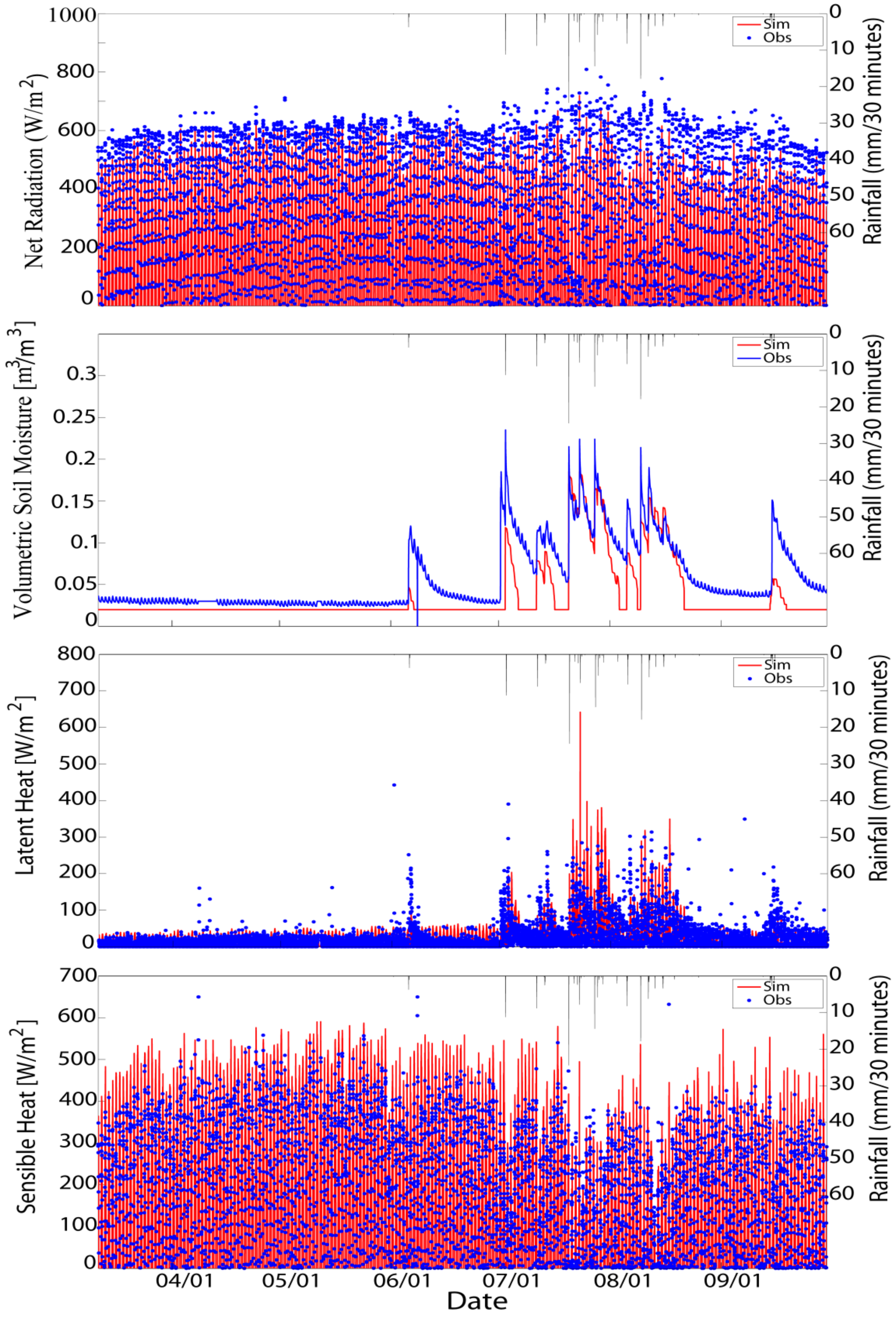

Figure 29: A comparison of 2011 tRIBS model calibration simulation results (red) to field observed data (blue) for net radiation, 5 cm depth soil moisture, latent heat flux, and sensible heat flux.

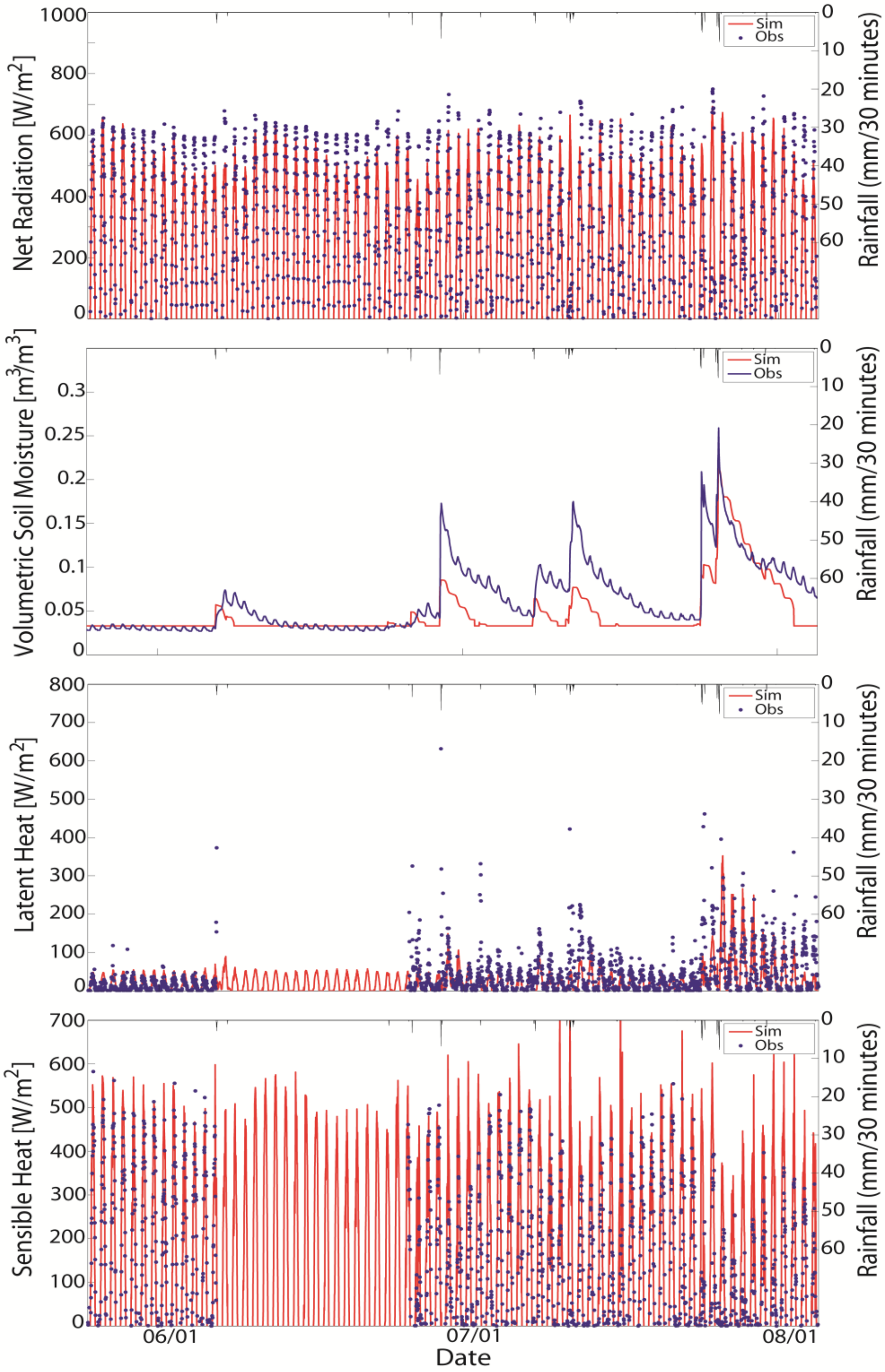

Figure 30: A comparison of 2010 tRIBS model simulation results (red) to field observed data (blue) for net radiation, 5 cm depth soil moisture, latent heat flux, and sensible heat flux.

observations. Simulated 5 cm soil moisture during the mid-NAM season also shows excellent agreement with field sampled values where peaks and drydown dynamics are captured well, while early and late NAM season agreement between observed and simulated results exhibit a need for increased calibration efforts in order to fully capture the seasonal dynamics. The soil moisture results show the degree to which vegetation dynamics can control the processes within the system. I am able to capture the soil moisture dynamics when transpiration is maximized in the mid NAM season, but have less accuracy in capturing early and late NAM season soil moisture dynamics due to the changing strength of transpirational effects on the system. 4 statistical metrics were used to compare observed to simulated processes (Table 16). Examining the statistical results show that R_n, T_S, H, and θ have excellent accuracy for the 2011 simulated spring and summer period. In contrast, G shows fairly poor agreement between simulated and observed results due to manner in which the model calculates G. In the model G is calculated as a residual from the energy balance. Earlier we showed that there was always error when attempting to close the energy balance using field measurements (Table 12). The inability of complete energy balance closure is a common phenomenon when using eddy covariance field sampling techniques (Dugas et al., 1991; Nie et al., 1992; Fritschen et al., 1997; Mahrt, 1998; Twine, et al., 2000) and is usually attributed to G. The closure issue certainly has an effect on the accuracy of G when compared field observed values and simulated values.

Following calibration of tRIBS using the 2011 dataset, the model was run for a shorter period during the 2010 transition between spring and summer (5/24/2010 – 8/5/2010). This run was to confirm the model's ability to reproduce the simulated process accuracy which was seen during the 2011 calibration period (Figure 30). Again

Table 16: Statistical comparisons between field observations and simulated energetic and hydrologic processes.

2011 Statistics						
	R_n	T_S	θ	λE	G	H
CC	0.96	0.95	0.83	0.66	0.44	0.95
E	0.90	0.89	-0.08	0.31	-0.16	0.77
B	0.78	1.05	0.56	1.12	0.03	0.90
MAE	51.5	3.31	0.03	14.8	32.5	57.2
2010 Statistics						
	R_n	T_S	θ	λE	G	H
CC	0.87	0.76	0.85	0.58	0.08	0.76
E	0.76	0.43	0.20	0.29	-2.02	0.25
B	1.01	1.05	0.67	0.76	0.41	1.22
MAE	78.4	7.16	0.02	22.1	44.3	93.8

we saw good model simulation agreement with field observations for R_n, T_S, θ, and H. No correlation between simulated and field observed G was found, once again showing that energy balance closure is causing a problem with accurate G simulation (Table 16).

Overall, using tRIBS to simulate hydrologic and energetic processes at the point-scale provides a means to accurately estimate land and atmosphere interactions at high temporal resolution. The periods for which I calibrated the model and ran a test simulation represent the most dynamic seasonal shift during the year, where the dry spring period transitions to the wet NAM summer.

4. CONCLUSIONS AND FUTURE WORK

Field observation resolution has long been the limiting factor in the characterization of land-surface and atmospheric interactions for a variety of different environments. As forecasting models become more complex, downscaling of model outputs to field-relevant resolutions has become necessary and universally accepted (Boe et al., 2006; Piles et al., 2011; Sultana and Coulibaly, 2011). Few studies have focused on determining the spatial and temporal resolution at which hydrologic processes change in order to define the scale at which these processes should be analyzed for adequate system characterization. In this study we presented an intensive analysis of hydrologic and atmospheric processes for a small semiarid watershed in the Chihuahuan desert which exhibited strong NAM derived seasonality, as is characteristic of the region. Understanding the seasonality of these systems has garnered increased research efforts in the past few decades (Mendez-Barroso and Vivoni, 2010; Notaro et al., 2010; Leung et al., 2003); however, these systems are still recognized for their high degree of inter-annual and intra-seasonal variation in rainfall patterns, which to this point is still poorly understood (Englehart and Douglas, 2010). It is not only important to define the NAM system by its macroscale processes to understand how these lead to self-perpetuation, but to also understand process interactions at a smaller scale to determine the uniformity of these process responses. Furthermore, a clear understanding of the heterogeneities inherit in the system leads to better response predictions and forecasting at larger scales.

In this thesis, the spatiotemporal variability of watershed hydrologic and energy flux responses to NAM system seasonality and rainfall event progression are analyzed from June 2010 to September 2011 through environmental sampling of atmospheric and surface processes at high resolution. The use of a dense sensing network which monitored atmospheric fluxes, surface runoff, soil moisture, and precipitation allowed for characterization of water and energy balance dynamics useful for the evaluating the application and accuracy of distributed hydrologic modeling and forecasting. From the effort of this work the following characteristics were identified for the Tromble watershed:

a) Seasonal shifts in land surface albedo towards decreased values during the NAM season are attributable to increased vegetation productivity and greening in response to drastic increases in available energy and rainfall. Increases in energy and rainfall resulted in elevated soil moisture at 5 cm, 15 cm, and 30 cm depths; increased latent heat; and increased runoff production (with only 2 of 18 runoff events not occurring during the NAM season). Carbon fluxes were also greatly altered by seasonal increases in rainfall with large carbon releases immediately following rain events and large carbon uptake once vegetation responses to increased soil moisture occurred.

b) Monthly water and energy balances indicate the system is highly responsive to increased rainfall by increasing evapotranspiration or latent heat fluxes. Extreme elevations in monthly precipitation, such as the month of July 2011 represents the only significant increases in soil water storage and if increased precipitation rates are not sustained in subsequent months (August and September 2011), soil water storage will quickly diminish due to increased net radiation and evapotranspiration.

c) Temporal scale discontinuities exist between energy fluxes and soil moisture dynamics following storms. Latent and sensible heat fluxes decrease and increase in magnitude, respectively, to close to prestorm values within a few days, while shallow soil moisture can take up to 2 weeks and 30 cm depth averaged soil moisture can take longer. This indicates that vegetation responses are slower than expected and could result in adequate time for deep soil moisture replenishment if ample rainfall occurs within a reasonable time-frame.

d) Variability in soil moisture occurs between hillslopes and within individual hillslopes. Previous studies analyzing hillslope soil moisture indicate an inverse relationship between soil moisture and elevation (Anderson and Burt, 1977) and while this was the general case for 2 of the 3 hillslopes examined in this study (T2 and T3), the north-facing hillslope (T1) showed high variability in soil moisture with elevation indicating that for hillslopes with low relief from crest to bottom, local topographic and soil characteristics can be more important than elevation in soil moisture infiltration and dry down. This variability in soil moisture was likely very important in establishing the high intra-watershed variability in surface flow.

e) Hillslope aspect plays an important role in overall soil moisture dry down rates following a storm due to the relative amount of solar radiation the hillslope receives. However, infiltration rates can vary between hillslopes even within a watershed as small as the Tromble watershed, which was evidenced by the consistent hillslope relative soil moisture hierarchy seen following storms (T3 was consistently the most wet and T1 was consistently the most dry).

f) ET estimation using the water balance provides a more economical means of obtaining ET at the monthly scale than using the costly Bowen or eddy covariance methods. While using point-scale measurements to calculate an ET residual from the water balance can provide adequate accuracy, I found using spatially averaged datasets drastically increases estimation accuracy. Using eddy covariance derived field samples of ET as a standard, I found spatially averaged soil moisture and precipitation resulted in a 74% increase in accuracy when compared to point-scale measurements. This analysis expanded on the results of Scott (2010) by observing the validity of using a spatially varied sampling dataset rather than point-scale measurements of P and θ for performing this calculation, resulting in almost a doubling of ET estimation accuracy for our watershed.

g) Spatial scale matching is also important for the determination of a field derived evapotranspiration vs. soil moisture relationship. Since most hydrologic models which partition evapotranspiration into evaporation and transpiration use the piecewise ET vs. soil moisture relationship described by Laio et al. (2001), adequate estimation of the soil hygroscopic point, the wilting point, and the soil moisture point at which maximum evapotranspiration occurs is imperative for adequately modeling the system. This thesis took a step closer to closing the spatial scale mismatch between the tower sampling footprint and the soil moisture sampling area by spatially averaging the soil moisture sampling footprint. Similar to the results found estimating ET using the water balance, when I increased field sampling resolution from the point-scale to the distributed-scale, I found ET estimation accuracy increased using the derived ET vs. θ relationship.

The observations and analyses conducted in this study show the hydrologic variability associated with a small semiarid watershed located in the NAM region of North America. While field observations are still a major limiting factor for watershed characterization and the forecasting of watershed responses to varying environmental factors, this study presents high spatial and temporal resolution characterizations of a highly variable ecosystem and provides evidence of the importance of understanding fine scale processes in determining the response of a system. Improvement of the distributed hydrological modeling results by finer scale field observations was evidenced by Minet et al. (2011), who found that spatially varying antecedent soil moisture to match field measured values resulted in improvement of runoff predictions when modeling at the hillslope scale. The high resolution characterization provided in this thesis will not only improve model forecasting performance for runoff, but will also improve understanding of other atmospheric and surface feedbacks and processes. However, some of the analyses performed in this thesis are still limited by spatial scale mismatches. Furthermore, reproducibility of the results found in this study is needed in order to extrapolate results to other small watersheds within the NAM region of the semiarid southwestern US.

Future work to further ameliorate spatial scale mismatches between flux tower footprints and surface scale processes would greatly increase understanding of surface/atmosphere interactions. Eddy covariance tower measurements of atmospheric energy fluxes sample a constantly shifting footprint due to the natural variability associated with wind movement (Baldocchi, 1997; Horst and Weil, 1992). Screening data to only include periods when the footprint includes the surface sampling area is one possibility for accomplishing this analysis; however, this depends on wind direction and speed being truly random. In most cases changes in wind speed and direction follow a general general pattern which is the case in the Jornada. In order to take a truly characteristic sample, it would be best to create a surface sampling network which covers an area representative of the tower sampled region as determined through field measurement.

While this study will increase ecosystem understanding and hydrologic modeling performance in semiarid systems, it represents only one localized characterization. Future watershed characterizations of a similar spatiotemporal resolution within small southwestern US semiarid watersheds would confirm or deny the reproducibility of the observations and analyses performed here. This thesis represents the first step in the creation of a regionally based hydrologic model focusing on accurate small watershed response to NAM storms in the semiarid US. It is therefore imperative to insure similar response trends can be seen in small watersheds not only in the Chihuahuan desert, but also within the Sonoran and Mojave deserts.

Finally, performing detailed sensitivity analyses with varying spatial and temporal scales of data collected from this experiment for the calibration of the tRIBS model will provide feedback on how to best optimize future deployments of environmental monitoring networks. As we have seen responses to seasonal, monthly, and event-scale processes differ in spatial extent and temporal range for separate land-atmosphere processes. By varying the resolution of input parameters into the model during the calibration stage, one could determine the resolution of data needed for a given application. This information is imperative for the economical design of future field experiments aimed to supply input or validation data for hydrologic modeling.

5. REFERENCES

Abrahams, A.D.; Parsons, A.J.; Wainwright, J. 2003. Disposition of rainwater under creosotebush. *Hydrological Processes* 17: 2555–2566.

Acutis, M.; Donatelli, M. 2001. *SOIL*PAR2.00: software to estimate soil hydrological parameters and functions. Proc. 2nd Int. Symp. Modelling Cropping Systems, 16-18 July, Florence, Italy, 209-210.

Acutis, M.; Donatelli, M. 2003. *SOIL*PAR 2.00: software to estimate soil hydrological parameters and functions. *Eur. J. Agron*. 18: 373-377.

Adams, D.K., Comrie, A.C. 1997. The North American Monsoon. *Bull. Amer. Meteor. Soc.* 78: 2197–2213.

Alcaraz, S.A.; Sannier, C.; Vitorino, A.C.T. and Daniel, O. Comparison of methodologies for automatic generation of limits and drainage networks for hydrographic basins. *Rev. bras. eng. agríc. ambient*. 2009, vol.13, n.4, pp. 369-375. ISSN 1807-1929.

Anderson, M.G.; Burt, T.P. 1977. Automatic Monitoring of Soil Moisture Conditions in a Hillslope Spur and Hollow. *Journal of Hydrology*. 33: 27-36.

Austin AT, Yahdjian L, Stark JM, Belnap J, Porporato A, Norton U, Ravetta D, Schaeffer SM (2004) Water pulses and biogeochemical cycles in arid and semiarid ecosystems. *Oecologia* 141(2): 221-235.

Baldocchi, D.D. 1997. Flux footprints within and over forest canopies. *Boundary-Layer Meteorol.* 85: 273–292.

Beals, E.A. 1922. The semipermanent Arizona low. *Monthly Weather Review* 50: 341-347.

Ben-Hur, M.; Marcos, L. 2008. Effect of soil weeting conditions on seal formation, runoff, and soil loss in arid and semiarid soils – a review. *Australian Journal of Soil Research* 46(3): 191-202.

Beuchat, X.; Schaefli, B.; Soutter, M.; Mermoud, A. 2011. Toward a robust method for subdaily rainfall downscaling from daily data. *Water Resources Research* 47: W09524, doi: 10.1029/2010WR010342.

Boe, J.; Terray, L.; Habets, F.; Martin, E. 2006. A simple statistical-dynamical downscaling scheme based on weather types and conditional resampling. *Journal of Geophysical Research-Atmospheres* 111: DOI: 10.1029/2005JD006889.

Burba, G.G., and D.J. Anderson, 2010. A Brief Practical Guide to Eddy Covariance Flux Measurements: Principles and Workflow Examples for Scientific and Industrial Applications. LI-COR Biosciences, Lincoln, USA, 211 pp.

Bestelmeyer, B. T., D. A. Trujillo, A. J. Tugel, and K. M. Havstad. 2006. A multi-scale classification of vegetation dynamics in arid lands: What is the right scale for models, monitoring, and restoration? *Journal of Arid Environments* 65: 296-318.

Breshears, D.D.; Nyhan, J.W.; Heil, C.E.; Wilcox, B.P. 1998. Effects of woody plants on microclimate in a semiarid woodland: Soil temperature and evaporation in canopy and intercanopy patches. *International Journal of Plant Sciences* 159: 1010–1017.

Campbell, J.E. 1990. Dielectric properties and influence of conductivity in soils at one to fifty Megahertz. *Soil Sci. Soc. Am. J.* 54: 332-341.

Cavanaugh, M.L.; Kurc, S.A.; Scott, R.L. 2011. Evapotranspiration partitioning in semiarid shrubland ecosystems: a two-site evaluation of soil moisture control on transpiration. *Ecohydrology* 4(5): 671-681.

Cerezo-Mota, R.; Allen, M.; Jones, R. 2011. Mechanisms Controlling Precipitation in the Northern Portion of the North American Monsoon. *Journal of Climate* 24(11): 2771-2783.

Definiens, 2009. *eCognition Developer 8.0 User Guide*. Munich: Definiens AG.

Dominguez, F., P. Kumar, and E. R. Vivoni (2008), Precipitation recycling variability and ecoclimatological stability—A study using NARR data. Part II: North American monsoon region. *J. Clim*. 21(20): 5187– 5203.

Dugas, W.A.; Fritschen, L.J.; Gay, L.W.; Held, A.A.; Matthias, A.D.; Reicosky, D.C.; Steduto, P.; Steiner, J.L. 1991. Bowen ratio, eddy correlation, and portable chamber measurements of sensible and latent heat flux over irrigated spring wheat. *Agric. For. Meteorol.* 56: 1–20.

Duniway, M.C.; Snyder, K.A.; Herrick, J.E. 2010. Spatial and temporal patterns of water availability in a grass-shrub ecotone and implications for grassland recovery in arid environments. *Ecohydrology* 3: 55-67.

Englehart, P.J.; Douglas, A.V. 2010. Diagnosing warm-season rainfall variability in Mexico: A classification tree approach. *International Journal of Climatology* 30(5): DOI: 10.1002/joc.1934.

Erdas, 2010. *Erdas 2010 Field Guide*, Norcross, GA: Erdas, Inc.

Forzieri, G.; Castelli, F.; Vivoni, E.R. 2011. Vegetation Dynamics within the North American Monsoon Region. *Journal of Climate* 24(6): 1763-1783.

Fredrickson, E. L., R. E. Estell, A. S. Laliberte, and D. M. Anderson. 2006. Mesquite recruitment in the Chihuahuan Desert - historic and prehistoric patterns with long-term impacts. *Journal of Arid Environments* 65, no. 2: 285-95.

Fritschen, L.J.; Qian, P.; Kanemasu, E.T.; Nie, D.; Smith, E.A.; Stewart, J.B.; Verma, S.B.; Wesely, M.L. 1992. Comparisons of surface flux measurement systems used in FIFE 1989. *J. Geophys. Res*. 97 (D17): 18697–18713.

Gebremichael, M.; Vivoni, E.R.; Watts, C.J.; Rodríguez, J.C. 2007. Submesoscale Spatiotemporal Variability of North American Monsoon Rainfall over Complex Terrain. *J. Climate* 20: 1751–1773.

Gochis, D.J.; Jimenez, A.; Watts, C.J.; Garatuza-Payan, J.; Shuttleworth, W.J. 2004. Analysis of 2002 and 2003 Warm-Season Precipitation from the North American Monsoon Experiment Event Rain Gauge Network. *Monthly Weather Review* 132: 2938-2953.

Gochis, D.J.; Brito-Castillo, L.; Shuttleworth, W.J. 2006. Hydroclimatology of the North American monsoon region in northwest Mexico. *Journal of Hydrology* 316(1–4): 53– 70.

Gochis, D.J.; Watts, C.J.; Garatuza-Payan, J.; Cesar-Rodriguez, J.C. 2007. Spatial and Temporal Patterns of Precipitation Intensity as Observed by the NAME Event Rain Gauge Network from 2002 to 2004. *Journal of Climate* 20: 1734-1750.

Gutzler, D.S.; Preston, J.W. 1997. Evidence for a relationship between spring snow cover in North America and summer rainfall in New Mexico. *Geophysical Research Letters* 24(17): 2207-2210.

Hales, J.E. 1972. Surges of maritime tropical air northward over the Gulf of California. *Monthly Weather Review* 100: 298-306.

Hargreaves, G.H. and Z.A. Samani 1982. Estimating potential evapotranspiration. J. Irrig. and Drain Engr., ASCE, 108(IR3):223-230.

Hargreaves, G.H. and Z.A. Samani, 1985. Reference crop evapotranspiration from temperature. Transaction of ASAE 1(2):96-99.

Hennessey, J.T.; Gibbens, R.P.; Tromble, J.M.; Cardenas, M. 1983. Water Properties of Caliche. *Journal of Range Management* 36(6): 723-726.

Hennessey, J.T.; Gibbens, R.P.; Tromble, J.M.; Cardenas, M. 1985. Mesquite (*Prosopis glandulosa* Torr) dunes and interdunes in southern New Mexico – A study of soil properties and soil water relations. *Journal of Arid Environments* 9: 27-38.

Higgins, R.W.; Yao, Y.; Yarosh, E.S.; Janowiak, J.E.; Mo, K.C. 1997. Influence of the Great Plains low-level jet on summertime precipitation and moisture transport over the central United States. *J. Clim*. 10: 481–507.

Horst, T.W.; Weil, J.C. 1992. Footprint estimation for scalar flux measurements in the atmospheric boundary layer. *Boundary-Layer Meteorol*. 59: 279–296.

Huenneke, L.F.; Clason, D.; Muldavin, E. 2001. Spatial heterogeneity in Chihuahuan Desert vegetation: Implications for sampling methods in semiarid ecosystems. *Journal of Arid Environments* 47: 257-270.

Huenneke, L.F.; Anderson, J.P.; Remmenga, M.; Schlesinger, W.H. 2002. Desertification alters patterns of aboveground net primary production in Chihuahuan ecosystems. *Global Change Biology* 8: 247-264.

Huenneke L.F., Schlesinger W.H. 2004. Patterns net primary production in chihuahan desert ecosystems. In Structure and Function of a Chihuahuan Desert Ecosystem: The Jornada Basin Long-Term Ecological Research Site, Havstad KM, Huenneke LF, Schlesinger WH (eds). Oxford University Press: Oxford; 232–246.

Huxman, T.E.; Snyder, K.A.; Tissue, D.; Leffler, A.J.; Ogle, K.; Pockman, W.T.; Sandquist, D.R.; Potts, D.L.; Schwinning, S. 2004. Precipitation pulses and carbon fluxes in semiarid and arid ecosystems. *Oecologia* 141: 254-268.

International Organization of Standards (ISO 4359). 1983. Liquid flow measurement in open channels - Rectangular, trapezoidal, and U-shaped flumes. Reference number: ISO 4359-1983(E).

IPCC, 2007: Climate Change 2007: The Physical Science Basis. Contribution of Working Group I to the Fourth Assessment Report of the Intergovernmental Panel on Climate Change [Solomon, S., D. Qin, M. Manning, Z. Chen, M. Marquis, K.B. Averyt,M. Tignor and H.L. Miller (eds.)]. Cambridge University Press, Cambridge, United Kingdom and New York, NY, USA.

Ivanov, V.Y.; Vivoni, E.R.; Bras, R.L.; Entekhabi, D. 2004. Catchment hydrologic response with a fully distributed triangulated irregular network model, *Water Resour. Res.* 40(11): W11102, doi:10.1029/2004WR003218.

Knapp A.K.; Fay, P.A.; Blair, J.M.; Collins, S.L.; Smith, M.D.; Carlisle, J.D.; Harper, C.W.; Danner, B.T.; Lett, M.S.; McCarron, J.K. 2002. Rainfall variability, carbon cycling, and plant species diversity in a mesic grassland. *Science* 298: 2202-2205.

Kurc S.A, Small E.E. 2007. Soil moisture variations and ecosystem-scale fluxes of water and carbon in semiarid grassland and shrubland. *Water Resources Research* 43: W06416, DOI:10.1029/2006WR005011.

Lado, M; Ben-Hur, M. 2004. Soil mineralogy effects on seal formation, runoff and soil loss. *Applied Clay Science* 24(3-4): 209-224.

Laio, F.; Poporato, A.; Ridolfi, L.; Rodriguez-Iturbe, I. 2001. Plants in water controlled ecosystems: active role in hydrologic processes and response to water stress II. Probabilistic soil moisture dynamics. *Advances in Water Resources* 24: 707-723.

Laliberte, A. S., Winters, C., and A. Rango, 2008, "A procedure for orthorectification of sub-decimeter resolution imagery obtained with an unmanned aerial vehicle (UAV)," in *ASPRS Annual Conference Proceedings*, Portland, OR, 28 Apr – 2 May, 2008.

Laliberte, A.S., Rango, A., 2011. Image Processing and Classification Procedures for Analysis of Sub-decimeter Imagery Acquired with an Unmanned Aircraft over Arid Rangelands. Giscience & Remote Sensing 48: 4-23.

Larson, L.W., Peck, E.L., 1974. Accuracy of precipitation measurements for hydrologic modeling. *Water Resour. Res*. 10, 857–863.

Leung, L.R.; Qian, Y.; Bian, X.D. 2003. Hydroclimate of the western United States based on observations and regional climate simulation of 1981-2000. part 1: Seasonal Statistics. *Journal of Climate* 16(12): 1892-1911.

Maddox, R.; McCollum, D.; Howard, K. 1995. Large-scale patterns associated with severe summertime thunderstorms over central Arizona. *Wea. Forecasting* 10: 763-778.

Mahrt, L. 1998. Flux sampling errors for aircraft and towers. *J.Atmos. Oceanic Technol*. 15: 416–429.

Mehrotra, R.; Sharma, A. 2011. Impact of atmospheric moisture in a rainfall downscaling framework for catchment-scale climate change impact assessment. *International Journal of Climatology* 31(3): 431-450.

Mendez-Barroso, L.A.; Vivoni, E.R. 2010. Observed shifts in land surface conditions during the North American monsoon: Implications for a vegetation-rainfall feedback mechanism, Journal of Arid Environments 74(5): 549-555.

Mendez-Barroso, L.A.; Vivoni, E.R.; Watts, C.J.; Rodrıguez, J.C. 2009. Seasonal and interannual relations between precipitation, surface soil moisture and vegetation dynamics in the North American monsoon region. *Journal of Hydrology* 377: 59–70.

Minet, J.; Laloy, E.; Lambot, S.; Vanclooster, M. 2011. Effect of high-resolution spatial soil moisture variability on simulated runodd response using a distributed hydrologic model. *Hydrol. Earth Syst. Sci.* 15: 1323-1338.

Monger, H. C., and B. T Bestelmeyer. 2006. The soil-geomorphic template and biotic change in arid and semiarid ecosystems. *Journal of Arid Environments* 65: 207-18.

Najafi, M.R.; Moradkhani, H.; Wherry, S.A. 2011. Statistical Downscaling of Precipitation Using Machine Learning with Optimal Predictor Selection. *Journal of Hydrologic Engineering* 16(8): 650-664.

Nash, M.S.; Wierenga, P.J.; Gutjahr, A. 1991. Time-series analysis of soil moisture and rainfall along a line transect in arid rangeland. *Soil Science*. 152:189-198.

Nie, D.; Kanemasu, E.T.; Fritschen, L.J.; Weaver, H.L.; Smith, E.A.; Verma, S.B.; Field, R.T.; Kustas, W.P.; Stewart, J.B. 1992. An intercomparison of surface energy flux measurement systems used during FIFE 1987. *J. Geophys. Res*. 97(D17): 18715–18724.

Notaro, M.; Liu, Z.Y.; Gallinore, R.G.; Williams, J.W.; Gutzler, D.S.; Collins, S. 2010. Complex seasonal cycle of ecohydrology in the Southwest United States. *Journal of Geophysical Research-Biogeosciences* 115: DOI: 10.1029/2010JG001382.

Okin, G. S., D. A. Gillette, and J. E. Herrick. 2006. Multi-scale controls on and consequences of aeolian processes in landscape change in arid and semiarid environments. *Journal of Arid Environments* 65: 253-75.

Peters, D.P.C.; Herrick, J.E.; Monger, H.C.; Huang, H. 2010. Soil-vegetation-climate interactions in arid landscapes: Effects of the North American monsoon on grass recruitment. *Journal of Arid Environments* 74(5): 618-623.

Pierson, F.B.; Blackburn, W.H.; Vanvactor, S.S.; Wood, J.C. 1994. Partitioning small-scale spatial variability of runoff and erosion on sagebrush rangeland. *Water Resources Bulletin* 30: 1081–1089.

Piles, M.; Camps, A.; Vall-Llossera, M.; Corbella, I.; Panciera, R.; Rudiger, C.; Kerr, Y.H.; Walker, J. 2011. Downscaling SMOS-Derived Soil Moisture Using MODIS

Visible/Infrared Data. *IEEE Transactions on Geoscience and Remote Sensing* 49(9): 3156-3166.

Reed, T.R. 1933. The North American high-level anticyclone. *Mon.Wea. Rev.,* 61: 321–325.

Renard, K.G. 1970. *The hydrology of semiarid rangleland watersheds*. ARS 41-62, USDA-ARS, Washington, DC.

Ridolfi, L.; D'Odorico, P.; Porporato, A.; Rodriguez-Iturbe, I. 2003. Stochastic soil moisture dynamics along a hillslope. *Journal of Hydrology*. 272: 264-275.

Schotanus, P., Nieuwstadt, F.T.M., De Bruin, H.A.R., 1983. Anemometer and its Application to Heat and Moisture Fluxes. Boundary Layer Meteorology. 26(1): 81-93.

Schmitz, T.J.; Mullen, S.L. 1996. Water Vapor transport associated with the summertime North American monsoon as depicted by ECMWF analyses. *J. Climate* 9: 1621-1633.

Schwinning, S.; Sala, O.E.; Loik, M.E.; Ehleringer, J.R., 2004. Thresholds, memory, and seasonality:understanding pulse dynamics in arid/semiarid ecosystems. *Oecologia* 141(2): 191-193.

Scott, R.L. 2010. Using watershed water balance to evaluate the accuracy of eddy covariance evaporation measurements for three semiarid ecosystems. *Agricultural and Forest Meteorology*. 150: 219-225.

Seyfried, M. S., L. E. Grant, E. Du, and K. Humes. 2005. Dielectric Loss and Calibration of the Hydra Probe Soil Water Sensor. Vadose Zone Journal 4:1070-1079.

Sher AA, Goldberg DE, Novoplansky A (2004) The effect of mean and variance in resource supply on survival of annuals from Mediterranean and desert environments. *Oecologia* 141(2): 353-362.

Snyder KA, Donovan LA, James JJ, Tiller RL, Richards JH (2004) Extensive summer water pulses do not necessarily lead to canopy growth of Great Basin and northern Mojave Desert shrubs. *Oecologia* 141(2): 325-334.

Sultana, Z.; Coulibaly, P. 2011. Distributed modeling of future changes in hydrological processes of Spencer Creek watershed. *Hydrological Processes* 25(8): 1254-1270.

Thomey, M.L.; Collins, S.L.; Vargas, R.; Johnson, J.E.; Brown, R.F.; Natvig, D.O.; Friggins, M.T. 2011. Effect of precipitation variability on net primary production and soil respiration in a Chihuahuan Desert grassland. *Global Change Biology* 17: 1505-1515.

Twine, T.E.; Kustas, W.P.; Norman, J.M.; Cook, D.R.; Houser, P.R.; Meyers, T.P.; Prueger, J.H.; Starks, P.J.; Wesely, M.L. 2000. Correcting eddy-covariance flux underestimates over a grassland. *Agri. and For. Meteor.* 103: 279-300.

Vivoni E.R.; Entekhabi, D.; Bras, R.L.; Ivanov, V.Y.; Van Horne, M.P.; Grassotti, C.; Hoffman, R.N. 2006. Extending the Predictability of Hydrometeorological Flood Events Using Radar Rainfall Nowcasting. *Journal of Hydrometeorology* 7: 660-677.

Vivoni, E.R.; Entekhabi, D.; Bras, R.L.; Ivanov, V.Y. 2007a. Controls on runoff generation and scale-dependence in a distributed hydrologic model, Hydrol. Earth Syst. Sci., 11(5), 1683– 1701.

Vivoni, E.R.; Gutierrez-Jurado, H.A.; Aragon, C.A.; Mendez-Barroso, L.A.; Rinehart, A.J.; Wyckoff, R.L.; Rodriguez, J.C.; Watts, C.J.; Bolten, J.D.; Lakshmi, V.; Jackson, T.J. 2007b. Variation of Hydrometeorological Conditions along a Topographic Transect in Northwestern Mexico during the North American Monsoon. *Journal of Climate* 20: 1792-1809.

Vivoni, E.R., Moreno, H.A.; Mascaro, G.; Rodriguez, J.C.; Watts, C.J.; Garatuza-Payan, J.; Scott, R. 2008. Observed relation between evapotranspiration and soil moisture in the North American monsoon region *Geophys. Res. Lett.* 35: doi:10.1029/2008GL036001.

Vivoni, E.R.; Rodriguez, J.C.; Watts, C.J. 2010. On the spatiotemporal variability of soil moisture and Evapotranspiration in a mountainous basin within the North American monsoon region. *Water Resources Research* 46: DOI: 10.1029/2009WR008240

Wainwright, J.; Parsons, A.J.; Abrahams, A.D. 2000. Plot-scale studies of vegetation, overland flow and erosion interactions: case studies from Arizona and New Mexico. *Hydrological Processes* 14: 2921-2943.

Wainwright, J., Parsons, A.J., Schlesinger, W.H., Abrahams, A.D. 2002. Hydrology-vegetation interactions in areas of discontinuous flow on a semiarid bajada, Southern New Mexico. J. of Arid Environ. 51:319-338.

Watts, C.J., Scott, R.L.; Garatuza-Payan, J; Rodrıguez, J.C.; Prueger, J.H.; Kustas, W.P.; Douglas, M. 2007. Changes in vegetation condition and surface fluxes during NAME 2004. *Journal of Climate* 20(9): 1810 -1820

Webb, E.K., Pearman, G.I., Leuning, R., 1980. Correction of flux measurements for density effects due to heat and water vapor transfer. Quart. J. R. Meteorol. Soc. 106, 85-106.

Wilczak, J.M., Oncley, S.P., Stage, S.A., 2001. Sonic anemometer tilt correction algorithms. Bound-Lay. Meteorol. 99, 127-150.

Yamanaka, T.; Yonetani, T. 1999. Dynamics of the evaporation zone in dry sandy soils, *J. Hydrol*. 217: 135–148.

Yao, J., D. P. C. Peters, K. M. Havstad, R. P. Gibbens, Herrick, J.E., 2006. Multi-scale factors and long-term responses of Chihuahuan Desert grasses to drought. *Landscape Ecology* 21, no. 8: 1217-31.

APPENDIX A

SAMPLING SENSORS

A.1. Watershed Sensor Network Locations

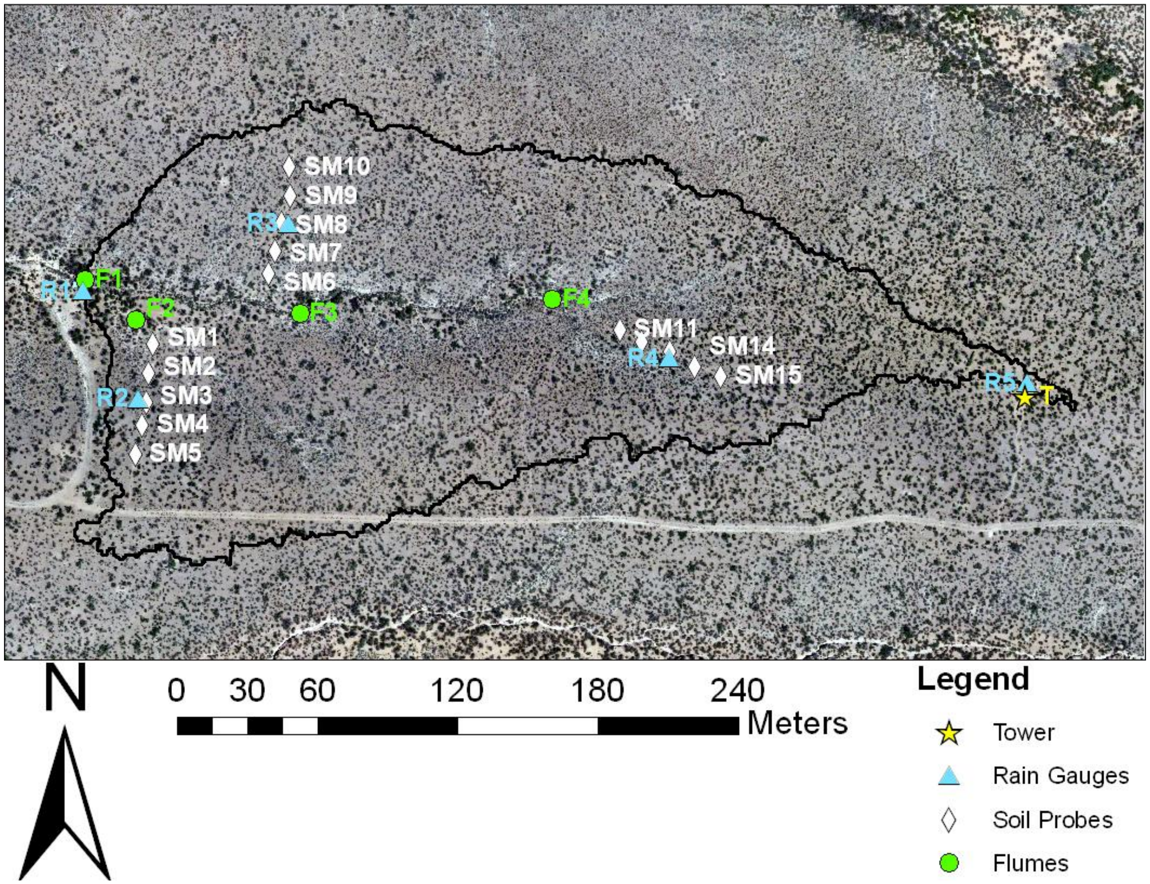

A.2. Miniflume Dimensions

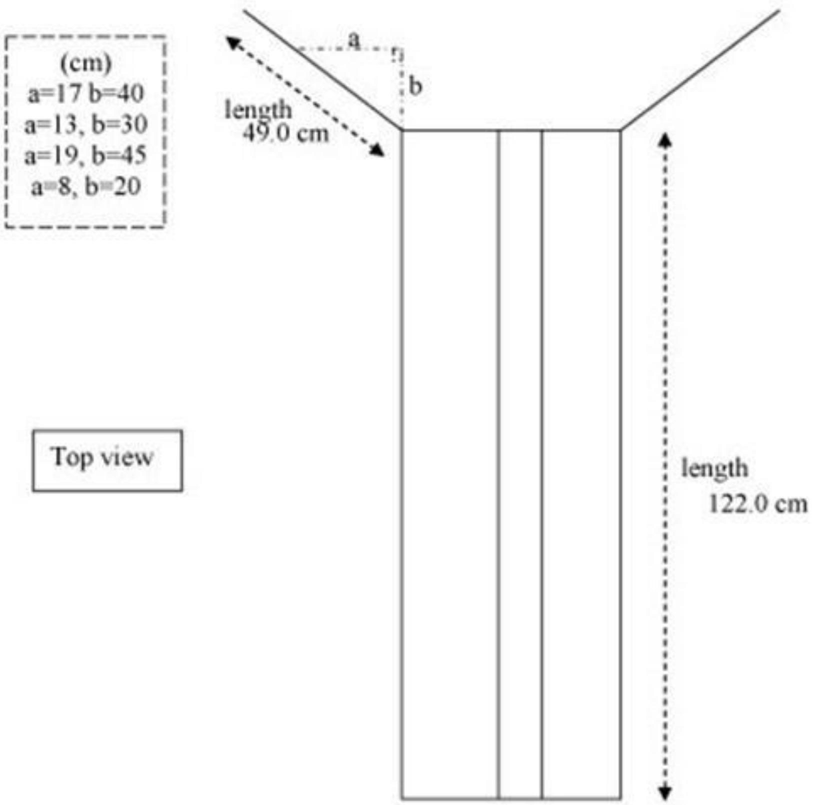

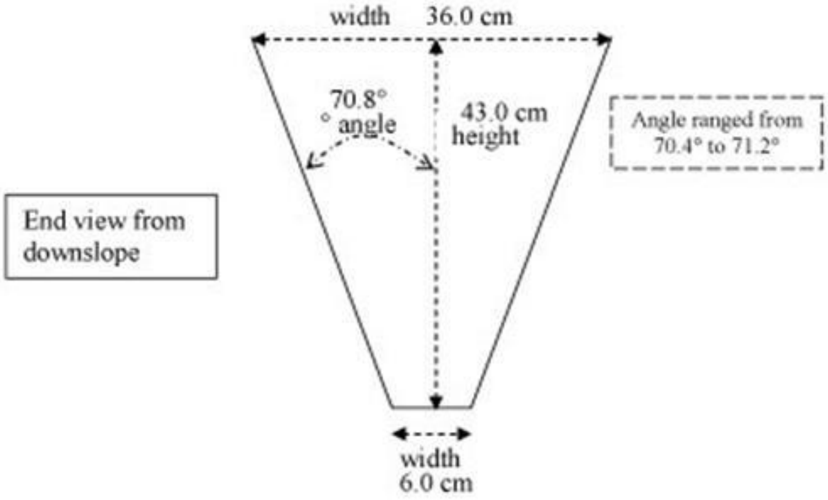

APPENDIX B

DATALOGGER PROGRAMS

B.1. Tower CR5000 Datalogger Program

```
‘CR5000 Series Datalogger
‘To create a different opening program template, type in new
‘instructions and select Template | Save as Default Template
‘date:June 23 2008
‘program author:Luis Mendez-Barroso and Ryan Templeton
‘Declare Public Variables

Public Batt_Volt
Public VW
Public PA_uS
Public VW_2
Public PA_uS_2
Public VW_3
Public PA_uS_3
Public VW_4
Public PA_uS_4
Public AirTC
Public RH
Public Rain_mm
Public Ptemp_C
Public Temp_C
Public Temp_C_2
Public Temp_C_3
Public Temp_C_4
Public Solar_Wm2
Public Solar_kJ
Public shf
Public shf_cal
Public shf_2
Public shf_cal_2
Public BP_mbar
Public Net_shortwave
Public Net_longwave
‘===Soil heatflux calibration variables
Public shf_mV
Public shf_mV_run
Public shf_mV_0
Public shf_mV_180
Public shf_mV_360
Public V_Rf
Public V_Rf_run
Public V_Rf_180
Public V_Rf_360
Public shf_cal_on                        ‘HFP01SC calibration flag.
Public shf_2_mV
Public shf_2_mV_run
Public shf_2_mV_0
Public shf_2_mV_180
```

```
Public shf_2_mV_360
Public V_Rf_2
Public V_Rf_2_run
Public V_Rf_2_180
Public V_Rf_2_360
Public shf_cal_2_on ‘HFP01SC calibration flag.
Public wind(5)                    ‘Wind, sonic temperature, and diagnostic data from
CSAT3.
Alias wind(1) = Ux
Alias wind(2) = Uy
Alias wind(3) = Uz
Alias wind(4) = Ts
Alias wind(5) = diag_csat
Units wind = m/s
Units Ts = degC
Units diag_csat = unitless

‘Declare variables for the Apogee surface temperature probe
Dim TT_K_6
Dim SBT_K_7
Dim m_8
Dim b_9
Public BattV
Public TT_C
Public SBT_C
Public TTmV


Public diag_bits(9)              ‘Warning flags.
Alias diag_bits(1) = del_T_f          ‘Delta temperature warning flag.
Alias diag_bits(2) = track_f          ‘Tracking (signal lock) warning flag.
Alias diag_bits(3) = amp_h_f           ‘Amplitude warning high flag.
Alias diag_bits(4) = amp_l_f           ‘Amplitude low warning flag.
Alias diag_bits(5) = chopper_f              ‘Chopper warning flag.
Alias diag_bits(6) = detector_f             ‘Detector warning flag.
Alias diag_bits(7) = pll_f            ‘PLL warning flag.
Alias diag_bits(8) = sync_f            ‘Synchronization warning flag.
Alias diag_bits(9) = agc              ‘Automatic gain control.
Units diag_bits = unitless

‘CS7500 has a fixed delay of 302.369 mSec (six scans at 20 Hz or three scans at 10 Hz).
Public irga(4)                                  ‘Co2, h2o, and pressure from the
CS7500 (LI-7500).
Alias irga(1) = co2
Alias irga(2) = h2o
Alias irga(3) = press
Alias irga(4) = diag_irga
Units co2 = mg/(m^3)
Units h2o = g/(m^3)
Units press = kPa
```

```
‘Analog variables with three or six scan delay.
Public fw                                        ‘Fine wire thermocouple temperature.
Units fw = degC
Public tc_ref                                    ‘Thermocouple reference temperature.
Units tc_ref = degC

‘Flux variables.
Public Fc                                        ‘CO2 flux.
Public LE                                        ‘Latent heat flux from CS7500 (LI-
7500).
Public Hs                                        ‘Sensible heat flux using sonic
temperature.
Public H                                         ‘Sensible heat flux using finewire
thermocouple.
Public tau                               ‘Momentum flux.
Public u_star                            ‘Friction velocity.
Public cov_out_1(32)             ‘Covariances of wind and scalars + windspeed.
Units Fc = mg/(m^2 s)
Units LE = W/m^2
Units Hs = W/m^2
Units H = W/m^2
Units tau = kg*m/s^2
Units u_star = m/s

‘Aliases for covariances.
Alias cov_out_1(1) = Uz_Uz_1
Alias cov_out_1(2) = Uz_Ux_1
Alias cov_out_1(3) = Uz_Uy_1
Alias cov_out_1(4) = Uz_co2_1
Alias cov_out_1(5) = Uz_h2o_1
Alias cov_out_1(6) = Uz_Ts_1
Alias cov_out_1(7) = Uz_fw_1
Alias cov_out_1(8) = Ux_Ux_1
Alias cov_out_1(9) = Ux_Uy_1
Alias cov_out_1(10) = Ux_co2_1
Alias cov_out_1(11) = Ux_h2o_1
Alias cov_out_1(12) = Ux_Ts_1
Alias cov_out_1(13) = Ux_fw_1
Alias cov_out_1(14) = Uy_Uy_1
Alias cov_out_1(15) = Uy_co2_1
Alias cov_out_1(16) = Uy_h2o_1
Alias cov_out_1(17) = Uy_Ts_1
Alias cov_out_1(18) = Uy_fw_1
Alias cov_out_1(19) = co2_co2_1
Alias cov_out_1(23) = h2o_h2o_1
Alias cov_out_1(26) = Ts_Ts_1
Alias cov_out_1(28) = fw_fw_1
Alias cov_out_1(31) = wnd_dir_compass
Units wnd_dir_compass = degrees
```

```
‘Alternate Flux variables using running mean.
Public cov_out_2(22)
‘Aliases for alternative covariances.
Alias cov_out_2(1) = Uz_Uz_2
Alias cov_out_2(2) = Uz_Ux_2
Alias cov_out_2(3) = Uz_Uy_2
Alias cov_out_2(4) = Uz_co2_2
Alias cov_out_2(5) = Uz_h2o_2
Alias cov_out_2(6) = Uz_Ts_2
Alias cov_out_2(7) = Uz_fw_2
Alias cov_out_2(8) = Ux_Ux_2
Alias cov_out_2(9) = Ux_Uy_2
Alias cov_out_2(10) = Ux_co2_2
Alias cov_out_2(11) = Ux_h2o_2
Alias cov_out_2(12) = Ux_Ts_2
Alias cov_out_2(13) = Ux_fw_2
Alias cov_out_2(14) = Uy_Uy_2
Alias cov_out_2(15) = Uy_co2_2
Alias cov_out_2(16) = Uy_h2o_2
Alias cov_out_2(17) = Uy_Ts_2
Alias cov_out_2(18) = Uy_fw_2
Alias cov_out_2(19) = co2_co2_2
Alias cov_out_2(20) = h2o_h2o_2
Alias cov_out_2(21) = Ts_Ts_2
Alias cov_out_2(22) = fw_fw_2
‘moving average variables
Dim primes(7)                   ‘fluctuations from means, consistent with cov_in
Dim move_avg(7)                         ‘moving averages
Dim x_prod(22)                          ‘cross products…to compute covariance

‘Diagnostic variables.
Public disable_flag_on(2)     ‘Intermediate processing disable.
    ‘disable_flag_on(1)     ‘Set high during site maintenance, flag(7) is set high.
    ‘disable_flag_on(2)     ‘Set high when CS7500 (LI-7500) failed to send data.
Public n(2)                     ‘Number of samples in the on-line covariances.
Public warnings(2)
Alias warnings(1) = csat_warnings     ‘Number of scans that at least one CSAT3
                                    ‘ warning flag was on.
Alias warnings(2) = irga_warnings     ‘Number of scans that the CS7500 (LI-7500)
Public flag(8)

‘Measurement variables without delays.
Dim wind_in(5)                                  ‘CSAT3 data, before adding delay.
Dim fw_in                                               ‘TC signal, before adding delay.
Dim tc_ref_in                                   ‘TC reference temperature, before
adding delay.

‘Arrays to store delayed data.
```

```
Dim analog_data(3)                          ‘Three or six scan old data from the
Data Table 3_6_scan.
Dim csat_data(5)                            ‘One or four scan old data from the Data
Table 1_4_scan.

Dim cov_in(7)                               ‘Array used in the covariance
instruction.
Dim j                                       ‘Counter variable.
Dim rTime(9)                                ‘Real time from CR5000 clock.
Dim scan_count                              ‘Counts the number scans that have
been executed.
Dim hex_number                                       ‘Used to break down the
diagnostic bits from the CSAT3.
Dim wind_east                               ‘Uy wind in compass coordinate system.
Dim wind_north                                       ‘Ux wind in compass coordinate
system.
Dim delays_loaded                           ‘A flag that gets set after three or six
scans have been executed.
                                                     ‘ This flag is used to ensure that
the Data Table 1_4_scan
                                                     ‘ and 3_6_scan are loaded with
data.
‘Declare Units
Units Batt_Volt=Volts
Units PA_uS=uSec
Units PA_uS_2=uSec
Units PA_uS_3=uSec
Units PA_uS_4=uSec
Units AirTC=Deg C
Units RH=%
Units Rain_mm=mm
Units Ptemp_C=Deg C
Units Temp_C=Deg C
Units Temp_C_2=Deg C
Units Temp_C_3=Deg C
Units Temp_C_4=Deg C
Units Solar_Wm2=W/m²
Units Solar_kJ=kJ/m²
Units shf = W/m^2
Units shf_2 = W/m^2
Units BP_mbar=mbar
Units Net_shortwave=W/m²
Units Net_longwave=W/m²
Units TT_C=Deg C
Units SBT_C=Deg C


‘Declare Constants
Const SCAN_INTERVAL = 50          ‘100 (mSec)                 50 (mSec)
```

```
Const CSAT_OPT = 10                      ‘10 (Hz)
        20 (Hz)
Const ANALOG_DELAY = 4                   ‘4 (3 scan delay)            7 (6
scan delay)
Const CSAT_DELAY = 2                     ‘2 (1 scan delay)            5 (4
scan delay)
Const GAMMA = 400                        ‘time constant in seconds

Const ANGLE_FROM_NORTH = 216             ‘Negative when West of North, positive
when East of North.
Const CP = 1003                          ‘Estimate of heat capacity of air [J/(kg
K)].
Const LV = 2440                          ‘Estimate of the latent heat of
vaporization [J/g].
Const RHO = 1.2                          ‘Estimate for air density at sea level
[kg/m^3].
Const SDM_PER = 30                       ‘Default SDM clock speed, 30 uSec bit
period.

Const A_0 = 6.107799961                  ‘Coefficients for the sixth order
approximating
Const A_1 = 4.436518521e-1          ‘ saturation vapor pressure polynomial (Lowe,
Const A_2 = 1.428945805e-2          ‘ Paul R., 1976.:  An approximating polynomial
for
Const A_3 = 2.650648471e-4          ‘ computation of saturation vapor pressure, J.
Appl.
Const A_4 = 3.031240396e-6          ‘ Meteor., 16, 100-103).
Const A_5 = 2.034080948e-8
Const A_6 = 6.136820929e-11

‘constants to convert voltage to ppm of  co2.
‘Const Crange = 1000
‘Const Vrange = 5

‘constants to convert voltage to ppt of  h20.
‘Const Hrange = 80
Const HFP01SC_CAL = 1000/64.3       ‘Unique multiplier for HFP01SC 1
(1000/sensitivity).
Const HFP01SC_CAL_2 = 1000/63.5 ‘Unique multiplier for HFP01SC 2
(1000/sensitivity).
Const CAL_INTERVAL = 180            ‘HFP01SC insitu calibration interval (minutes).


‘Define Data Tables
DataTable(Met,True,1344)
  CardOut (0,1344)
        DataInterval(0,30,Min,10)
        Average(1,VW,FP2,False)
        Average(1,VW_2,FP2,False)
        Average(1,VW_3,FP2,False)
```

```
        Average(1,VW_4,FP2,False)
        Average(1,AirTC,FP2,False)
        Average(1,RH,FP2,False)
        Totalize(1,Rain_mm,FP2,False)
        Average(1,Temp_C,FP2,False)
        Average(1,Temp_C_2,FP2,False)
        Average(1,Temp_C_3,FP2,False)
        Average(1,Temp_C_4,FP2,False)
        Average(1,Ptemp_C,FP2,False)
        Average(1,Solar_Wm2,FP2,False)
        Totalize(1,Solar_kJ,IEEE4,False)
        Average (1,shf,IEEE4,shf_cal_on)
  Average (1,shf_2,IEEE4,shf_cal_2_on)
  Average(1,Net_shortwave,FP2,False)
        Average(1,Net_longwave,FP2,False)
        Average(1,BP_mbar,FP2,False)
        Minimum(1,Batt_Volt,FP2,False,False)
        Average(1,PA_uS,FP2,False)
        Average(1,PA_uS_2,FP2,False)
        Average(1,PA_uS_3,FP2,False)
        Average(1,PA_uS_4,FP2,False)
        Sample(1,TT_C,FP2)
        Sample(1,SBT_C,FP2)
EndTable

DataTable(Tips,True,1000)
  DataEvent (0,Rain_mm>0,Rain_mm=0,0)
  Sample (1,Rain_mm,FP2)
EndTable

DataTable (raw_in,TRUE,1)
  Sample (5,wind_in(1),IEEE4)
  Sample (3,irga(1),IEEE4)
  Sample (1,fw_in,IEEE4)
  Sample (1,tc_ref_in,IEEE4)
EndTable

‘Delay the analog measurements by three or six scans.
DataTable (scan_3_6,TRUE,ANALOG_DELAY)
  Sample (1,tc_ref_in,IEEE4)
  Sample (1,fw_in,IEEE4)
EndTable

‘Delay the CSAT3 measurements by one or four scans.
DataTable (scan_1_4,TRUE,CSAT_DELAY)
  Sample (5,wind_in(1),IEEE4)
EndTable

‘Set flag(8) high to save time series data.  Set flag(5) also
‘to break up the time series data file into one hour periods.
```

```
DataTable (ts_data,flag(8),-1)
  DataInterval (0,SCAN_INTERVAL,mSec,50)
  CardOut (0,-1)
  Sample (3,wind(1),IEEE4)
  Sample (2,irga(1),IEEE4)
  Sample (1,Ts,IEEE4)
  Sample (1,press,IEEE4)
  Sample (1,diag_csat,IEEE4)
‘  Sample (1,diag_irga,IEEE4)
EndTable

‘Compute the covariances of vertical wind, co2, h2o, natural log of
‘ the krypton voltage, sonic temperature, and finewire thermocouple
‘ temperature, as well as the other cross products, required to rotate
‘ the data into natural wind coordinates.  This data is output every
‘ 30 minutes.
DataTable (comp_cov,TRUE,1)
  DataInterval (0,30,min,1)
  Covariance (7,cov_in(1),IEEE4,(disable_flag_on(1) OR disable_flag_on(2) OR NOT
(flag(7))),28)
  WindVector (1,wind_east,wind_north,IEEE4,(disable_flag_on(1) OR NOT
(flag(7))),0,1,2)
EndTable

‘Alternative covariance calculation for 21 days
DataTable (alt_cov,TRUE,1)
  DataInterval (0,30,min,1)
  Average (22,x_prod(1),IEEE4,(disable_flag_on(1) OR disable_flag_on(2) OR NOT
(flag(7))))
EndTable

‘This table will hold 28 days of flux data.  This data is
‘output every 30 minutes.
DataTable (flux,TRUE,1344)
  DataInterval (0,30,Min,10)
  CardOut (0,1344)
  Sample (1,Fc,IEEE4)
  Sample (1,LE,IEEE4)
  Sample (1,Hs,IEEE4)
  Sample (1,H,IEEE4)
  Sample (1,u_star,IEEE4)
  Sample (19,cov_out_1(1),IEEE4)
  Sample (1,cov_out_1(23),IEEE4)
  Sample (1,cov_out_1(26),IEEE4)
  Sample (1,cov_out_1(28),IEEE4)

  Average (3,wind(1),IEEE4,(disable_flag_on(1) OR NOT (flag(7)))
  Average (2,irga(1),IEEE4,(disable_flag_on(2) OR NOT (flag(7)))
  Average (1,fw_in,IEEE4,(disable_flag_on(1) OR NOT (flag(7))))
  Average (1,Ts,IEEE4,(disable_flag_on(1) OR NOT (flag(7)))
```

```
  Average (1,press,IEEE4,disable_flag_on(2))
  Average (1,tc_ref,FP2,FALSE)

  Sample (1,wnd_dir_compass,FP2)
  WindVector (1,Uy,Ux,FP2,(disable_flag_on(1) OR NOT (flag(7))),0,1,2)
  Average (1,Batt_volt,FP2,FALSE)



  Totalize (1,n(1),IEEE4,FALSE)
  Totalize (2,warnings(1),IEEE4,FALSE)
  Sample (22,cov_out_2(1),IEEE4)
EndTable

‘Define subroutines
‘Sub hfp01sc_cal ‘Begin HFP01SC calibration one minute into every CAL_INTERVAL
minutes.
  ‘If ( IfTime (1,CAL_INTERVAL,Min) ) Then
    ‘shf_cal_on = TRUE
    ‘Move (shf_mV_0,1,shf_mV_run,1)
    ‘SW12=TRUE
  ‘EndIf

  ‘If ( IfTime (4,CAL_INTERVAL,Min) ) Then
    ‘Move (shf_mV_180,1,shf_mV_run,1)
    ‘Move (V_Rf_180,1,V_Rf_run,1)
    ‘SW12=FALSE
  ‘EndIf

  ‘If ( IfTime (19,CAL_INTERVAL,Min) ) Then
    ‘Move (shf_mV_360,1,shf_mV_run,1)
   ‘Compute new HFP01SC calibration factors.
      ‘shf_cal = V_Rf_180*V_Rf_180*128.7/ ABS(((shf_mV_0+shf_mV_360)/2)-
shf_mV_180)
   ‘Stop filtering data
   ‘shf_cal_on = FALSE
    ‘EndIf
‘EndSub ‘End HFP01SC calibration sequence.

‘Sub hfp01sc_cal_2  ‘Begin HFP01SC PLATE 2 calibration one minute into every
CAL_INTERVAL minutes.
  ‘If ( IfTime (1,CAL_INTERVAL,Min) ) Then
    ‘shf_cal_2_on = TRUE
    ‘Move (shf_2_mV_0,1,shf_2_mV_run,1)
    ‘SW12=TRUE
  ‘EndIf

  ‘If ( IfTime (4,CAL_INTERVAL,Min) ) Then
    ‘Move (shf_2_mV_180,1,shf_2_mV_run,1)
```

```
    ‘Move (V_Rf_2_180,1,V_Rf_2_run,1)
    ‘SW12=FALSE
  ‘EndIf

  ‘If ( IfTime (19,CAL_INTERVAL,Min) ) Then
    ‘Move (shf_2_mV_360,1,shf_2_mV_run,1)
   ‘Compute new HFP01SC calibration factors.
      ‘shf_cal_2 = V_Rf_180*V_Rf_180*128.7/ ABS(((shf_mV_0+shf_mV_360)/2)-
shf_mV_180)
   ‘Stop filtering data
   ‘shf_cal_2_on = FALSE
    ‘EndIf
‘EndSub ‘End HFP01SC calibration sequence.

‘Main Program
BeginProg

flag(1) = TRUE
  flag(7) = TRUE
  flag(8) = TRUE

‘initiate moving average
  For j = 1 To 7
    move_avg(j) = 0
  Next j

 ‘Set all CSAT3 variables to NaN.
  For j = 1 To 5
    wind_in(j) = NaN
  Next j

 ‘Set all CS7500 (LI-7500) variables to NaN.
  For j = 1 To 4
      irga(j) = NaN
  Next j

 ‘Set the SDM clock speed.
  SDMSpeed (SDM_PER)

Scan(SCAN_INTERVAL,mSec,10,0)

   ‘Get CSAT3 wind and sonic temperature data.
    CSAT3 (wind_in(1),1,3,91,CSAT_OPT)

   ‘Get CS7500 (LI-7500) data.
    CS7500 (irga(1),1,7,6)

   ‘Convert CS7500 (LI-7500) data from molar density [mmol/m^3] to mass density.
   ‘ 44 [g/mol] – molecular weight of carbon dioxide
   ‘ 0.018 [g/mmol] – molecular weight of water vapor
```

```
 If (NOT (co2 = -99999)) Then (co2 = co2 * 44)
 h2o = h2o * 0.018

             ‘Get the battery voltage from the Status Table.
 Batt_Volt = Status.Battery(1,1)

      ‘If Batt_volt is < 11 Turn OFF IRGA
      If Batt_Volt < 11 Then
             WriteIO (&B10,&B00)
             flag(1) = TRUE
      EndIf
      If (flag(1) = TRUE AND Batt_Volt > 11.5) Then ‘Turning IRGA back ON
             WriteIO (&B10,&B10)
             flag(1) = FALSE
      EndIf


‘Call humedad table.
 ‘CallTable moisture

‘Display the raw, unshifted turbulence data.
 CallTable raw_in

 ‘Delay the analog measurements by three or six scans.
 CallTable scan_3_6

 ‘Delay the CSAT3 measurements by one or four scans.
 CallTable scan_1_4

 If (NOT delays_loaded) Then (scan_count = scan_count + 1)
 If (scan_count = ANALOG_DELAY) Then (delays_loaded = TRUE)

 ‘Load in analog measurements that have been delayed by three or six scans.
 GetRecord (analog_data(1),scan_3_6,ANALOG_DELAY)
 tc_ref = analog_data(1)
 fw = analog_data(2)

 ‘Load in CSAT3 measurements that have been delayed by one or four scans.
 GetRecord (csat_data(1),scan_1_4,CSAT_DELAY)
 Ux = csat_data(1)
 Uy = csat_data(2)
 Uz = csat_data(3)
 Ts = csat_data(4)
 diag_csat = csat_data(5)
 wind_east = -1 * csat_data(2)
 wind_north = csat_data(1)

‘Turn on the intermediate processing disable flag when the CSAT3 is reporting NaN, a
 ‘Lost Trigger (&hf000), No Data (&hf03f), or an SDM error (&hf001).
```

```
    If ( (diag_csat = NaN) OR (diag_csat = &hf000) OR (diag_csat = &hf03f) OR
(diag_csat = &hf001))
      disable_flag_on(1) = TRUE
    Else
     ‘Check for any warning flags in CSAT3 data.  Filter all measurements associated
     ‘ with the CSAT3, when the warning flags are set.
      If (diag_csat AND &hf000)
        csat_warnings = 1
        disable_flag_on(1) = TRUE
      Else
        csat_warnings = 0
        disable_flag_on(1) = FALSE
      EndIf
    EndIf

‘Keep the four most significant bits of the diagnostic word.
    diag_csat = INT ((diag_csat AND &hf000)/&h1000 + 0.5)

   ‘Break down the four most significant bits of the diagnostic word
   ‘ into a delta temperature flag, poor signal lock (tracking flag),
   ‘ amplitude high flag, and amplitude low flag.
    hex_number = &h0008
    For j = 1 To 4
      If ( ((diag_csat AND hex_number) = hex_number) AND NOT (diag_csat = &h000f)
)
        diag_bits(j) = 1
      Else
        diag_bits(j) = 0
      EndIf

      If ( diag_csat = NaN ) Then ( diag_bits(j) = NaN )

      hex_number = INT ((hex_number/&h0002) + 0.5)
    Next j

   ‘Compute the AGC.
    agc = INT ((diag_irga AND &h000f) * 6.25 + 0.5)

   ‘Keep the four most significant bits of the CS750 (LI-7500) diagnostic word
   ‘ and swap bits.
    diag_irga = (NOT (INT ((diag_irga AND &h00f0)/&h0010 + 0.5)) AND &h000f)

   ‘Turn on the intermediate processing disable flag when the CS7500 (LI-7500) has
   ‘ failed to send data to the CR5000 via SDM.
‘    If ( (ABS (co2) >= 99990) OR (co2 = NaN) )
     If ( (co2 >=2000) OR (co2<=0) OR (co2 = NaN) OR (h2o <=0) OR (h2o >=50) )
      disable_flag_on(2) = TRUE
        irga_warnings = 1
    Else
     ‘Check for any warning flags in CS7500 (LI-7500) data.  Filter all measurements
```

```
    ‘ associated with the CS7500 (LI-7500), when the warning flags are set.
    If (diag_irga AND &h000f)
      irga_warnings = 1
      disable_flag_on(2) = TRUE
    Else
      irga_warnings = 0
      disable_flag_on(2) = FALSE
    EndIf
  EndIf

  ‘Decompose the warning flags.  Li-Cor uses reverse logic, e.g., bit set is okay.
  ‘The program changes the logic, e.g., bit not set is okay.
  hex_number = &h0008
  For j = 1 To 4
    If ( (diag_irga AND hex_number) = hex_number)
      diag_bits(j+4) = 1
    Else
      diag_bits(j+4) = 0
    EndIf

    If ( (ABS (co2) >= 99990) OR (co2 = NaN) ) Then ( diag_bits(j+4) = NaN )
    hex_number = INT ((hex_number/&h2) + 0.5)
  Next j


  ‘Perform time series and flux processing only after the Table 3_6_scan is loaded with
data.
  If (delays_loaded)

    ‘Write a file mark to the time series table every day.  The file mark is written only to
    ‘ to the PC Card if flag(5) is set high by the station operator and time series data are
being
    ‘ stored [flag(8) is high].  Both flag(8) and flag(5) must be set high by the station
operator
    ‘ using PC9000 or the CR5000 keyboard.

    If (flag(5) AND flag(8) AND IfTime (0,1440,Min) ) Then (FileMark (ts_data))
    CallTable ts_data

    ‘Load cov_in() array for the covariance computation.
    cov_in(1) = Uz
    cov_in(2) = Ux
    cov_in(3) = Uy
    cov_in(4) = co2
    cov_in(5) = h2o
    cov_in(6) = Ts
    cov_in(7) = fw

    CallTable comp_cov
```

```
‘compute deviations from moving average
        For j = 1 To 7
                If (NOT disable_flag_on(1) AND NOT disable_flag_on(2) AND flag(7)
AND NOT (cov_in(j) = NaN) )
                        move_avg(j)=move_avg(j)*EXP(-1/(CSAT_OPT*GAMMA)) +
cov_in(j)*(1-EXP(-1/(CSAT_OPT*GAMMA)))
                        primes(j)=cov_in(j)-move_avg(j)
                EndIf
        Next j
        If (NOT disable_flag_on(1) AND NOT disable_flag_on(2) AND flag(7))
                x_prod(1)=primes(1)*primes(1)
                x_prod(2)=primes(1)*primes(2)
                x_prod(3)=primes(1)*primes(3)
                x_prod(4)=primes(1)*primes(4)
                x_prod(5)=primes(1)*primes(5)
                x_prod(6)=primes(1)*primes(6)
                x_prod(7)=primes(1)*primes(7)
                x_prod(8)=primes(2)*primes(2)
                x_prod(9)=primes(2)*primes(3)
                x_prod(10)=primes(2)*primes(4)
                x_prod(11)=primes(2)*primes(5)
                x_prod(12)=primes(2)*primes(6)
                x_prod(13)=primes(2)*primes(7)
                x_prod(14)=primes(3)*primes(3)
                x_prod(15)=primes(3)*primes(4)
                x_prod(16)=primes(3)*primes(5)
                x_prod(17)=primes(3)*primes(6)
                x_prod(18)=primes(3)*primes(7)
                x_prod(19)=primes(4)*primes(4)
                x_prod(20)=primes(5)*primes(5)
                x_prod(21)=primes(6)*primes(6)
                x_prod(22)=primes(7)*primes(7)
        EndIf

        CallTable alt_cov

   ‘Keep track of the number of samples in the covariances.
    If (NOT disable_flag_on(1) AND NOT disable_flag_on(2) AND flag(7))
      n(1) = 1
    Else
      n(1) = 0
    EndIf


    If (comp_cov.Output(1,1))

      GetRecord (cov_out_1(1),comp_cov,1)

      wnd_dir_compass = wnd_dir_compass + ANGLE_FROM_NORTH
           wnd_dir_compass = wnd_dir_compass MOD 360
```

```
    ‘Compute on-line fluxes.
    Fc = Uz_co2_1
    LE = LV * Uz_h2o_1
    Hs = RHO * CP * Uz_Ts_1
    H = RHO * CP * Uz_fw_1
    tau = SQR ((Uz_Ux_1)^2 + (Uz_Uy_1)^2)
    u_star = SQR (tau)
    tau = RHO * tau

   EndIf

      If (alt_cov.Output(1,1))
            GetRecord (cov_out_2(1),alt_cov,1)
      EndIf

   CallTable flux

  EndIf

            ‘Default Datalogger Battery Voltage measurement Batt_Volt:
            Battery(Batt_Volt)
            ‘CS616 Water Content Reflectometer measurements VW and PA_uS:
            PortSet(1,1)
            PeriodAvg(PA_uS,1,mV5000,1,0,0,100,10,1,0)
            PortSet(1,0)
            VW=-0.0663+(-0.0063*PA_uS)+(0.0007*PA_uS^2)
            ‘CS616 Water Content Reflectometer measurements VW_2 and
PA_uS_2:
            PortSet(2,1)
            PeriodAvg(PA_uS_2,1,mV5000,2,0,0,100,10,1,0)
            PortSet(2,0)
            VW_2=-0.0663+(-0.0063*PA_uS_2)+(0.0007*PA_uS_2^2)
            ‘CS616 Water Content Reflectometer measurements VW_3 and
PA_uS_3:
            PortSet(3,1)
            PeriodAvg(PA_uS_3,1,mV5000,3,0,0,100,10,1,0)
            PortSet(3,0)
            VW_3=-0.0663+(-0.0063*PA_uS_3)+(0.0007*PA_uS_3^2)
            ‘CS616 Water Content Reflectometer measurements VW_4 and
PA_uS_4:
            PortSet(4,1)
            PeriodAvg(PA_uS_4,1,mV5000,4,0,0,100,10,1,0)
            PortSet(4,0)
            VW_4=-0.0663+(-0.0063*PA_uS_4)+(0.0007*PA_uS_4^2)
            ‘HMP45C (6-wire) Temperature & Relative Humidity Sensor
measurements AirTC and RH:
            VoltSe(AirTC,1,mV1000,5,0,0,250,0.1,-40.0)
            VoltSe(RH,1,mV1000,6,0,0,250,0.1,0)
            If RH>100 AND RH<108 Then RH=100
```

```
                fw=AirTC*1.0
                fw_in=AirTC*1.0
                If (fw_in = NaN) Then fw_in = 0
                ‘TE525/TE525WS Rain Gauge measurement Rain_mm:
                PulseCount(Rain_mm,1,1,2,0,0.254,0)
                ‘Wiring Panel Temperature measurement Ptemp_C:
                PanelTemp(Ptemp_C,250)
                tc_ref=Ptemp_C*1.0
                tc_ref_in=Ptemp_C*1.0
                ‘Type E (chromel-constantan) Thermocouple measurements Temp_C:
                TCDiff(Temp_C,1,mV20C,6,TypeE,Ptemp_C,True,0,250,1,0)
                ‘Type E (chromel-constantan) Thermocouple measurements Temp_C_2:
                TCDiff(Temp_C_2,1,mV20C,7,TypeE,Ptemp_C,True,0,250,1,0)
                ‘Type E (chromel-constantan) Thermocouple measurements Temp_C_3:
                TCDiff(Temp_C_3,1,mV20C,8,TypeE,Ptemp_C,True,0,250,1,0)
                ‘Type E (chromel-constantan) Thermocouple measurements Temp_C_4:
                TCDiff(Temp_C_4,1,mV20C,9,TypeE,Ptemp_C,True,0,250,1,0)
                CallTable(Tips)
        NextScan


        SlowSequence
        shf_cal = HFP01SC_CAL
shf_cal_2 = HFP01SC_CAL_2
        Scan(1,Sec,1,0)
        ‘CM3 Pyranometer measurements Solar_kJ and Solar_Wm2:
                VoltDiff(Solar_Wm2,1,mV50,5,True,0,250,68.166,0)
                If Solar_Wm2<0 Then Solar_Wm2=0
                Solar_kJ=Solar_Wm2*0.2
                ‘CS100 Barometric Pressure Sensor measurement BP_mbar:
                PortSet(7,1)
                VoltSe(BP_mbar,1,mV5000,7,1,0,250,0.2,600.0)
                BP_mbar=BP_mbar*1.0
                ‘CNR2 Net radiation measurements
                VoltDiff(Net_shortwave,1,mV20,19,True,200,250,57.1755,0.0)
                VoltDiff(Net_longwave,1,mV20,20,True,0,250,77.0416,0.0)
                ‘Measure the HFP01SC soil heat flux plate 1.
 VoltDiff(shf_mV,1,mV50,11,FALSE,200,200,1,0)
 shf = shf_mV * shf_cal
‘Measure voltage across the heater (Rf_V).
 VoltDiff(V_Rf, 1, mV5000, 12, FALSE, 200, 200, 0.001, 0)
‘Maintain filtered values for calibration.
 AvgRun (shf_mV_run,1,shf_mV,100)
 AvgRun (V_Rf_run,1,V_Rf,100)
 ‘Call hfp01sc_cal
        ‘Measure the HFP01SC soil heat flux plate 2.
 VoltDiff(shf_2_mV,1,mV50,13,FALSE,200,200,1,0)
 shf_2 = shf_2_mV * shf_cal_2
‘Measure voltage across the heater (Rf_V).
 VoltDiff(V_Rf_2, 1, mV5000, 14, FALSE, 200, 200, 0.001, 0)
```

```
   ‘Maintain filtered values for calibration.
    AvgRun (shf_2_mV_run,1,shf_2_mV,100)
    AvgRun (V_Rf_2_run,1,V_Rf_2,100)
    ‘Call hfp01sc_cal_2
    ‘Run the Apogee program to calculate the target temperature
               ‘Measure IRR-P sensor body thermistor temperature
                         BrHalf(SBT_C,1,mV5000,31,1,1,5000,True,0,250,1,0)
                         SBT_C=24900*(1/SBT_C-1)
                         SBT_C=LOG(SBT_C)
                         SBT_C=1/(1.129241e-3+2.341077e-4*SBT_C+8.775468e-8*(SBT_C^3))-273.15
                         ‘Measure IRR-P mV output of thermopile
                         VoltDiff(TTmV,1,mV20,15,True,0,250,1,0)
                         ‘Calculate slope (m) and offset (b) coefficients for target temperature calculation
                         m_8=1340820000+(7418550*SBT_C)+(72785*SBT_C^2)
                         b_9=14841900+(118490*SBT_C)+(23378*SBT_C^2)
                         ‘Calculate target temperature using calculated slope (m) and offset (b)
                         SBT_K_7=SBT_C+273.15
                         TT_K_6=SBT_K_7^4+TTmV*m_8+b_9
                         TT_K_6=SQR(SQR(TT_K_6))
                         ‘Convert target temperature into desired units
                         TT_C=TT_K_6-273.15
                         ‘Call Output Tables
                         CallTable (Met)
             NextScan
EndProg
```

B.2. Transect CR800 Datalogger Program

```
'CR800 Series for Hydraprobe Transect #1 in the Jornada LTER Tromble Weir
'Created by Ryan Templeton 5-5-2010

'Declare Variables and Units
Public BattV
Public HP(2)
Public HP_1(2)
Public HP_2(2)
Public HP_3(2)
Public HP_4(2)
Public HP_5(2)
Public HP_6(2)
Public HP_7(2)
Public HP_8(2)
Public HP_9(2)
Public HP_a(2)
Public HP_b(2)
Public HP_c(2)
Public HP_d(2)
Public HP_e(2)
Public Rain_mm
Public CS450(2)


Alias HP(1)=Temp_C
Alias HP(2)=SW_wfv
Alias HP_1(1)=Temp_C_1
Alias HP_1(2)=SW_wfv_1
Alias HP_2(1)=Temp_C_2
Alias HP_2(2)=SW_wfv_2
Alias HP_3(1)=Temp_C_3
Alias HP_3(2)=SW_wfv_3
Alias HP_4(1)=Temp_C_4
Alias HP_4(2)=SW_wfv_4
Alias HP_5(1)=Temp_C_5
Alias HP_5(2)=SW_wfv_5
Alias HP_6(1)=Temp_C_6
Alias HP_6(2)=SW_wfv_6
Alias HP_7(1)=Temp_C_7
Alias HP_7(2)=SW_wfv_7
Alias HP_8(1)=Temp_C_8
Alias HP_8(2)=SW_wfv_8
Alias HP_9(1)=Temp_C_9
Alias HP_9(2)=SW_wfv_9
Alias HP_a(1)=Temp_C_a
Alias HP_a(2)=SW_wfv_a
Alias HP_b(1)=Temp_C_b
Alias HP_b(2)=SW_wfv_b
```

```
Alias HP_c(1)=Temp_C_c
Alias HP_c(2)=SW_wfv_c
Alias HP_d(1)=Temp_C_d
Alias HP_d(2)=SW_wfv_d
Alias HP_e(1)=Temp_C_e
Alias HP_e(2)=SW_wfv_e
Alias CS450(1)=Level
Alias CS450(2)=PTemp_C


Units BattV=Volts
Units Temp_C=C
Units SW_wfv=Wfv(m3m-3)
Units Temp_C_1=C
Units SW_wfv_1=Wfv(m3m-3)
Units Temp_C_2=C
Units SW_wfv_2=Wfv(m3m-3)
Units Temp_C_3=C
Units SW_wfv_3=Wfv(m3m-3)
Units Temp_C_4=C
Units SW_wfv_4=Wfv(m3m-3)
Units Temp_C_5=C
Units SW_wfv_5=Wfv(m3m-3)
Units Temp_C_6=C
Units SW_wfv_6=Wfv(m3m-3)
Units Temp_C_7=C
Units SW_wfv_7=Wfv(m3m-3)
Units Temp_C_8=C
Units SW_wfv_8=Wfv(m3m-3)
Units Temp_C_9=C
Units SW_wfv_9=Wfv(m3m-3)
Units Temp_C_a=C
Units SW_wfv_a=Wfv(m3m-3)
Units Temp_C_b=C
Units SW_wfv_b=Wfv(m3m-3)
Units Temp_C_c=C
Units SW_wfv_c=Wfv(m3m-3)
Units Temp_C_d=C
Units SW_wfv_d=Wfv(m3m-3)
Units Temp_C_e=C
Units SW_wfv_e=Wfv(m3m-3)
Units Rain_mm=mm
Units Level=psig
Units PTemp_C=C


'Define Data Tables
DataTable(Avgs,True,1400)
  DataInterval(0,30,Min,10)
  Minimum(1,BattV,FP2,False,False)
```

```
  Average(1,Temp_C,FP2,0)
  Average(1,SW_wfv,FP2,0)
  Average(1,Temp_C_1,FP2,0)
  Average(1,SW_wfv_1,FP2,0)
  Average(1,Temp_C_2,FP2,0)
  Average(1,SW_wfv_2,FP2,0)
  Average(1,Temp_C_3,FP2,0)
  Average(1,SW_wfv_3,FP2,0)
  Average(1,Temp_C_4,FP2,0)
  Average(1,SW_wfv_4,FP2,0)
  Average(1,Temp_C_5,FP2,0)
  Average(1,SW_wfv_5,FP2,0)
  Average(1,Temp_C_6,FP2,0)
  Average(1,SW_wfv_6,FP2,0)
  Average(1,Temp_C_7,FP2,0)
  Average(1,SW_wfv_7,FP2,0)
  Average(1,Temp_C_8,FP2,0)
  Average(1,SW_wfv_8,FP2,0)
  Average(1,Temp_C_9,FP2,0)
  Average(1,SW_wfv_9,FP2,0)
  Average(1,Temp_C_a,FP2,0)
  Average(1,SW_wfv_a,FP2,0)
  Average(1,Temp_C_b,FP2,0)
  Average(1,SW_wfv_b,FP2,0)
  Average(1,Temp_C_c,FP2,0)
  Average(1,SW_wfv_c,FP2,0)
  Average(1,Temp_C_d,FP2,0)
  Average(1,SW_wfv_d,FP2,0)
  Average(1,Temp_C_e,FP2,0)
  Average(1,SW_wfv_e,FP2,0)
  Totalize(1,Rain_mm,FP2,0)
  Average(1,Level,FP2,0)
  Average(1,PTemp_C,FP2,0)
EndTable

DataTable(Tips,True,1000)
  DataEvent (0,Rain_mm>0,Rain_mm=0,0)
  Sample (1,Rain_mm,FP2)
EndTable

DataTable(PT,True,-1)
        DataInterval(0,1,min,10)
        Average(1,Level,FP2,0)
EndTable

'Main Program
BeginProg
  Scan(1,Sec,1,0)
    'Default Datalogger Battery Voltage measurement BattV
    Battery(BattV)
```

```
    'For TE525MM Rain Gage, use multiplier of 0.1 in PulseCount instruction
    PulseCount(Rain_mm,1,1,2,0,0.1,0)

    'Call Data Tables and Store Data
    CallTable(Tips)
  NextScan

  SlowSequence
  Scan (30,Sec,3,0)
    'Hydraprobe Sensor '0' measurements of Soil Temperature (Temp_C) and Moisture
(SW_wfv)
    SDI12Recorder(HP(),1,"0","M!",1,0)
    'Hydraprobe Sensor '1' measurements of Soil Temperature (Temp_C) and Moisture
(SW_wfv)
    SDI12Recorder(HP_1(),1,"1","M!",1,0)
    'Hydraprobe Sensor '2' measurements of Soil Temperature (Temp_C) and Moisture
(SW_wfv)
    SDI12Recorder(HP_2(),1,"2","M!",1,0)
    'Hydraprobe Sensor '3' measurements of Soil Temperature (Temp_C) and Moisture
(SW_wfv)
    SDI12Recorder(HP_3(),1,"3","M!",1,0)
    'Hydraprobe Sensor '4' measurements of Soil Temperature (Temp_C) and Moisture
(SW_wfv)
    SDI12Recorder(HP_4(),1,"4","M!",1,0)
    'Hydraprobe Sensor '5' measurements of Soil Temperature (Temp_C) and Moisture
(SW_wfv)
    SDI12Recorder(HP_5(),1,"5","M!",1,0)
    'Hydraprobe Sensor '6' measurements of Soil Temperature (Temp_C) and Moisture
(SW_wfv)
    SDI12Recorder(HP_6(),1,"6","M!",1,0)
    'Hydraprobe Sensor '7' measurements of Soil Temperature (Temp_C) and Moisture
(SW_wfv)
    SDI12Recorder(HP_7(),1,"7","M!",1,0)
    'Hydraprobe Sensor '8' measurements of Soil Temperature (Temp_C) and Moisture
(SW_wfv)
    SDI12Recorder(HP_8(),1,"8","M!",1,0)
    'Hydraprobe Sensor '9' measurements of Soil Temperature (Temp_C) and Moisture
(SW_wfv)
    SDI12Recorder(HP_9(),1,"9","M!",1,0)
    'Hydraprobe Sensor 'a' measurements of Soil Temperature (Temp_C) and Moisture
(SW_wfv)
    SDI12Recorder(HP_a(),3,"a","M!",1,0)
    'Hydraprobe Sensor 'b' measurements of Soil Temperature (Temp_C) and Moisture
(SW_wfv)
    SDI12Recorder(HP_b(),3,"b","M!",1,0)
    'Hydraprobe Sensor 'c' measurements of Soil Temperature (Temp_C) and Moisture
(SW_wfv)
    SDI12Recorder(HP_c(),3,"c","M!",1,0)
```

```
    'Hydraprobe Sensor 'd' measurements of Soil Temperature (Temp_C) and Moisture
(SW_wfv)
    SDI12Recorder(HP_d(),3,"d","M!",1,0)
    'Hydraprobe Sensor 'e' measurements of Soil Temperature (Temp_C) and Moisture
(SW_wfv)
    SDI12Recorder(HP_e(),3,"e","M!",1,0)
    'Read Pressure Transducer (CS450) Sensor 'f' every 60 seconds
    SDI12Recorder(CS450,3,"f","M1!",1,0)

    CallTable(PT)
    CallTable(Avgs)
  NextScan

EndProg
```

APPENDIX C

SOIL AND VEGETATION CHARACTERIZATION

C.1. Soil Characterization

Soil characterization within the watershed was performed using field samples to determine bulk density of soils within the watershed. Five samples were taken using soil cores of a volume of ~295 cm^3. These cores were taken at different locations within the watershed and at different depths in order to provide an average soil characterization for the entire watershed. The results of this analysis are presented below.

Sample	Pan weight (g)	Pan+Sample (dry) (g)	Sample (dry) (g)	Bulk Density (g/cm^3)
1	20.5144	423.183	402.6686	1.3650
2	20.8311	395.1348	374.3037	1.2688
3	20.1882	434.2527	414.0645	1.4036
4	20.5535	438.9648	418.4113	1.4183
5	20.1464	437.7038	417.5574	1.4154
Avg				1.3742

Further soil analysis was performed using soil sieving methods in order to determine the relative proportions of clay, silt, and sand within soil samples taken from the region during soil sensor installation. From this analysis the following soil characteristics were discovered:

Location	Depth (cm)	Total Mass (g)	% Sand	% Silt	% Clay
1	10	45.586	27.5	56.3	16.2
1	20	51.317	37.5	38.3	24.2
2	10	38.64	49.6	30.7	19.8
2	20	34.787	34.9	41.9	23.1
Avg			37.4	41.8	20.8

For further characterization of the watershed soil structure, the programs SoilPar and Rosetta were used along with the inputs described above. Using these soil parameter estimate programs the approximate hydraulic conductivity for the soil was found to be 40 mm/hr and the porosity was approximated to be 0.4 m^3/m^3.

C.2. Vegetation Characterization

Finalized watershed vegetation characterization provided earlier in the manuscript was utilizing data collected from UAV flights within the region. Vegetation transects were also performed within the watershed for intra-watershed land cover characterization prior to obtaining UAV flight results. The transects were done on the north-, south-, and west-facing hillslopes of the watershed and covered a 70 m distance. Every 1 m the vegetation was recorded. This transect land cover sampling was performed on 5/25/2010 and 10/22/2010 with the results shown below.

5/25/2010 Vegetation transect results

Common Name	Transect 1	Transect 2	Transect 3	Average
Bare Soil	58.57	62.86	57.14	59.52
Creosote bush	10.71	7.86	7.14	8.57
Mesquite	7.14	0.00	3.57	3.57
Broom Snakeweed	7.14	0.00	0.00	2.38
Rock	2.86	1.43	0.00	1.43
Mariola	0.71	0.71	1.43	0.95
Apache Plume	0.00	0.00	0.71	0.24

10/22/2010 Vegetation Transect results

Common Name	Transect 1	Transect 2	Transect 3	Average
Rock	55.71	47.14	52.86	51.90
Soil	15.71	12.86	10.00	12.86
Litter	4.29	14.29	10.00	9.52
Tarbush	1.43	0.00	0.00	0.48
Snakeweed	1.43	0.00	2.86	1.43
Mesquite	4.29	2.86	1.43	2.86
Prickley-leaf Dogweed	4.29	2.86	2.86	3.33
Mariola	7.14	5.71	5.71	6.19
Bush Muly	1.43	2.86	1.43	1.90
Spike Dropseed	0.00	4.29	0.00	1.43
Creosote	0.00	1.43	0.00	0.48
Feather Plume	0.00	2.86	5.71	2.86
Desert Zinnia	0.00	1.43	0.00	0.48

APPENDIX D

NETWORK MAINTENANCE AND TROUBLESHOOTING GUIDE

This guide presents insights from previous field experience on the maintenance and troubleshooting of equipment installed within the Tromble watershed.

D.1. Monthly Maintenance

The site should be visited monthly in order to assure equipment is clean and in good operating condition. While the telemetry network presents a method for remotely viewing datasets, dust buildup on sensor lenses can skew readings resulting in the need for regular cleaning. Also, data storage space at each datalogger location is limited. If data is not downloaded approximately every four weeks, data loss may occur. At the monthly scale the following activities should be performed:

1) Clean tower sensor lenses including the: net radiometer, pyranometer, sonic anemometer, and IRGA.
2) Download tower data in the following order to insure there is no data loss. A) Use a direct cable connection from a field laptop to the CR5000 and download the ‘Tips’, ‘MET’, and ‘Flux’ 30 min datasets. B) Then remove the CR5000 data card from the data logger and download the ‘.ts’ datasets (.ts = 20Hz Time Series data) directly onto the computer.
3) Insure the datalogger has steady battery voltages for the past several days.
4) If ‘NAN’ or ‘-9999’ values are encountered at the tower first check the cable for the sensor of interest to determine if it has been chewed by rodents. Next, check all cable connections as these may come loose.
5) At the soil moisture transect locations check the ‘Public’ file for each datalogger for every sampling location (Note: On transect 2, sensor ‘2’ will always show values of ‘NAN’ as this sensor was never installed). If ‘NAN’ or ‘-9999’ values are encountered first check the cable for the sensor of interest to determine if it has been chewed by rodents. Next, check the connection of the cable to the connector box within the datalogger enclosure area as these may come loose.
6) Clean all still wells of flumes during each visit as these fill with silt quickly during the rainy season. I have found the easiest method to clean these is the backwash the system by pouring ~5 gallons of water into the top of the still forcing the silt out of the still in the opposite direction of which it usually enters. This also cleans off the pressure transducer and refills the still well so that it is primed for the next storm event.

D.2. Annual Maintenance

1) CO_2 flux readings should be examined at the annual scale in order to determine if they are drifting. If drift occurs recalibration of the IRGA should be considered. As I have not performed a recalibration, I cannot comment on the best method of doing so (i.e. manual calibration in the field or returning the equipment to Campbell for factory calibration).
2) Creation of new pressure transducer calibration curves each year will help to reduce any impact in measurement drift from these sensors as well. A full method of flume calibration equation creation is presented in a later Appendix.
3) All batteries should be checked at the annual scale in order to determine their degradation state. It is important to note that the battery voltage starts dropping below 12V at regular intervals the battery should be replaced to insure the system does not fail due to power issues.

It is important to note that the 2 main issues faced in the past with lost data were due to either power failures within the tower site or cable splicing by rodents or other undesirables. These 2 problems should always be addressed first when attempting to troubleshoot an issue in the field. If battery failure occurs due to several consecutive overcast days resulting in not enough incoming radiation to power the systems, batteries should be recharged and tested for their ability to hold the charge as complete depletion can cause irreparable damage to a battery. Batteries can be charge at the Jornada headquarters.

APPENDIX E

TELEMETRY NETWORK OPERATION

The telemetry network installed at the Jornada watershed was installed for real-time access to sampled data from each of the dataloggers located within the watershed. This access allows for evaluation of currently downloaded datasets and access to all stored data at each of the datalogger locations within the watershed. The telemetry network follows the general setup shown below.

E.1. Telemetry Network Schematic

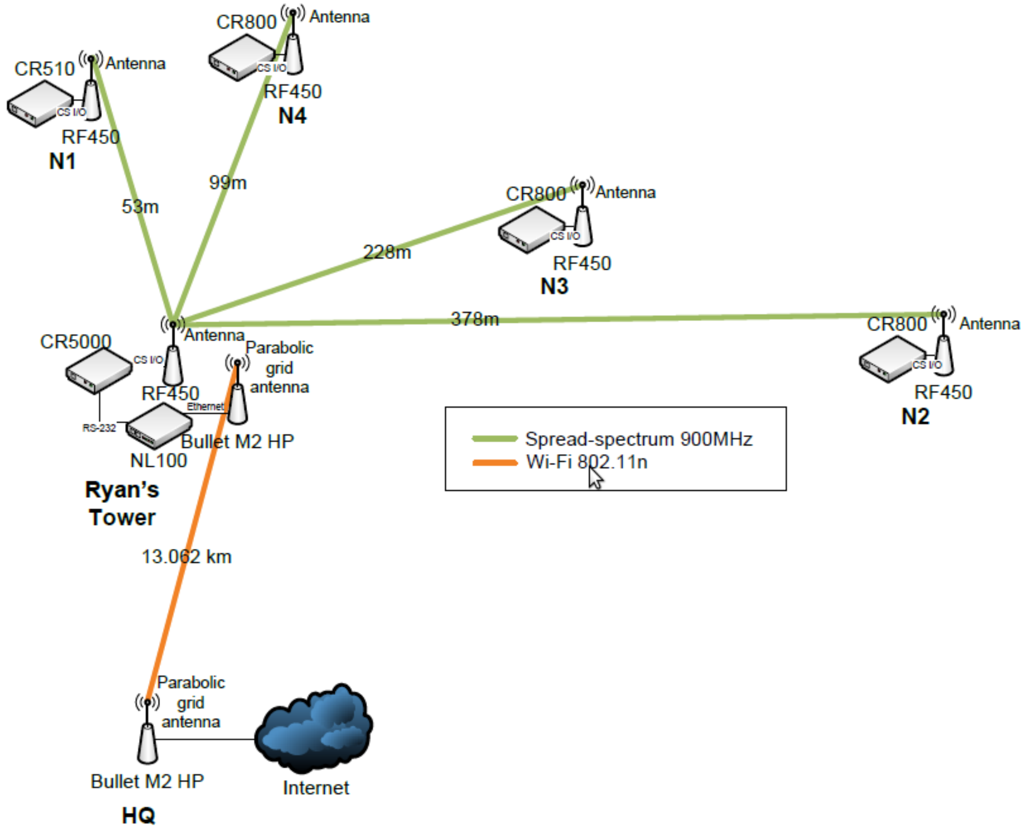

Within the interior of the watershed the telemetry networks broadcasts over a 900 MHz radio signal between the outlet and transect dataloggers to the tower datalogger. The information is then combined over a network adaptor. The network adaptor sends the signal to the Jornada headquarters over a 100Mbps network controlled by 2 Bullet M2HP wireless transceivers. At the headquarters the signal is broadcast through the NMSU network over a secured IP address which can be accessed remotely for data viewing and downloading.

E.2. Remote Connection

Remote connection to the telemetry network from an outside computer can be accomplished using the following step-by-step process. This requires a computer with an internet connetion and the Loggernet software suite.

1. Download the New Mexico State University VPN Client from the following website:

   http://ict.nmsu.edu/VPN/

2. Open the VPN client and import 'Jornada VPN.pcf'
3. Download Loggernet version 4.0 or later.
4. Open Loggernet and enter the 'Setup' screen under the Main menu.
5. Change from EZ View to Standard View ('Std View').
6. Add a Root Directory 'Add Root'. You will be prompted to select the directory type, choose 'IPPort'. You will then be prompted to choose a device. You will need to add 'PakBusPort (Other Loggers)' and add 4 'CR800 Series' dataloggers. Make sure all the devices are located right below the PakBusPort, this is done by highlighting the PakBusPort prior to adding each new datalogger.
7. Next, add another Root Directory 'Add Root' and select another 'IPPort'. The device Type will be CR5000.

You should now have all of the dataloggers listed on your setup screen. Next we will configure the hardware.

8. Highlight 'IPPort' (this is the first IPPort we added). Change the Internet IP Address to '128.123.176.239:6784'. Change the Extra Response Time to '04 s'.
9. Highlight 'PakBusPort' and change the Extra Response Time to '04 s'.
10. Next, configure each of the CR800 Series dataloggers so the PakBus Addresses are 1, 2, 3, or 4. The CR800 with the address 1 is 'HP1' which is located on the soil moisture transect furthest to the west. Address 2 and address 3 are 'HP2' and 'HP3' and are located on the middle and furthest east soil moisture transects respectively. CR800 address 4 is located at the watershed outlet.
11. Next, highlight 'IPPort_2' which should be the second IPPort we set up. The Internet IP Address should be '128.123.176.239:6783', and the Extra Response Time will be '04 s'.
12. Finally, highlight the CR5000 and change the Maximum Time On-Line to 2 hours and the Extra Response Time to '04 s'.
13. Apply changes.

The system should now be setup. You can change the datalogger names in the setup screen if you wish. Finally, you can connect by using the following steps:
1. Open the 'Cisco Systems VPN Client' → 'VPN Client' in Windows.
2. Connect to the Jornada VPN. The Username is 'rtemplet' and the password is 'Jornada2@'.

3. Next Open Loggernet and go to the ‘Connect’ screen under ‘Main’. You should be able to connect to any of the dataloggers by highlighting the datalogger of interest and hitting the ‘Connect’ button.

Telemetry network deficiencies

Currently there is only one known deficiency with the telemetry network. While all data from the transect and watershed outlet dataloggers can be downloaded remotely, the tower data is sampled at such a resolution that the connection speed cannot download as fast as the data is sampled and thus the tower 20 Hz data cannot be downloaded in full sets. This dataset can be monitored in real-time however.

APPENDIX F

FLUME CALIBRATION

F.1. Flume Calibration

Flume calibration equations were produced for each flume within the watershed using the method described below.

First, a small section of the flume neck was isolated so that it could be filled with water to the top of the flume. As this portion of the flume was filled with water, so to did the still well of the flume. Once the flume was filled with water, an initial pressure reading was taken from the datalogger and recorded with the corresponding height of water within the flume as measured from the bottom of the flume neck. Slowly, water was removed from the flume with pressure measurements and height measurements being recorded every 1-2 cm in drop of water height until the flume was completely empty. Using this dataset a linear relationship was created for height vs. pressure readings.

The next step was to create a flow rate vs. water height relationship utilizing the ISO 4359 method which basis water flow rate through a flume on flume dimensions and water height within the flume. Below I outline the steps taken to create this relationship.

The following variables are used for equation calculations:
A = cross-sectional area of approach channel [m2]
b = Bottom width of flume throat [m]
B = Bottom width of approach channel [m]
Cd = Coefficient of discharge for rectangular, trapezoidal, and U flumes [unitless]
Cs = Shape coefficient for trapezoidal flume [unitless]
Cv = Coefficient of approach velocity for rectangular, trapezoidal, and U flumes [unitless]
d = Diameter of throat of U flume [m]
D = Diameter of approach channel of U flume [m]
F = Froude number of flow in approach channel [unitless]. F<1 is slow or sub-critical. F>1 is fast or super-critical.
g = Acceleration due to gravity, 9.8066m/s2.
h = Measured head [m]. If there is a hump, then it is the vertical distance between the top of the hump and the water surface.
H = Total head [m]. Measured head plus velocity head. H=h*Cv^(2/3)
k = Constant used in trapezoidal flume computation [unitless]
L = Length of flume throat [m].
m = Side slope of trapezoidal flume throat. Horizontal to vertical (H:V).
M = Side slope of trapezoidal flume approach channel. Hoirizontal to vertical (H:V).
P = Hump Height [m].
Q = Flowrate through flume [m3/s].
T = Top width of approach channel [m].
V = Velocity in approach channel [m/s].

The following equations were used for calculation of different variables:

$$\boxed{k = \sqrt{1+m^2}}$$

$$\boxed{C_d = \left(1 - \frac{0.006kL}{b}\right)\left(1 - \frac{0.003L}{h}\right)^{3/2}}$$

$$\boxed{A = (P+h)[B + M(P+h)]}$$

$$\boxed{T = B + 2M(P+h)}$$

Take the following steps to calculate the relationship for Q vs. h:

1) Let H = h and obtain C_s from the following graph:

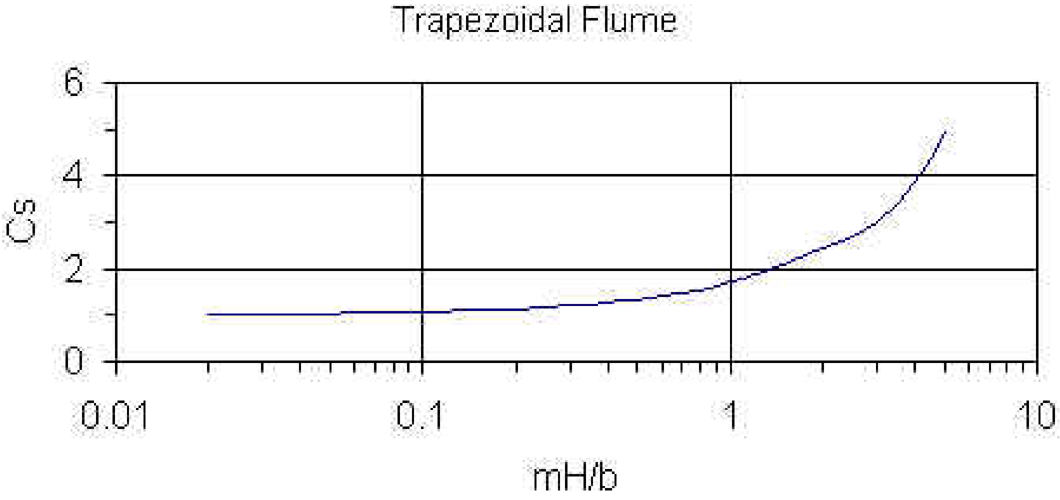

2) Now calculate C_v from:

$$\boxed{\sqrt{C_v^{2/3} - 1} = \frac{2}{3\sqrt{3}} \frac{bhC_vC_s}{A}}$$

3) Finally calculate:

$$\boxed{Q = bC_dC_sC_v\left(\frac{2h}{3}\right)^{\frac{3}{2}}\sqrt{g}}$$

$$\boxed{V = Q/A}$$

Since Cs and Cv are functions of both H and h, recompute H = hCv^(2/3), Cs, Cv, and Q until Q is within 4 significant figures of accuracy and then compute the true V from final Q.

Two relationships have now been created whereby pressure as measured from the PT in field will give you a height of water within the flume. The calculated height can then be used to calculate flow through the flume.

F.2. Outlet Flume Flow Calculation

Calibration of the outlet flume for the watershed was performed in the field prior to this research and equations for flow calculations were provided by Jornada Experimental Range emaployees. These equations are listed below:

$$H = 30.62 * mV - 30.74$$

$$Q = 0.080677862 * H + 4.306711148 * H^2$$

These The first equation which calculates water height in the flume is optimized for a PT which was installed at the outlet prior to this research. If the PT is changed in the future, a new relationship will have t be made using a system similar to that described previously.

F.3. Storm Events Post Processing

Variability in flume PT measurements due to diurnal temperature changes within the still well necessitated post processing of data for individual storm events. To assess this problem, rainfall was analyzed to determine storm onset. Two minutes prior to storm onset (as determined by the earliest tip on the closest rain gauge to each respective flume), runoff data was clipped until 1 hour after rainfall had ended. Data was normalized to produce an initial height reading of zero for the storm event by providing a constant offset to all pressure readings during the storm event. Hydrographs were then calculated using the relationships provided above.

APPENDIX G

SOIL MOISTURE, RAINFALL, AND EDDY COVARIANCE DATA PROCESSING

The information provided in this section is augmented from that given in the main manuscript Methods by increasing description of processing procedure and providing equations for reproduction of the calculated results.

G.1. Soil Moisture Data Processing

Half-hourly averaged soil moisture datasets obtained from Hydraprobe measurements were transformed to volumetric soil moisture (m^3/m^3) values via the ‘loam soil’ type factory calibration equation to coincide with the dominant soil type found in the Tromble watershed (see the soil analysis appendix). For all analyses, periods of interrupted measurements for individual probes resulted in either removal of periods of compromised data from the dataset entirely, or removal of the individual probe data entirely for the period of analysis. In order to calculate spatially averaged soil moisture, the watershed was separated via the main channel network into 3 sections: the north-facing slope, the south-facing slope, and the west-facing slope. Each slope was separated into 5 bins based on elevation. Elevation weighted soil moisture was then calculated for each slope at the three sampled depths with each of the 5 transect soil moisture locations corresponding to one of the 5 elevation bins. Watershed averaged soil moisture was then calculated at each depth by the area-weighted average of slope soil moisture using the equation below:

$$\begin{aligned}\theta_{avg} = (&1448 * SM1 + 1121 * SM2 + 1232 * SM3 + 1348 * SM4 + 15911 * SM5 \\ &+ 2850 * SM6 + 1086 * SM7 + 1312 * SM8 + 1278 * SM9 + 9193 \\ &* SM10 + 997 * SM11 + 535 * SM12 + 624 * SM13 + 865 * SM14 \\ &+ 6891 * SM15)/46691\end{aligned}$$

Finally, profile averaged soil moisture was calculated by treating the measured 5cm soil moisture as average soil moisture over the top 10 cm of soil, measured 15 cm soil moisture was treated as the average soil moisture over the depth of 10-20 cm, and measured 30 cm soil moisture was treated as the average soil moisture over the depth of 20-40 cm.

$$\theta_{profile} = (10 * \theta_{5cm} + 10 * \theta_{15cm} + 20 * \theta_{30cm})/40$$

G.2. Precipitation Data Processing

Upon installation, each Texas Electronic tipping bucket rain gauge was calibrated statically to insure accuracy of individual tip volumes. Watershed-scale spatially averaged precipitation was calculated using the R2, R3, and R4 rain gauges (Appendix A). The watershed outlet and tower rain gauges (R1 and R5 respectively) were omitted from spatially averaged calculations due to a few periods of equipment malfunction over the sampling timeframe. A watershed bound Theissen polygon map (below) was created based on rain gauge location to calculate contributing area-weighted, spatially averaged rainfall using the equation below:

$$P_{avg} = R2 * 0.221283 + R3 * 0.334527 + R4 * 0.44419$$

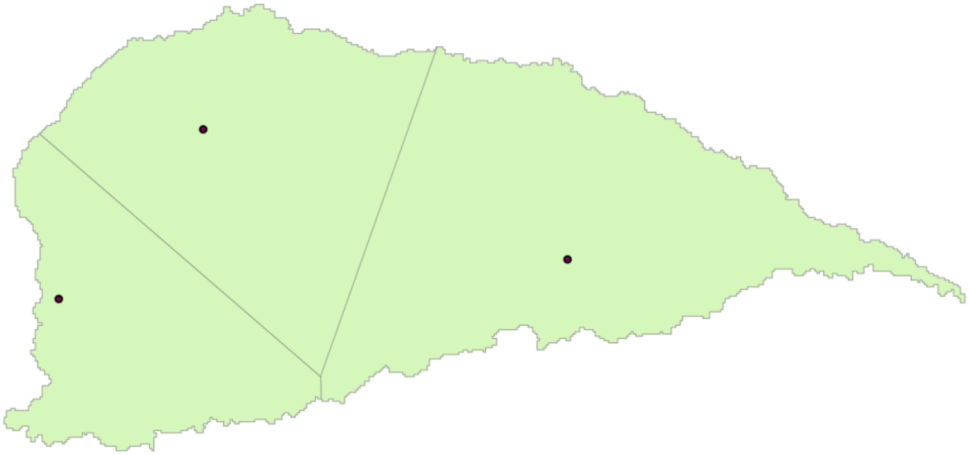

G.3. Eddy Covariance Data Processing

Eddy covariance tower three-dimensional sonic anemometer and open-path gas analyzer data were first filtered to remove rainfall periods and periods of equipment malfunction. Data was then despiked for any samples which were 3+ standard deviations of the mean calculated on a monthly basis. Next, signal lag was removed and subsequent 30 min block averaging was performed. Coordinate plane rotation (Lee et al., 2004), stability, and density fluctuation (Webb et al., 1980) corrections were also performed prior to calculation of finalized fluxes. Sensible heat flux was calculated using the sonic temperature (Schotanus et al. 1983). Fluxes were then examined visually for erroneous data periods. For those 30-min flux periods which were manually removed due to extreme values, linear interpolation of data was performed to gap-fill. Negative latent heat flux values were set equal to zero. Despiking, corrections, and 30 min flux calculations were performed using the EdiRE data software tool (The University of Edinburgh). The process below explains how flux processing was performed in a step-by-step manner, with the EdiRE processing file given at the bottom.

Raw flux time series files for this process are binary Campbell format and include the variables listed below in the order of appearance:

1. Date/Timestamp
2. Ux (velocity in the x-direction)
3. Uy (velocity in the y-direction)
4. Uz (velocity in the z-direction)
5. CO2
6. H2O
7. Temp
8. press
9. diag_csat (CSAT diagnostic)

The raw dataset should first be split into smaller files using Loggernet's "CardConvert" tool. When utilizing this tool make sure to convert all files to an "TOB1" format under the "Destination File Options". Also make sure to check the "Use Time" box under "File Processing". This will allow the user to open the "Time Settings". Input a starting date for processing the raw ts.dat file prior to the date of your first data collection and set the interval to 1 day. I set the processing time to 12am or 12pm, but the time is optional. I also check the “TimeDate Filenames” and “Use Day of Year” tabs under the “File Naming” section in order to make keeping up with the files easier. Make sure you are changing the output to a folder which has no other .dat files and then you can “Start Converserion”. The completion of the conversion should result in multiple “TOB1_2517.ts_data…” files within the designated output folder.

EdiRE will be used for all despiking and flux processing. The processing files performs planar rotation, lag correction, Webb correction, Monin-Obhukov correction, latent and sensible heat flux calculation, and 30 minute averaging. The processing file used for this is “Jornada_Proc6162011”. Prior to using this file one should change the “Wind Direction” within the file to match the navigational orientation in degrees to which their CSAT faces. Prior to running EdiRE, one will need to create a File Format List. This can be done by using the “Interpreter” tool under the “Processing” header. Make sure to check only the “Create raw file format list”. The Raw data file type should be Campbell and the Sample file can be any of the TOB1 files you created earlier. Make sure to specify the Format list name and check the “Load new lists” button. After creating the file format list, load it under the “File” → “Load” headers. Next you should change the output folder to which EdiRE sends your processed files. This is done by clicking the Red Check button and going to the “Output Folders” section. You can now process the data through EdiRE. In order to make it easier you can process approximately 10 files at one time. This can be done by shift clicking multiple files when prompted for the raw file when you start processing.

Jornada_Proc6162011 file:

```
Extract
        From Time =
        To Time =
        Channel = 1
        Label for Signal = SECONDS
Extract
        From Time =
        To Time =
        Channel = 2
        Label for Signal = NANOSECONDS
Extract
        From Time =
        To Time =
        Channel = 3
        Label for Signal = RECORD
Extract
        From Time =
        To Time =
        Channel = 4
        Label for Signal = Ux
Extract
        From Time =
        To Time =
```

```
        Channel = 5
        Label for Signal = Uy
Extract
        From Time =
        To Time =
        Channel = 6
        Label for Signal = Uz
Extract
        From Time =
        To Time =
        Channel = 7
        Label for Signal = co2
Extract
        From Time =
        To Time =
        Channel = 8
        Label for Signal = h2o
Extract
        From Time =
        To Time =
        Channel = 9
        Label for Signal = Ts
Extract
        From Time =
        To Time =
        Channel = 10
        Label for Signal = press
Extract
        From Time =
        To Time =
        Channel = 11
        Label for Signal = diag_csat
Despike
        From Time =
        To Time =
        Signal = co2
        Standard Deviations = 4
        Spike width = 200
        Spike % consistency = 50
        Replace spikes =
        Storage Label spike count = co2spike
        Outlier Standard Deviations = 4
Despike
        From Time =
        To Time =
        Signal = h2o
        Standard Deviations = 4
        Spike width = 200
        Spike % consistency = 50
        Replace spikes =
```

```
        Storage Label spike count = h2ospike
        Outlier Standard Deviations = 4
Remove Lag
        From Time =
        To Time =
        Signal = co2
        Min Lag (sec) = -1
        Lag (sec) = 0.3
        Max Lag (sec) = 1
        Below Min default (sec) =
        Above Max default (sec) =
Remove Lag
        From Time =
        To Time =
        Signal = h2o
        Min Lag (sec) = -1
        Lag (sec) = 0.3
        Max Lag (sec) = 1
        Below Min default (sec) =
        Above Max default (sec) =
Raw Subset
        From Time =
        To Time =
        Subset start time(s) =
        Subset length(s) =
        Signal for condition = diag_csat
        Condition operators = <
        Condition (lower limit) = 4096
        Condition upper limit =
        Storage Label % removed = csat_error
        Number of signals = 6
        Signal Subset = Ux
        Signal Subset = Uy
        Signal Subset = Uz
        Signal Subset = co2
        Signal Subset = h2o
        Signal Subset = Ts
1 chn statistics
        From Time =
        To Time =
        Signal = Ux
        Storage Label Mean = Ux_mean
        Storage Label Std Dev =
        Storage Label Skewness =
        Storage Label Kurtosis =
        Storage Label Maximum =
        Storage Label Minimum =
        Storage Label Variance =
        Storage Label Turbulent Intensity =
        Alt Turbulent Intensity Denominator =
```

```
1 chn statistics
        From Time =
        To Time =
        Signal = Uy
        Storage Label Mean = Uy_mean
        Storage Label Std Dev =
        Storage Label Skewness =
        Storage Label Kurtosis =
        Storage Label Maximum =
        Storage Label Minimum =
        Storage Label Variance =
        Storage Label Turbulent Intensity =
        Alt Turbulent Intensity Denominator =
1 chn statistics
        From Time =
        To Time =
        Signal = Uz
        Storage Label Mean = Uz_mean
        Storage Label Std Dev =
        Storage Label Skewness =
        Storage Label Kurtosis =
        Storage Label Maximum =
        Storage Label Minimum =
        Storage Label Variance =
        Storage Label Turbulent Intensity =
        Alt Turbulent Intensity Denominator =
1 chn statistics
        From Time =
        To Time =
        Signal = co2
        Storage Label Mean = co2_mean
        Storage Label Std Dev =
        Storage Label Skewness =
        Storage Label Kurtosis =
        Storage Label Maximum =
        Storage Label Minimum =
        Storage Label Variance =
        Storage Label Turbulent Intensity =
        Alt Turbulent Intensity Denominator =
1 chn statistics
        From Time =
        To Time =
        Signal = h2o
        Storage Label Mean = H2O_mean
        Storage Label Std Dev =
        Storage Label Skewness =
        Storage Label Kurtosis =
        Storage Label Maximum =
        Storage Label Minimum =
        Storage Label Variance =
```

```
        Storage Label Turbulent Intensity =
        Alt Turbulent Intensity Denominator =
1 chn statistics
        From Time =
        To Time =
        Signal = press
        Storage Label Mean = press_mean
        Storage Label Std Dev =
        Storage Label Skewness =
        Storage Label Kurtosis =
        Storage Label Maximum =
        Storage Label Minimum =
        Storage Label Variance =
        Storage Label Turbulent Intensity =
        Alt Turbulent Intensity Denominator =
1 chn statistics
        From Time =
        To Time =
        Signal = Ts
        Storage Label Mean = Ts_mean
        Storage Label Std Dev =
        Storage Label Skewness =
        Storage Label Kurtosis =
        Storage Label Maximum =
        Storage Label Minimum =
        Storage Label Variance =
        Storage Label Turbulent Intensity =
        Alt Turbulent Intensity Denominator =
Rotation coefficients
        From Time =
        To Time =
        Signal (u) = Ux
        Signal (v) = Uy
        Signal (w) = Uz
        Storage Label Alpha =
        Storage Label Beta  =
        Storage Label Gamma =
        Optional mean u = Ux_mean
        Optional mean v = Uy_mean
        Optional mean w = Uz_mean
Rotation
        From Time =
        To Time =
        Signal (u) = Ux
        Signal (v) = Uy
        Signal (w) = Uz
        Alpha =
        Beta =
        Gamma =
        Do 1st Rot = x
```

```
        Do 2nd Rot = x
        Do 3rd Rot = x
Gas conversion
        From Time =
        To Time =
        Storage Label = e
        Apply to =
        Apply by =
        Measured variable = H2O_mean
        Convert from = Absolute density g/m3
        Convert to = Partial Pressure kPa
        Temperature (C) = Ts_mean
        Pressure (kPa) = press_mean
        Water vapour = H2O_mean
        Water vapour units = Partial pressure kPa
        Molecular weight (g/mole) = 18
Sensible heat flux coefficient
        From Time =
        To Time =
        Storage Label = rhoCp
        Apply to =
        Apply by =
        Vapour pressure (KPa) = e
        Min or QC =
        Max or QC =
        Temperature (C) = Ts_mean
        Min or QC =
        Max or QC =
        Pressure (KPa) = press_mean
        Min or QC =
        Max or QC =
        Alternate rhoCp = 1296.0243
Latent heat of evaporation
        From Time =
        To Time =
        Storage Label = L
        Apply to =
        Apply by =
        Temperature (C) = Ts_mean
        Min or QC =
        Max or QC =
        Pressure (KPa) = press_mean
        Min or QC =
        Max or QC =
        LE flux coef, L = 2440
Friction Velocity
        From Time =
        To Time =
        Signal (u) = Ux
        Signal (v) = Uy
```

```
        Signal (w) = Uz
        Storage Label U* (uw) =
        Storage Label U* (uw vw) =   ustar
2 chn statistics
        From Time =
        To Time =
        Signal = h2o
        Signal = Uz
        Storage Label Covariance = h2o_cov
        Storage Label Correlation =
        Storage Label Flux = LE
        Flux coefficient = L
2 chn statistics
        From Time =
        To Time =
        Signal = Ts
        Signal = Uz
        Storage Label Covariance = Ts_cov
        Storage Label Correlation =
        Storage Label Flux = H
        Flux coefficient = rhoCp
2 chn statistics
        From Time =
        To Time =
        Signal = co2
        Signal = Uz
        Storage Label Covariance = co2_cov
        Storage Label Correlation =
        Storage Label Flux = FC
        Flux coefficient = 1
User defined
        From Time =
        To Time =
        Storage Label = Wind_sp
        Apply to =
        Apply by =
        Equation = SQRT(Ux_mean^2+Uy_mean^2)
        Variable = Ux_mean
        Variable = Uy_mean
Wind direction
        From Time =
        To Time =
        Signal (u) = Ux
        Signal (v) = Uy
        Orientation = 216
        Wind Direction Components = U+N_V+E
        Wind Direction Output = N_0_deg-E_90_deg
        Storage Label Wind Direction = Wind_dir
        Storage Label Wind Dir Std Dev =
Stability - Monin Obhukov
```

```
        From Time =
        To Time =
        Storage Label = Stability
        Apply to =
        Apply by =
        Measurement height (m) = 7
        Zero plane displacement (m) = 2.0
        Virtual Temperature (C) = Ts_mean
        Min or QC =
        Max or QC =
        H flux (W/m2) = H
        Min or QC =
        Max or QC =
        H flux coef, RhoCp = rhoCp
        Min or QC =
        Max or QC =
        Scaling velocity (m/s) = ustar
        Min or QC =
        Max or QC =
Frequency response
        From Time =
        To Time =
        Storage Label = H_frqres
        Apply to =
        Apply by =
        Correction type = WX
        Measurement height (m) = 7
        Zero plane displacement (m) = 2.0
        Boundary layer height (m) = 1000
        Stability Z/L = Stability
        Wind speed (m/s) = Wind_sp
        Sensor 1 Flow velocity (m/s) = Wind_sp
        Sensor 1 Sampling frequency (Hz) = 20.0
        Sensor 1 Low pass filter type =
        Sensor 1 Low pass filter time constant =
        Sensor 1 High pass filter type =
        Sensor 1 High pass filter time constant =
        Sensor 1 Path length (m) = 0.15
        Sensor 1 Time constant (s) = 0
        Sensor 1 Tube attenuation coef =
        Sensor 2 Flow velocity (m/s) = Wind_sp
        Sensor 2 Sampling frequency (Hz) = 20.0
        Sensor 2 Low pass filter type =
        Sensor 2 Low pass filter time constant =
        Sensor 2 High pass filter type =
        Sensor 2 High pass filter time constant =
        Sensor 2 Path length (m) = 0.15
        Sensor 2 Time constant (s) = 0
        Sensor 2 Tube attenuation coef =
        Path separation (m) =
```

Get spectral data type = Model
Get response function from = model
Reference Tag =
Reference response condition =
Sensor 1 subsampled =
Sensor 2 subsampled =
Apply velocity distribution adjustment =
Use calculated distribution =
Velocity distribution std dev=
Stability distribution std dev=

Frequency response

From Time =
To Time =
Storage Label = CLE_frqres
Apply to =
Apply by =
Correction type = WX
Measurement height (m) = 7
Zero plane displacement (m) = 2.0
Boundary layer height (m) = 1000
Stability Z/L = Stability
Wind speed (m/s) = Wind_sp
Sensor 1 Flow velocity (m/s) = Wind_sp
Sensor 1 Sampling frequency (Hz) = 20.0
Sensor 1 Low pass filter type =
Sensor 1 Low pass filter time constant =
Sensor 1 High pass filter type =
Sensor 1 High pass filter time constant =
Sensor 1 Path length (m) = 0.15
Sensor 1 Time constant (s) = 0
Sensor 1 Tube attenuation coef =
Sensor 2 Flow velocity (m/s) = Wind_sp
Sensor 2 Sampling frequency (Hz) = 20.0
Sensor 2 Low pass filter type =
Sensor 2 Low pass filter time constant =
Sensor 2 High pass filter type =
Sensor 2 High pass filter time constant =
Sensor 2 Path length (m) = 0.125
Sensor 2 Time constant (s) = 0.0
Sensor 2 Tube attenuation coef =
Path separation (m) = 0.05
Get spectral data type = Model
Get response function from = model
Reference Tag =
Reference response condition =
Sensor 1 subsampled =
Sensor 2 subsampled =
Apply velocity distribution adjustment =
Use calculated distribution =
Velocity distribution std dev=

```
          Stability distribution std dev=
Mathematical operation
          From Time =
          To Time =
          Storage Label = Hc
          Apply to =
          Apply by =
          Measured variable A = H
          Operation  = *
          Measured variable B = H_frqres
Mathematical operation
          From Time =
          To Time =
          Storage Label = LEc
          Apply to =
          Apply by =
          Measured variable A = LE
          Operation  = *
          Measured variable B = CLE_frqres
Mathematical operation
          From Time =
          To Time =
          Storage Label = FCc
          Apply to =
          Apply by =
          Measured variable A = FC
          Operation  = *
          Measured variable B = CLE_frqres
Webb correction
          From Time =
          To Time =
          Storage Label = WPL_LE
          Apply to =
          Apply by =
          Scalar value type = Partial Pressure (kPa)
          Scalar value = e
          Min or QC =
          Max or QC =
          Water vapour value type = Partial Pressure (kPa)
          Water vapour value = e
          Min or QC =
          Max or QC =
          Temperature (C) = Ts_mean
          Min or QC =
          Max or QC =
          Pressure (KPa) = press_mean
          Min or QC =
          Max or QC =
          H flux (W/m2) = Hc
          Min or QC =
```

```
        Max or QC =
        LE flux (W/m2) = LEc
        Min or QC =
        Max or QC =
        H flux coef, RhoCp = rhoCp
        Min or QC =
        Max or QC =
        LE flux coef, L = L
        Min or QC =
        Max or QC =
        Scalar molecular wt. = 18
        Scalar flux type = LE (W/m2)
        Scalar flux coefficient = L
        Min or QC =
        Max or QC =
        Alternate water vapour pressure (kPa) =
        Alternate temperature (C) =
        Alternate pressure (kPa) =
Mathematical operation
        From Time =
        To Time =
        Storage Label = LEcw
        Apply to =
        Apply by =
        Measured variable A = LEc
        Operation  = +
        Measured variable B = WPL_LE
Webb correction
        From Time =
        To Time =
        Storage Label = WPL_FC
        Apply to =
        Apply by =
        Scalar value type = Density (mg/m3)
        Scalar value = co2_mean
        Min or QC =
        Max or QC =
        Water vapour value type = Partial Pressure (kPa)
        Water vapour value = e
        Min or QC =
        Max or QC =
        Temperature (C) = Ts_mean
        Min or QC =
        Max or QC =
        Pressure (KPa) = press_mean
        Min or QC =
        Max or QC =
        H flux (W/m2) = Hc
        Min or QC =
        Max or QC =
```

```
	LE flux (W/m2) = LEcw
	Min or QC =
	Max or QC =
	H flux coef, RhoCp = rhoCp
	Min or QC =
	Max or QC =
	LE flux coef, L = L
	Min or QC =
	Max or QC =
	Scalar molecular wt. = 44
	Scalar flux type = Fx (mg/m2/s)
	Scalar flux coefficient = 1
	Min or QC =
	Max or QC =
	Alternate water vapour pressure (kPa) =
	Alternate temperature (C) =
	Alternate pressure (kPa) =
Mathematical operation
	From Time =
	To Time =
	Storage Label = FCcw
	Apply to =
	Apply by =
	Measured variable A = FCc
	Operation  = +
	Measured variable B = WPL_FC
Plot Value
	From Time =
	To Time =
	Left Axis Value = Hc
	Right Axis Value = H
	Left Axis Minimum =
	Left Axis Maximum =
	Right Axis Minimum =
	Right Axis Maximum =
	Match Left/Right Axes =
Plot Value
	From Time =
	To Time =
	Left Axis Value = LEcw
	Right Axis Value = LEc
	Left Axis Minimum =
	Left Axis Maximum =
	Right Axis Minimum =
	Right Axis Maximum =
	Match Left/Right Axes =
Plot Value
	From Time =
	To Time =
	Left Axis Value = LEc
```

```
        Right Axis Value = LE
        Left Axis Minimum =
        Left Axis Maximum =
        Right Axis Minimum =
        Right Axis Maximum =
        Match Left/Right Axes =
Plot Value
        From Time =
        To Time =
        Left Axis Value = LEcw
        Right Axis Value = Hc
        Left Axis Minimum =
        Left Axis Maximum =
        Right Axis Minimum =
        Right Axis Maximum =
        Match Left/Right Axes =
Plot Value
        From Time =
        To Time =
        Left Axis Value = FCcw
        Right Axis Value = FCc
        Left Axis Minimum =
        Left Axis Maximum =
        Right Axis Minimum =
        Right Axis Maximum =
        Match Left/Right Axes =
```

APPENDIX H

POINT SCALE MODELING PARAMETERS

H.1. Point-scale Modeling Parameters

Lists of the utilized tRIBS parameters for point-scale modeling of hydrologic surface/atmosphere interactions are given below. They are split into 2 separate tables depending on whether they are parameters located in the soil parameter input file or the land use parameter input file. Other important parameters necessary for the accurate modeling of these periods of the Jornada basin, but not listed in these two input files are: 1) Depth to Bedrock = 0.9 m, 2) Depth of Water Table = 900 mm, 3) Baseflow Discharge = 0.01 m^3/s, 4) Channel Roughness = 0.15.

Soil Parameters				
Parameter	Description	Units	2010 run	2011 run
Ks	Saturated Hydraulic Conductivity	[mm/hr]	80	80
thetaS	Soil Moisture at Saturation	[ ]	0.4	0.4
thetaR	Residual Soil Moisture	[ ]	0.035	0.02
m	Pore distribution index	[ ]	0.85	0.85
PsiB	Air Entry Bubbling Pressure	[mm] (negative)	0	0
f	Decay parameter	[mm^{-1}]	0.1	0.1
As	Saturated Anisotropy Ratio	[ ]	1	1
Au	Unsaturated Anisotropy Ratio	[ ]	1	1
n	Porosity	[ ]	0.45	0.45
ks	Volumetric Heat Conductivity	[J/msK]	0.05	0.05
Cs	Soil Heat Capacity	[J/msK]	300000	300000

Land Use or Vegetation Parameters				
Parameter	Description	Units	2010 run	2011 run
a	Canopy Storage	[mm]	0.04	0.04
b1	Interception Coefficient	[ ]	0.04	0.04
P	Free Throughfall Coefficient	[ ]	0.96	0.96
S	Canopy Field Capacity	[mm]	0.1	0.1
K	Drainage Coefficient	[mm/hr]	0.15	0.15
b2	Drainage Exponential Parameter	[mm^{-1}]	3.7	3.7
Al	Albedo	[ ]	0.15	0.2
h	Vegetation height	[m]	0.1	0.1
Kt	Optical Transmission Coefficient	[ ]	0.9	0.65
Rs	Canopy-average Stomatal Resistance	[s/m]	111.8	111.8
V	Vegetation fraction	[ ]	0.42	0.42
LAI	Canopy Leaf Area Index	[ ]	0.5	0.5

APPENDIX I

HARGREAVES EVAPOTRANPIRATION ESTIMATES

I.1. Hargreaves Estimates

The following dataset represents the evapotranspiration estimates (ET$_0$) using the Hargreaves equation.

Date	ET$_0$ [mm/day]	Date	ET$_0$ [mm/day]	Date	ET$_0$ [mm/day]
6/6/2010	0.623	7/20/2010	0.614	12/30/2010	0.012
6/7/2010	0.538	7/21/2010	0.549	12/31/2010	0.000
6/8/2010	0.636	7/22/2010	0.481	1/1/2011	0.000
6/9/2010	0.655	7/23/2010	0.494	1/2/2011	0.000
6/10/2010	0.535	7/24/2010	1.082	1/3/2011	0.013
6/11/2010	0.498	7/25/2010	0.932	2/2/2011	0.000
6/12/2010	0.565	7/26/2010	1.494	2/3/2011	0.000
6/13/2010	0.494	7/27/2010	2.113	2/4/2011	0.000
6/14/2010	0.516	7/28/2010	1.312	2/5/2011	0.075
6/15/2010	0.567	7/29/2010	0.908	2/6/2011	0.079
6/16/2010	0.594	7/30/2010	2.214	2/7/2011	0.085
6/17/2010	0.578	7/31/2010	0.920	2/8/2011	0.159
6/18/2010	0.622	8/1/2010	1.252	2/9/2011	0.036
6/19/2010	0.656	8/2/2010	2.260	2/10/2011	0.055
6/20/2010	0.657	8/11/2010	0.684	2/11/2011	0.109
6/21/2010	0.631	8/12/2010	0.616	2/12/2011	0.139
6/22/2010	0.548	8/13/2010	0.715	2/13/2011	0.195
6/23/2010	0.579	8/14/2010	0.688	2/14/2011	0.185
6/24/2010	0.654	8/15/2010	0.616	2/15/2011	0.225
6/25/2010	0.594	8/16/2010	0.456	2/16/2011	0.229
6/26/2010	0.480	8/17/2011	0.973	2/17/2011	0.163
6/27/2010	0.613	8/23/2010	0.534	2/18/2011	0.181
6/28/2010	0.570	12/9/2010	0.060	2/19/2011	0.201
6/29/2010	2.361	12/10/2010	0.098	2/20/2011	0.166
6/30/2010	0.399	12/11/2010	0.091	2/21/2011	0.135
7/1/2010	0.457	12/12/2010	0.059	2/22/2011	0.169
7/2/2010	0.361	12/13/2010	0.074	2/23/2011	0.169
7/3/2010	0.543	12/14/2010	0.093	2/24/2011	0.117
7/4/2010	0.606	12/15/2010	0.062	2/25/2011	0.157
7/5/2010	0.564	12/16/2010	0.047	2/26/2011	0.175
7/6/2010	0.488	12/17/2010	0.038	2/27/2011	0.102
7/7/2010	0.529	12/18/2010	0.043	2/28/2011	0.142
7/8/2010	2.228	12/19/2010	0.073	3/1/2011	0.285
7/9/2010	2.061	12/20/2010	0.054	3/2/2011	0.359
7/10/2010	0.415	12/21/2010	0.077	3/3/2011	0.340

Date	ET_0 [mm/day]	Date	ET_0 [mm/day]	Date	ET_0 [mm/day]
7/11/2010	0.505	12/22/2010	0.045	3/4/2011	0.305
7/12/2010	3.047	12/23/2010	0.047	3/5/2011	0.241
7/13/2010	3.905	12/24/2010	0.046	3/6/2011	0.269
7/14/2010	3.842	12/25/2010	0.039	3/7/2011	0.285
7/15/2010	0.516	12/26/2010	0.043	3/8/2011	0.236
7/16/2010	0.511	12/27/2010	0.029	3/9/2011	0.312
7/17/2010	0.568	12/28/2010	0.043	3/10/2011	0.352
7/18/2010	0.595	12/29/2010	0.016	3/11/2011	0.335
7/19/2010	0.546				